UNIVERSITÀ DEGLI STUDI DI PADOVA

DIPARTIMENTO DI ASTRONOMIA

Dottorato di Ricerca in Astronomia
Ciclo XIX

FORMATION AND EVOLUTION OF EARLY-TYPE GALAXIES: Spectro-Photometry from Cosmo-Chemo-Dynamical Simulations

Coordinatore: Prof. Giampaolo Piotto
Supervisori: Prof. Cesare Chiosi
Dott. Rosaria Tantalo

Dottorando: SIMONETTA CHINELLATO

DATA CONSEGNA TESI
31 Gennaio 2008

UNIVERSITY OF PADOVA

ASTRONOMY DEPARTMENT

PhD in Astronomy
Course XIX

FORMATION AND EVOLUTION OF EARLY-TYPE GALAXIES: Spectro-Photometry from Cosmo-Chemo-Dynamical Simulations

PhD Coordinator: Prof. Giampaolo Piotto
Supervisors: Prof. Cesare Chiosi
Dott. Rosaria Tantalo

Candidate: SIMONETTA CHINELLATO

January 31st, 2008

Riassunto

Una delle principali questioni ancora aperte nell'ambito dell'astrofisica moderna consiste nel comprendere l'origine e l'evoluzione delle galassie, in particolare delle galassie 'early-type' (ETGs) più luminose, all'interno di un contesto cosmologico che presuppone un universo dominato da materia oscura fredda, e da una energia oscura sotto forma della costante cosmologica Λ.

Questi sistemi sferoidali sono di grande interesse in quanto comprendono la maggior parte della massa stellare dell'universo locale (Fukugita et al. 1998). Le galassie ellittiche giganti costituiscono i sistemi stellari più massicci e sembrano definire un'omogenea classe di oggetti vecchi e di metallicità sopra solare (Bressan et al. 1993), hanno una scarsa quantità di gas e una formazione stellare attuale nulla, questo significa che si siano dovute formare ad alti redshift. Forti evidenze osservative mostrano galassie ellittiche già formate a redshift $z \sim$ 2-3 e che in queste galassie la maggior parte delle stelle si siano formate a redshift precedenti a $z = 1$ (Searle et al. 1973; Brinchmann & Ellis 2000; Treu et al. 2005; van der Wel et al. 2005). Questa classe di galassie dunque costituisce un buona testimonianza della evoluzione, della formazione delle stelle e dell'arricchimento chimico nell'universo primordiale.

Scopo principale di questa tesi di Dottorato è lo sviluppo di un strumento in grado di combinare i risultati ottenuti dalle simulazioni numeriche, che seguono l'evoluzione cosmologica, chimica e dinamica di galassie ellittiche, con i modelli di evoluzione spettro-fotometrica attraverso la tecnica di sintesi di popolazione evolutiva. L'obiettivo consiste nel riprodurre le proprietà integrate delle galassie 'early-type' osservate in qualsiasi sistema fotometrico, ed in particolare nei sistemi fotometrici utilizzati dalle più comuni e moderne survey nel campo della cosmologia osservativa.

La tecnica della sintesi di popolazione evolutiva prevede la costruzione di 'oggetti', quali le SSP, le cui caratterisctiche sono tali da permettere lo studio di sistemi più complessi, come le galassie ellittiche, eventualmente generate da simulazioni numeriche semplicemente come composizione di diverse popolazioni stellari. Una volta ottenuto lo spettro della galassia in esame è possibile studiarne tutte le proprietà integrate, come ad esempio luminosità, magnitudini, colori, etc. Il confronto di queste con le proprietà osservate permette di testare i vari parametri dei

modelli, come massa, tasso di formazione stellare, funzione di massa iniziale, processi fisici, etc.

Nella presente ricerca, l'approccio sintetico consente la determinazione di quantità spettroscopiche e fotometriche ottenute combinando tra loro il metodo di sintesi evolutiva di popolazione con le simulazioni tridimensionali di evoluzione cosmologica, chimica e dinamica, delle galassie ellittiche ottenute dal gruppo di Padova (Merlin & Chiosi 2006; Merlin & Chiosi 2007) la cui evoluzione è seguita dalla loro formazione fino all'epoca presente.

Il codice è stato testato su tre galassie simulate: tali modelli evolvono in scenari cosmologici diversi, uno presenta una cosmologia di tipo standard (*SCDM*), gli altri due invece considerano un universo basato sulla costante cosmologica ΛCDM.

Nella prima parte della tesi consideriamo i modelli di galassie, simulati per via dinamica e con una dettagliata evoluzione chimica, e ricaviamo la loro evoluzione spettro-fotometrica nel sistema di riferimento comovente e dalla quale otteniamo le proprietà integrate, quali magnitudini e colori, per le diverse epoche. In tal modo è possibile seguire l'evoluzione spettro-fotometrica di queste galassie tracciata attraverso tutta l'età dell'universo fino ai giorni nostri. In particolar modo vengono riportati i risultati trovati in due importanti sistemi fotometrici: Bessell-Brett e della Sloan Digital Sky Survey.

Lo sviluppo di dei moderni telescopi ha portato a nuove scoperte nella cosmologia osservativa consentendo lo studio delll'evoluzione galattica a partire da epoche primordiali. In questo contesto, le survey fotometriche che coprono ampi intervalli spettrali, dall'ultravioletto (UV) al vicino infrarosso (near-IR), hanno consentito osservazioni di galassie sempre più distanti e deboli con una efficienza sempre maggiore, questo permette uno studio più approfondito dell'evoluzione galattica su un intervallo più ampio di redshift.

Partendo dai risultati ottenuti attraverso la sintesi evolutiva, sono state ricavate le correzioni evolutive e cosmologiche, da apportare a magnitudi e colori per la determinazione dell'evoluzione ad alti redshift delle proprietà delle galassie simulate. Sono stati considerati i cataloghi di galassie di due recenti survey ad alto redshift quali COSMOS e GOODS da cui è possibile fare una selezione morfologica delle galassie, isolando quelle ellittiche, per un confronto qualitativo e quantitativo con i risultati teorici da noi ottenuti.

I tre modelli presi in considerazione sono stati confrontati con le galassie del database di COSMOS e il risultato ottenuto mostra che l'andamento generale dei modelli segue quello dei dati osservativi, in particolare esiste un buon accordo con le galassie classificate come ellittiche. Il confronto dei modelli con le galassie del database di GOODS mostra un migliore accordo con i dati osservativi rispetto ai dati di COSMOS. Poiché il databse di GOODS consente una migliore classificazione morfologica, in quanto viene fatta per via visiva rispetto a quella automatizzata

di COSMOS, questo risulta piu affidabile.

In entrambi i casi verifichiamo che i colori simulati nei diversi scenari cosmologici seguono l'andamento medio a redshift più bassi e sono in accordo con i dati osservativi fino a redshift $z \sim 1$, al di sopra del quale il numero di galassie ellittiche osservate diminuisce rapidamente. Possiamo concludere che fino a $z \sim 1$ i colori simulati riproducono in modo molto siddisfacente i dati osservati.

La combinazione dei i parametri dinamici derivati dalle simulazioni numeriche e delle proprietà spettro-fotometriche ricavate dal nostro strumento permettono di studiare con maggiore dettaglio le leggi di scala che legano i parametri strutturali e fotometrici delle galassie ellittihce, ed in particolare la relazione di Kormendy che lega luninosità e raggio.

Il metodo introdotto per ricavare i parametri morfologici e strutturali utili al confronto con le leggi di scala osservate, si basa sulla costruzione di immagini artificiali in un piano bidimensionale, a partire dai modelli tridimensional simulati. Combinando i modelli di sintesi di popolazione con le geometria tridimensionale della struttura della galassia, e con i dettagli riguardanti l'evoluzione chimica, abbiamo creato immagini sintetiche delle galassie in un determinato sistema fotometrico. Dalle immagini sintetiche così ottenute ricaviamo i parametri strutturali e morfologici, quali il raggio effettivo, la luminosità all'interno di questo, gli indici di struttura tramite l'analisi di Fourier e di Sérsic, assieme ai profili radiali dei più importanti parametri che definiscono la struttura delle galassie.

Questi parametri sono stati confrontati con quelli osservati. In particolare è stata analizzatata la relazione di Kormendy, in quanto è l'unica che al momento siamo in grado di costruire per via della limitata risoluzione delle simulazioni numeriche. Luminosità e raggio effettivo sono stati ricavati dai nostri modelli e sono stati confrontati con la relazione di Kormendy ottenuta dalla survey della SDSS selezionandone solo le galassie ellittiche. Il confronto con i dati è risultato, nonostante la disomogeneita' dei modelli, accettabile.

Abstract

One of the major challenges in modern astrophysiscs is to understand the origin and the evolution of galaxies, the bright Early-Type Galaxies (ETGs) in particular, in the context of a Universe dominated by Cold Dark Matter (CDM), with some kind of Dark Energy in form of the Cosmological Constant Λ (Chiosi 2000).

These spheroidal systems are of interest in their own right as they contain more than half of the total stellar mass in the local Universe (Fukugita et al. 1998). Giant elliptical galaxies are the most massive stellar systems and they appear to define a homogeneous class of objects which predominantly consist of uniformly old and red populations, which implies that they must have formed at high redshift, have negligible amounts of gas and very little star formation (Bressan et al. 1993). There is strong observational evidence that ellipticals are already in place at $z \sim 2-3$ and that formed most of their stars well before a redshift $z = 1$ (Searle et al. 1973; Brinchmann & Ellis 2000; Treu et al. 2005; van der Wel et al. 2005). These galaxies are therefore likely to be good probes of galaxy evolution, star formation and metal enrichment in the early Universe.

The main goal of this PhD thesis is the derivation of a tool that combines the results derived from the cosmo-chemo-dynamical models of elliptical galaxies obtained from N-body simulations, together with the spectro-photometric models computed from the stellar Evolutionary Population Synthesis (EPS) technique. The aim is to reproduce the observational integrated properties of early-type galaxies in any photometric bandpass, and in particular in the systems used by the modern imaging surveys of observational cosmology, that cover any spectral range.

The EPS technique is based on Simple Stellar Populations (SSPs) due to their characteristics, these are suitable for purposes of population synthesis of more complex systems of stellar populations, such as simulated ETGs derived from numerical simulations, and so are suitable for the modelling of the integrated properties (light), and allow easy testing for different input prescriptions in the description of a galaxy (different masses, star formation, initial mass functions, physical processes, etc.) and reproduction of basic observational constraints.

In the present work, the approach allows the computation of spectroscopic and photometric

quantities by combining the EPS technique to three-dimensional self-consistent cosmo-chemo-dynamical Tree-SPH numerical simulations, carried on in the last years by the Padova group (Merlin & Chiosi 2006, 2007), that follow the evolution of ETGs from the epoch of their complex formation to the present. The method has been tested so far on three simulated galaxies: these models have different cosmological metrics, both cold dark matter (CDM) scenarios, one in the *SCDM* and two in the Λ*CDM* cosmologies.

In the first part of the thesis we consider the template galaxies, which have been dynamically simulated with a detailed chemical evolution, and recover their spectro-photometric evolution in the rest-frame and the integrated properties, such as magnitudes and colors, at the different epochs through the entire history of the Universe up to the formation of present-day ellipticals. This is done in particluar for two inportant photometric systems, the Bessell-Brett passbands and the Sloan Digital Sky Survey (SDSS).

The advent of the modern giant telescope facilities has opened a new era in observational cosmology and galaxy evolution can be traced back to its early stages. In this sense, deep multicolor imaging surveys are established as a powerful tool to access the population of faint galaxies with relatively high efficiency. These surveys sample the whole spectral range from the UV to the near-IR bands, enabling galaxy evolution to be followed on a wider range of redshifts.

Starting from the evolutionary synthesis results we compute the evolutionary and cosmological corrections, along with magnitudes and colors and their evolution at different redshifts for the simulated galaxies at our disposal. We consider the COSMOS (Giavalisco et al. 2004) and the GOODS (Scoville et al. 2007) databases, which allow us to select a sample of galaxies that are catalogued as early-type and to make a qualitative and quantitative comparison between the theoretical results obtained from our model galaxies and the observational data. For the COSMOS database we find that the models follow the general trend for all data at high redshift and, in particular, are in good agreement with those galaxies selected as ellipticals. For the galaxies selected from the GOODS database, theoretical colors seem to match better with data than what found for the COSMOS data. Having a better morphological classificator, the selection is done by eye and by correlating a catalog of photometric and spectroscopic redshifts with a morphological one for GOODS in contrast to the selection derived from the automated pipelines used for COSMOS, is certainly discriminating in favour of the GOODS database.

For both datasets our findings show that simulated colors for the different cosmological scenarios follow the general trend at lower redshifts and are in good agreement with the data up to $z \sim 1$, where the number of early-type galaxies observed falls abruptly. In conclusion, within the redshift range considered, all the simulated colors reproduce quite well the observational data.

The dynamical and geometrical informations, derived from the numerical simulations, and the spectro-photometric properties, recovered from our tool, combined together, allow to tackle in some detail important physical issues that deal with the scaling relations governing the photometric and structural parameters of ETGs, and in particluar with the Kormendy relation that allows a comparison with observables in the luminosity-radius plane.

The method we introduced for the derivation of the parameters that enter the scaling laws deals with the construction of artificial images in a bi-dimensional plane, starting from the three-dimensional structure of the simulated galaxies. By matching the population synthesis models with the three-dimensional geometric information of the galaxy's structure along with the chemical details, both provided by the N-body simulations, we create synthetic images of a galaxy in a given photometric system, from which we derive the structural and morphological parameters, such as the galaxy's effective radius and the luminosity within this, the shape indices through Fourier and Sérsic analysis, color profiles, and radial profiles of most of the parameters that define the structure of galaxies.

The most interesting aspect of these results is that the investigation of the simulated galaxies, via the photometric analysis of the artificial images, led us to recover properties that resemble those of observed galaxies. The results obtained in this way are studied and compared within the scaling laws, the Kormendy relation in particular, as it is the only one we can construct so far, due to the limited resolution of our simulations. The observational data with which we compare our simulated results have been selected form the SDSS database. We separate a subsample of elliptical galaxies, and our findings show that the values of luminosities and effective radii, the two parameters that compare in the Kormendy relation, measured for our model galaxies are consistent with the archivial data from the SDSS.

The application of this tool to the simulated galaxies at our disposal allows to understand that the method, still at its infancy, provides good results that permit a comparison between the numerical models and the observational data.

Even if a small sample of simulated galaxies does not allow for a statistical generalization and we have to attend a more complete library of simulated galaxies that, e.g., evolve in the same cosmological scenario, cover a wider range in mass, etc., the main result of this thesis consists in the fact that the method developed to follow the spectro-photometric evolution of galaxies stands up.

As a natural consequence of this work, is that the code has to be reassessed in more detail (e.g., expanded to any photometric system, added dust, ..) and hence tested on a wider library of simulations with different parameters, in order to derive the spectro-photometric parameters

from the EPS technique and the morphological and structural parameters from the analysis of the artificial images, and their evolution in a cosmological context. The determination of the cosmological evolution of these properties will allow for a study of the scaling laws as a function of look-back time that provides a probe for the possibile evolution of these empirical relations.

Contents

List of Figures

List of Tables

Introduction

The numerical simulations combined with stellar population synthesis codes which enable us to predict not only structural and kinematical properties but also photometric and spectroscopic ones are indispensable in solving important problems related to the formation and evolution of galaxies.

The synthetic approach and its application to template galaxies allows the computation of photometric quantities starting from the derivation of Spectral Energy Distributions (SEDs), magnitudes and colors of Simple Stellar Populations (SSPs). SSPs, due to their characteristics, are suitable for purposes of Evolutionary Population Synthesis (EPS) of more complex systems of stellar populations, the Early-Type Galaxies (ETGs) in our case, derived from numerical chemo-cosmo-dynamical simulations. The modelling of their integrated properties (light) permits easy testing, for different input prescriptions in the galaxy's characteristics (e.g., different masses, star formations, initial mass function, physical processes, etc.), in the reproduction of basic observational constraints.

Our main goal is the derivation of a tool that reproduces observational integrated properties of early-type galaxies by means of the EPS technique. Assigning a SED to the SSP and convolving it with the photometric system filters, the photometry of more complex systems, i.e. ETGs in our specific case, is obtained from the contribution of these different SSPs.

This self-consistent chemo-dynamical treatment allows to derive the optical SED for the simulation end-products with minimal assumptions. Taking advantage of this, we compare these results for an elliptical galaxy in our simulation with the observational data at optical wavelengths directly and quantitatively.

For all models, as a further step, we examine the resulting optical and IR photometric properties and their evoltuion in a cosmological context, comparing our results with observational data at high redshift selected from major surveys databases.

Moreover, we create artificial images of the simulated galaxies and investigate both radial profiles in the photometric properties as well as structural parameters that we derive from analyzing these synthetic projected bi-dimensioanl images.

The major aim of this thesis is to validate the analysis techniques that we intend to apply to a

set of simulations (under preparation) of comparable numerical resolution, as well as to identify potential disagreements between simulations and observations that may prompt a radical revision of our photometric tool or of the adopted cosmological model.

The outline of this thesis is as follows.

Chapter 1 resumes the most important characteristics of ETGs derived from observational evidences. Their origin and evolution within a cosmological context, still matter of debate, are briefly resumed. As ETGs are known to be homogeneous, they follow some empirical relations; we describe the most important of these scaling laws.

In **Chapter 2** we introduce the basic principles of the evolutionary synthesis technique: a very powerful tool, used throughout the thesis for computing the spectro-photometric integrated properties of the simulated galaxies. We describe the adopted stellar evolutionary models and spectral library that combined together enable us to apply the stellar EPS technique to the three-dimensional cosmo-chemo-dynamical models derived from the numerical simulations, and trasform the simulated models into the observational plane.

In **Chapter 3** we describe the SSPs, as they are the building blocks of the EPS technique, and the procedure followed to determine their spectral energy distributions. We also review the method adopted for performing synthetic photometry for the derivation of magnitudes and colors of the SSPs in a given magnitude system and photometric filter passband, mentioning the database we have at disposal for our study.

Chapter 4 deals with the spectro-photometric synthesis and the SED derivation of the simulated galaxies from the UV to the IR domain and their modeling within an evolutionary cosmic scenario. We firstly describe the numerical code that follows the stellar formation and evolution of a galaxy, an early-type galaxy in the specific case. In the second part we show how we derive the photometric evolution in the rest-frame for the three simulated models. We show the intregrated spectra, the magnitudes and colors derived and their evolution for two photometric systems: the Bessell-Brett and the Sloan Digital Sky Survey (SDSS).

In **Chapter 5** we present a multi-wavelength study of optical and near-IR high-z photometric properties of the ETGs and compare the results with a sample of galaxies selected from two different recent surveys. We describe how we make the selection of elliptical galaxies from the COSMOS and GOODS databases.

In **Chapter 6** we describe how we derive two-dimensional artificial images starting from the three-dimensional simulated galaxies, images that resemble observable data and can be analyzed in a similar manner. Isophotal analysis via Fourier and Sérsic is applied for inferring the photometric properties of the models galaxies at our disposal.

The results are tested on the three simulated elliptical galaxies: we derive morphological and

structural parameters that compared with a sample of elliptical galaxies selected from the SDSS allow to establish the consistency of our models with photometric constraints. These parameters are compared within the scaling relation, the Kormendy relation in particular.

Finally, in **Chapter 7**, we discuss the main results, and some future plans are drawn.

Chapter 1

Early-Type Galaxies

The origin and evolution of elliptical galaxies as part of *Early-Type Galaxies* (ETGs) cathegory is still a quite controversial debate (Chiosi (2000)). Spheroidal systems are of interest in their own right as they contain more than half of the total stellar mass in the local universe (Fukugita et al. 1998). Giant ellipticals are the most massive stellar systems in the local Universe, they appear to define a homogeneous class of objects which predominantly consists of uniformly old and red populations, which implies that they must have formed at high redshift, have negligible amounts of gas and very little star formation.

There is strong observational evidence that old, massive red and metal-rich proto-ellipticals are already in place at $z \sim 2-3$ and that the present-day early-type galaxies formed most of their stars well before a redshift $z = 1$ (Searle et al. (1973); Brinchmann & Ellis (2000); Treu et al. (2005); van der Wel et al. (2005)). Moreover, the current rates of star formation in these systems are quite low, the rates increasing sharply into the past (Butcher & Oemler (1978); Dressler (1980)). These ETGs are therefore likely to be good probes of galaxy assembly, star formation and metal enrichment in the early Universe.

Elliptical galaxies constitute a rather uniform family of stellar spheroids whose dynamical and photometric properties satisfy a number of *Scaling Relations* and whose detailed internal structure appears to vary weakly but systematically with galaxy mass.

Perhaps the most important of such scaling relations is the Fundamental Plane (FP), a tight correlation between the luminosity, size, and velocity dispersion that has been extensively used as a sensitive distance indicator (Djorgovski & Davis 1987; Dressler et al. 1987). The existence of the FP is believed to reflect largely the virial theorem, as applied to systems where the dark matter content, as well as, perhaps, age and metallicity, varies monotonically as a function of luminosity.

The small scater in the FP (e.g. Jorgensen et al. (1996)) and its apparent lack of evolution with redshift (Franx 1995; van Dokkum & Franx 1996; Bender 1997; Ellis et al. 1997; van

Dokkum et al. 2000), the homogeneity (Bower et al. 1992), and the evidence for short (< 1 *Gyr*) star formation timescales in these systems, all indicate that the bulk of stellar population in early-type galaxies indeed formed at high redshift ($z > 2$).

Dynamical and photometric indicators also vary with luminosity: bright elliptical galaxies are typically slowly rotating triaxial structures supported by anisotropic velocity dispersion tensors, whereas rotation is thought to play a more substantial role in the dynamics of fainter elliptical galaxies (Davies et al. 1983; Bender & Nieto 1990; Halliday et al. 2001). This dynamical distinction is reflected in isophotal deviations from perfect ellipses: fast-rotating spheroidals are usually 'disky', in contrast with the 'boxy' isophoptal shapes of slowly rotating systems (Bender 1988). Such deviations, although significant and robustly measured, are usually small, and simple concentric ellipsoidal models provide a rough but reasonable description of the structure of many elliptical galaxies. This structural trend observed holds important clues to the formation and evolution of elliptical galaxies and is not straightforward to account for in traditional models of elliptical galaxy formation.

1.1 Origin and Evolution

One of the major challenges in modern astrophysiscs is to understand the origin and the evolution of galaxies, the bright elliptical ones in particular, in the context of a Universe dominated by Cold Dark Matter (CDM), some kind of Dark Energy in form of the Cosmological Constant Λ, and containing a suitable mix of baryons and photons. In this scenario, in which cosmic structures are formed by the gravitational collapse of Dark Matter and are organized in a hierarchy of haloes inside which baryons dissipate their energy and collapse to form luminous systems, the formation of early-type galaxies can be reduced to the following schemes (Peebles 2002; Schade et al. 1999).

The classical *monolithic scenario* of galaxy formation supposes and predicts that all early-type galaxies form at high redshift ($z >> 1$) as a result of rapid and dissipationless collapse of a large mass of gas transformed into stars. In the model first proposed by Eggen et al. (1962) and then refined and implemented (see Larson (1975), Arimoto & Yoshii (1987), Bressan et al. (1994), Chiosi & Carraro (2002)), galaxies undergo a single and short but intense burst of star formation episode, ever since followed by passive evolution of their stellar populations to the present day. This scenario results in the vision of all elliptical galaxies being old, relaxed systems with ages around $12 Gyr$. This simple model accounts naturally for the old apparent ages of spheroid stars, for their high densities, and for the weak evolution in the spheroidal population properties with time.

In favour of this scheme are the observational data that convincingly hint for old and homo-

geneous stellar populations (see Chiosi (2000) for a recent review of the subject). It is worth mentioning, however, that Kauffmann et al. (1993) and Barger et al. (1999) argue for the presence of recent evolution in the stellar populations of elliptical galaxies.

This scenario successfully explains the tightness of the fundamental scaling relations that elliptical galaxies obey, like the color-magnitude realtion and the fundamental plane, as well as the evolution of these relations as a function of redshift. The optical properties of early-type populations and their strict obedience to simple scaling relations are indeed remarkably consistent with such a simple formation scenario.

While theoretical arguments might be compelling, the strongest evidence for the role of interactions in shaping early-type galaxy evolution and inducing star formation comes from observations. This formation mechanism fails to explain some recent observational evidence which has become available with the advance of more detailed data from present day surveys. These indicate that the star formation histories of at least some early-type galaxies, and perhaps the early-type population as a whole, deviate strongly from the expectations of the monolithic collapse paradigm, both in terms of their structural evolution and the star formation experienced by them over the whole Hubble time. It is less successful at explaining the detailed luminosity dependence of their dynamical properties, the apparent scarcity of very large star starbursts in the high-redshift universe, and the origin of dynamical peculiarities suggestive of recent accretion events.

While it reproduces the optical properties of early-type galaxies remarkably well, a monolithic star formation history does not fit quite well with the currently accepted ΛCDM galaxy formation scenario, in which galaxy mass is thought to accumulate over the lifetime of the Universe through both quiescent and merger-driven star formation. There is not yet a general consensus on how elliptical galaxies formed. A key feature of CDM-like theories is that massive dark matter halos are assembled by mergers of low mass halos. However, the role of mergers in structuring the stellar distributions of galaxies is still unclear.

The *hierarchical scenario* suggests instead that massive spheroidal galaxies are the end product of subsequent violent mergers of preexisting smaller subunits, over time scales almost equal to the Hubble time in the particular cosmological model used. In this scenario, the epoch of assembly of elliptical galaxies differs markedly from the epoch of formation of their constituent stars, and high density of elliptical galaxies is ascribed to the effects of dissipation during the formation of the progenitor disks. As the look-back time increases, the density in comoving space of bright (massive) elliptical galaxies should decrease by a factor 2 to 3 (e.g. White & Rees (1978), Kauffmann et al. (1993)).

This model accounts naturally for the scarcity of very bright elliptical progenitors at high redshift, for the rapid evolution of the galaxy population with look-back time, and for the pres-

ence of dynamical pecularities. In favour of this view are some observational evidences that the merger rate likely increases with $\sim (1+z)^3$ (Patton et al. 1997) together with some hint for a color-structure relationship for E & S0 galaxies: the color becomes bluer at increasing complexity of a galaxy structure. This could indicate some star formation associated to the merger event. Finally, there are the many successful numerical simulations of galaxy encounters, mergers and interactions (e.g. Barnes & Hernquist (1996)).

It is, on the other hand, less successful at explaining the apparent old ages of stars in elliptical galaxies and their uniformity in their dynamical properties. Nevertheless, contrary to the expectation from this model, the number density of elliptical does not seem to decrease with the redshift, at least up to $z \simeq 1$ (Im et al. 1996).

There is a third scheme named *dry merger* view, in which bright ellipticals form by encounters of quiescent, no star forming galaxies. This view is advocated by Bell et al. (2004) who finds that the B-band luminosity density of the red peak in the color distribution of galaxies shows mild evolution starting from $z \simeq 1$. As old stellar populations would fade by a factor 2 or 3 in this time interval, and the red color of the peak tells us that new stars are not being formed in old galaxies, this mild evolution hints for a growth in the stellar mass of the red sequence, either coming from the blue-peak galaxies in which star formation is truncated by some physical process, or by "dry mergers" of smaller red, gas-poor galaxies.

Finally, a fourth hybrid scenario named *revised monolithic* has been proposed by Schade et al. (1999), who suggests that a great deal of the stars in massive galaxies are formed very early-on at high redshift and the remaining few ones at lower z. The revised monolithic ought to be preferred to the classical monolithic, as some evidences of star formation at $0.2 \leq z \leq 2$ can be inferred from the presence of the emission line of [OII], and also as the number frequency of early-type galaxies up to $z \simeq 1$ seems to be nearly constant.

1.2 Scaling Relations

Among all galaxy families, ETGs (elliptical and S0), show the most precise regularities: they are similar in their structural and dynamical properties, as follows from spectroscopic and photometric observed properties. ETGs have observable quantities of the stellar content, as colors, luminosities, half-light radii, velocity dispersions, and surface brightnesses, all these are correlated and satisfy a few but fundamental empirical relations known as the *Scaling Laws*.

The Fundamental Plane

Elliptical galaxies in the local Universe are known to populate the *Fundamental Plane* (FP) (Djorgovski & Davis (1987); Dressler et al. (1987)), in the three-dimensional space defined

by the effective radius R_e, the mean surface brightness SB_e within the effective radius ($SB_e = -2.5\log < I_e > +const$; I is the surface brightness in linear flux), and the central velocity dispersion σ_0. The FP is described by:

$$\log R_e = \alpha \log \sigma_0 + \beta SB_e + \gamma \tag{1.1}$$

where R_e is in *kpc*, σ_0 in *km* s^{-1}, and SB_e in *mag* $arcsec^{-2}$. The coefficients are different for each filter bandpass, and typical values in the Johnson *B*-band are, for example, $\alpha = 1.25$; $\beta = 0.32$ and $\gamma = -8.895$ (Bender et al. 1998).

The existence of the empirical scaling described by the FP has strong implications in terms of galactic evolution and formation theories. For example, the FP suggests that the distributions of dark and luminous matter are related, since σ_0 depends on the total gravitational potential, whereas SB_e and R_e trace only the stellar mass. The FP can be explained in terms of homology of the virial theorem, and of the existence of a well-defined relation between luminosity and mass (Faber et al. 1987). The remarkable fact is the variation of the coefficinet α in the different filter bandpasses, and the almost constant value of β (Bernardi et al. 2003a). The values of α and β do not agree with what is expected form the virial theorem and homology, which makes the well-known problem of the tilt of the FP. Clusters and field elliptical galaxies are found to populate a thin plane in this three-dimensional space, slightly 'tilted' relative to the plane expected from the virial theorem, as applied to homologous systems.

The scaling laws are empirical relations for ETGs that correlate photometric and structural parameters of galaxies, the projection of the FP onto a plane gives the following relations.

The Faber-Jackson Relation

The *Faber-Jackson* (FJ) relation (Faber & Jackson 1976) is an empirical correlation of the total luminosity with the central velocity dispersion σ_0. As these are two of the three variables defining the FP, this relation can be seen as the projection onto the $\sigma_0 - L_e$ plane:

$$L_e \sim \sigma_0^4. \tag{1.2}$$

The FJ relation indicates that the projected velocity dispersion increases with galaxy luminosity.

Kormendy Relation

The *Kormendy relation* (Kormendy (1977),Djorgovski & Davis (1987)) relates surface brightness $< \mu >_e$ and effective radius R_e, also a projection of the FP, that in terms of the effective luminosity I_e gives:

$$R_e \propto I_e^{-0.83}. \tag{1.3}$$

Many studies have confirmed that the luminous ETGs in clusters follow approximately the relation $< \mu >_e = \log R_e + const$ found by Kormendy with a slope of ~ 3 and an intrinsic scatter of $0.3 - 0.4$. The $< \mu >_e - \log R_e$ data for galaxies in clusters at an increasing redshift have been claimed to be consistent with a passively evolving stellar population (Bower et al. (1992), Aragon-Salamanca et al. (1993), Bender et al. (1996), van Dokkum & Franx (1996), Jorgensen & Hjorth (1997), Ziegler & Bender (1997), Bender et al. (1998), van Dokkum et al. (1998)). On the other hand, some studies have also claimed that the data are consistent with the hierarchical evolutionary scenario ()). La Barbera et al. (2003), working with ETGs in cluster at different redshift, found that the slope in the relation is almost invariant up to $z \sim 0.64$ with a coefficient of $\sim 2.91 \pm 0.08$. The homogeneity and the invariance with redshift of these distributions is also suggested by the analysis of the SDSS data by Bernardi et al. (2003b).

Chapter 2

Evolutionary Synthesis Technique

With the exception of the nearest ones, the study of the galaxies is based on the information included in their integrated light, since the totality or the majority of their population cannot be resolved into single stars. This means that the integrated Spectral Energy Distribution (SED) must be calculated to obtain integrated magnitudes, colors and narrow band indices of the single models.

There are different approaches able to interpret integrated colors and spectral energy distribution features of the galaxies. O'Connell (1986) discusses two possible approaches to the spectral synthesis of an integrated galaxy spectrum:

(i) *optimizing synthesis models* (or *Empirical synthesis*). This method by means of a library of stellar spectra (either observed or theoretical) tries to find the mix of stars which minimize the differences between the theoretical and observed spectral energy distributions. The method does not allow to follow the evolution of the system and suffers of a certain degree of ambiguity in the uniqueness of the results (McClure & van den Bergh 1968; Faber 1972; Turnrose 1976; O'Connell 1980; Pickles 1985; Fanelli et al. 1987; Fanelli et al. 1988).

(ii) *Evolutionary population synthesis* (EPS) whose primary goal is the construction of the time-dependent distribution of stars in the theoretical Color Magnitude Diagram (CMD), from which the time-dependent history of the integrated spectral energy distribution (SED) can be easily obtained from adding up the spectra of individual stars.

The *evolutionary population synthesis method*, adopted in this thesis, have been introduced for the first time by Tinsley (1968) [see Tinsley (1980a) and Bruzual & Charlot (1993) for review]. Key ingredients for the EPS method are:

- the library of evolutionary tracks;

- the library of stellar spectra.

The stellar evolutionary tracks are used to calculate isochrones in the CMD and the relative proportions of stars in the various evolutionary phases, whereas the spectral library to derive the integrated spectral energy distribution and, in turn, magnitudes, colors in suitable pass bands (see next Chapter 3 for all details), for the single stellar population.

The EPS method is particularly powerful in combination with a chemical model from which the history of star formation and chemical enrichment can be taken and plugged into the EPS code to calculate the integrated spectral energy distributions (see for instance Bressan et al. (1994), Tantalo et al. (1996), Tantalo et al. (1998) and references therein and Section 2.3).

The quality of the evolutionary population synthesis (EPS) models depends on the quality and completeness of the library of stellar tracks in use and on the technique adopted to calculate isochrones in the color-magnitude diagram (CMD).

Charlot et al. (1996) compare several evolutionary synthesis models for elliptical galaxies, and discuss some of the limitations associated with them. The most serious are the treatment of stars in post-main sequence evolutionary stages, the poorly-determined temperature scale for the red giant branch and cool stars, and the lack of complete and accurate libraries of stellar spectra, especially for cool stars and non-solar metallicities.

We have adopted the data-base of stellar tracks very close to the ideal library which should include models calculated with modern physical input (opacity, nuclear reaction rates, neutrino losses, mixing schemes, etc.), extended to the latest evolutionary phases, and encompass large ranges of stellar masses and chemical compositions. In addition to this, we make use of a spectral library which extends over a large range of effective temperatures, gravities and chemical compositions. Both libraries are described in more detail below.

2.1 Library of Stellar Models

The availabilty of large sets of stellar evolution models spanning a wide range of stellar masses and initial chemical compositions is a necessary prerequisite for any investigation aimed at interpreting observations of galactic and extragalctic, resolved and unresolved stellar populations. A reliable library of stellar evolution models used to study stellar populations in various environments has to satisfy at least three main criteria: (i) the input physics has to be up to date and the treatment of physical processes has to be adequate and as much accurate as possible, (ii) the set of models has to be homogeneous, in the sense that all evolutionary phases and initial chemical compositions have to be computed with the same evolutionary code and the same physical framework, and (iii) the models have to reproduce as many empirical constraints as possible.

For the purposes of this thesis, we consider the large grid of stellar evolutionary tracks

presented by Girardi et al. (2000) which are suitable to modeling star clusters and galaxies by means of population synthesis, and list the main characteristics of the model library. The set of tracks considered, i.e. those with solar-scaled mixtures of abundances (same abundance ratios as in the solar mix), is for stars that cover a very large range of initial stellar masses that goes from 0.15 $M_{\odot}$ to 120 $M_{\odot}$. The choice for the chemical composition Z and the helium content Y parameters is made according to the helium-to-metal enrichment ratio law $\Delta Y/\Delta Z = 2.25$ so that $Y = 0.23 + 2.25Z$.

2.1.1 Input physics

The input physics is homogeneous for all stellar tracks in the grids, briefly, they are computed with consistent opacities over the whole range of temperatures, equation of state, a constant helium-to-metal enrichment ratio $\Delta Y/\Delta Z$, and mass loss from massive stars. Main characteristics are described in Girardi et al. (2000).

Initial chemical composition. Stellar models are assumed to be chemically homogeneous when they settle on to the zero age main sequence (ZAMS). The models stand on the enrichment law $\Delta Y/\Delta Z = 2.25$, in this way the metal Z, the helium Y, and the hygrogen X mass fractions, are chosen according to a fixed helium-to-metal relation, $Y(Z)$: $Y \sim 0.23 + 2.25Z$. The values of [Z,Y,X] chosen are listed in Table 2.1. For a fixed value of total metallicity Z, the fractions of

Table 2.1: Initial chemical composition of the stellar models.

Z	0.001	0.0004	0.001	0.004	0.008	0.019	0.04	0.07	0.1
Y	0.23	0.23	0.23	0.24	0.25	0.273	0.32	0.39	0.455
X	0.77	0.77	0.769	0.756	0.742	0.708	0.64	0.54	0.445

different metals follow a solar-scaled distribution (the solar-scaled abundances ratios of metals) and are taken from Grevesse & Noels (1993) as adopted in the OPAL opacity tables.

Opacities. The radiative opacities are from the OPAL group (Rogers & Iglesias 1992; Iglesias & Rogers 1993) for temperatures higher than $\log(T/K) = 4.1$ and from Alexander & Ferguson (1994) for $\log(T/K) < 4.0$. In the temperatue interval $4.0 < \log(T/K) < 4.1$, a linear interpolation between the opacities derived from both sources is adopted.

Equation of state. The equation of state (EOS) for temperatures higher than 10^7 K is that of a fully-ionized gas, including electron degeneracy as described by Kippenhahn et al. (1965). For temperatures lower than 10^7 K they adopt the Mihalas et al. (1990) EOS. They consider only the four most abundant metal species, i.e. C, N, O, and Ne.

Reaction rates and Neutrino losses. The nuclear reactions involve all the important reactions

of the pp and CNO chains, and the most important alpha-capture reactions for elements as heavy as Mg. The reaction rates are from Caughlan & Fowler (1988), but for $^{17}O(p,\alpha)^{14}N$ and $^{17}O(p,\gamma)^{18}F$, for which they use the most recent determinations by Landre et al. (1990). The energy loss by pair, plasma, and bremsstrahlung neutrinos, important in the electron-degenerate stellar cores are from Munakata et al. (1985) and Itoh & Kohyama (1983).

Convection. The energy transport in the outer convective zone is described according to the theory of Böhm-Vitense (1958). The mixing length parameter α is calibrated by means of the solar model. The extension of convective boundaries is estimated by means of an algorithm which takes into account overshooting from the borders of both core and from the lower boundary of the convective zones, as described in Bressan et al. (1981) and Alongi et al. (1991). The main parameter describing overshooting is its extent Λ_c across the border of the convetive zone, expressed in units of pressure scale height. Overshooting at the lower boundary of convective envelopes is also considered (see Alongi et al. (1991)).

Mass loss by stellar wind. Mass loss by stellar winds cannot be neglected in massive stars (Chiosi et al. 1992); therefore, for stars with initial mass between 12 $M_\odot$ and 120 $M_\odot$ the evolutionary models are computed taking into account mass loss according to the rates by de Jager et al. (1988) from the main sequence up to the so-called de Jager limit in the HRD. Although significant mass loss by stellar wind may occur during the Red Giant Branch (RGB) and Asymptotic Giant Branch (AGB) phases, models of low and intermediate mass stars are computed at constant mass. In low mass stars passing from the tip of the red giant branch (T-RGB) to the Horizontal Branch (HB) or clump, mass loss by stellar winds is included according to Reimers (1975) with the free parameter $\eta = 0.45$.

2.1.2 Evolutionary phases

The evolutionary phases covered by the grids extend from the Zero Age Main Sequence (ZAMS[1]) up to either the start of the thermally pulsing asymptotic giant branch (TP-AGB) phase or carbon ignition phase, depending on their initial mass. The models evolve from the ZAMS at constant mass. The evolution through the whole H- and He-burning phases is followed in detail.

In the case of stellar masses lower than 0.6 $M_\odot$, the main sequence evolution takes place on time scales much larger than a Hubble time, for these tracks the computations are stopped at an age of 25 *Gyr*: stars evolve very little during the Hubble time.

In low-mass stars with $M > 0.6\ M_\odot$, the evolution is interrupted at the stage of the He-flash in the electron degenerate hydrogen exhausted core, it is then restarted from a Zero Age

[1]The ZAMS model is defined to be the stage of minimum T_{eff} along the computed track; it follows a stage of much faster evolution in which the pp-cycle is out of equilibrium, and in which gravitation may provide a non negligible fraction of the radiated energy.

Horizontal Branch ZAHB model with the same core mass and surface chemical composition as the last RGB model, and finally followed up to the thermally pulsing AGB phase.

In intermediate-mass stars, the evolution goes from the ZAMS up to either the beginning of the TP-AGB phase, or at the onset of the carbon ignition in a helium exhausted core in the case of the most massive models (i.e. those with masses higher that about 5 $M_{\odot}$).

These grids of stellar tracks constitute the starting point of the isochrones: they give effective temperatures and luminosities as a function of time for different values of mass and metallicity. For each evolutionary track, we have the corresponding information: stellar age, surafce luminosity, effective temperature, surface gravity, and stage (indicating particular evolutionary stages).

2.1.3 Isochrone Synthesis

As mentioned before, the set of stellar models described above is used to calculate the isochrones, which enable the computation of integrated magnitudes and colors of single stellar populations in a defined photometric system.

From the tracks presented in Girardi et al. (2000), Girardi (2003, private communication) constructed the isochrones by means of the procedure described in Bertelli et al. (1994), that is adopting the algorithm of 'equivalent evolutionary points'.

The dense grid of stellar tracks allows to construct detailed isochrones at small age steps ($\Delta logt = 0.05$). This fine age spacing makes the models suitable for the simulation of synthetic color magnitude diagrams. The age range is large enough to describe young clusters and associations as well as globular clusters and galaxies.

The initial point of each isochrone is the 0.15 $M_{\odot}$ model in the lower main sequence. The terminal stage of the isochrones is either the TP-AGB for $M < 5\ M_{\odot}$ (ages of $\sim 10^8\ yr$), or C-ignition in the core for the remaining stars.

For the use with single short burst stellar populations, isochrones have a basic advantage over the stellar evolutionary tracks they are based on. Because tracks are only available for typically 50 (or less) stellar masses, drastic changes in the luminosity evolution of an SSP occur when all stars of a certain mass collectively climb on the red giant branch or die. Between reasonably defined equivalent evolutionary stages of two stellar masses with evolutionary tracks available, isochrones are interpolated in terms of

$$\log L = \log(L(m_i, \mu, \tau_\mu)) \tag{2.1}$$

$$\log T_{eff} = \log(T_{eff}(m_i, \mu, \tau_\mu)) \tag{2.2}$$

where m_i is the initial mass for track i, μ the defined physical phase of evolution and τ_μ the relative duration in this phase. It is then possible to interpolate both in luminosity and temperature

between two adjacent masses.

For each isochrone, of a given age and metallicity, we have the following data: the age, the initial and actual stellar masses in solar units along the isochrone (the initial mass is useful for population synthesis calculations, since together with the initial mass function (IMF) it determines the relative number of stars in different sections of the isochrones: the actual mass at the specified age is computed taking into account mass loss), the surface luminosity, the effective temperature, and the surface garvity.

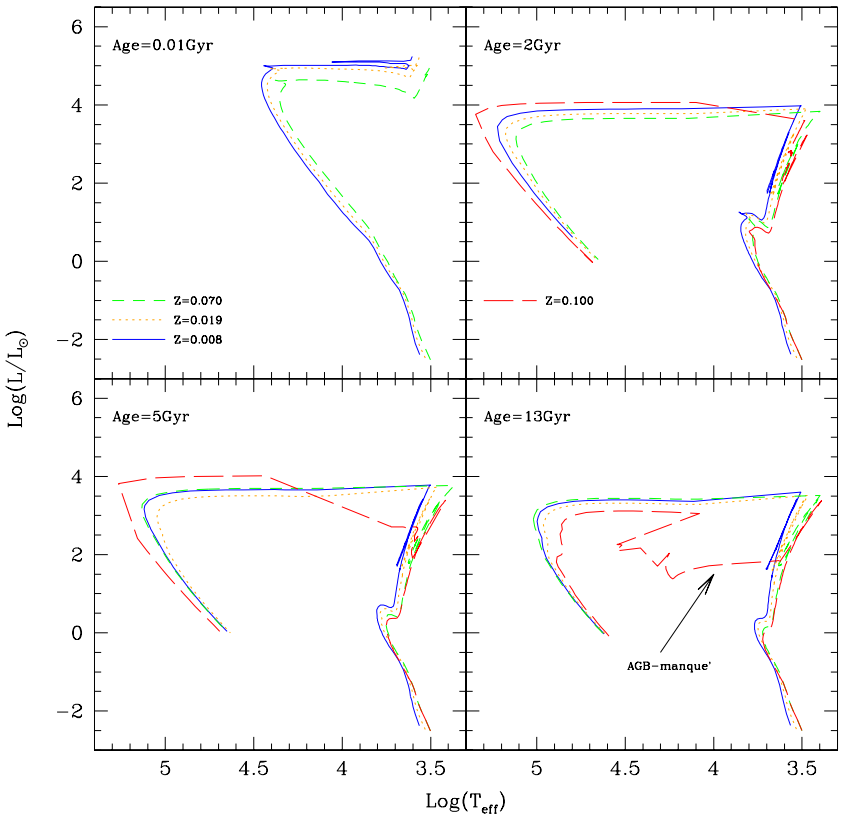

Figure 2.1: Isochrones in the HR diagram for different ages of 10^7, 2×10^9 *yr*, 5×10^9 *yr*, and 13×10^9 *yr* and for four different values of metallicity, $Z=0.008$, $Z=0.019$, $Z=0.07$, and $Z=0.1$. At the age of 13×10^9 *yr* the AGB-manqué phase is indicated in correspondence of the $Z=0.1$ metallicity.

Many characteristics of the stellar models depend on the chemical composition and in particular some of the features that can be observed are the following.

At increasing metallicity, the mean sequence Turn-off gets redder and fainter, the T_{eff} range covered by the sub-giant branch (SGB) decreases, and the RGB bends toward lower T_{eff}. The core He-burning phase gets redder at increasing metal content (see Figure 2.1).

The evolution of high metallicity stars of low mass is a subject of interest because they can provide the correct explanation of the UV-excess observed in elliptical galaxies. The high-metallicity ($\sim Z_{\odot}$) low-mass stars, after a normal He-burning phase (red-HB), skip the standard TP-AGB and soon after the early AGB phase is completed, proceed toward the WD regime; these are named P-EAGB.

At higher metallicictiies ($\sim 3Z_{\odot}$), the old HB stars of normal mass ($\sim 0.55-0.6\ M_{\odot}$) can spend a significant fraction of the core He-burning phase at high T_{eff} and subsequently skip the entire AGB phase to directly evolve toward the WD regime; these are named Hot-HB and AGB-manqué.

The physical explanation is that for a given M_{HB}, both the lower hydrogen content in the envelope and the enhanced CNO processing in the H-burning shell, because of the high metallicity, concur to burn out the envelope much faster than in stars of the same mass but lower metallicity and hence helium

In Fig. 2.1 are shown some isochrones of different metal content and for a few ages corresponding to the models described above.

2.2 Library of Stellar Spectra

In order to derive spectral energy distributions, integrated magnitudes, and colors, corresponding to a source of given luminosity, effective temperature, gravity, and chemical composition, one needs a library of stellar spectra as function of these parameters.

The spectral library considered in this thesis was put together by Girardi et al. (2002) adopting the ATLAS9 (Kurucz 1992) library of synthetic atmospheres: no-overshooting models calculated by Castelli et al. (1997) and subsequently extended by other authors.

The Kurucz library covers a wide range of the stellar atmospheric parameters: effective temperatures have a range of 3500 $K < T_{eff} < 50000\ K$, gravity of $0 < \log g < 5$, and the metallicity values considered are $[M/H]^2 = -2.5, -2.0, -1.5, -1.0, -0.5, 0.0, 0.5$. Models have solar-scaled abundance ratios, a microturbolent velocity $\xi = 2\ km\ s^{-1}$, and a mixing length equal to $\alpha = 1.25$. This region has subsequently been extended both for the low and high T_{eff}s values.

[2]Whenever necessary, the metallicity Z is converted into the logarithmic metal content by means of the approximate relation

$$[M/H] = \log(Z/X) - \log(Z_{\odot}/X_{\odot}), \tag{2.3}$$

with respect to the solar scaled composition, $Z_{\odot} = 0.019$, $X_{\odot} = 0.708$.

The spectral library contains the spectral energy distributions (SEDs), expressed in $erg\ sec^{-1}\ cm^{-2}\ \AA\ sr^{-1}$, which goes from 90 $\AA$ to 1.6×10^6 $\AA$, with a mean resolution of 20 $\AA$ ($\sim$ 10 $\AA$ in the UV region and up to $\sim$ 50 $\AA$ in the optical region).

Extension to high and low temperatures

The isochrones in the CMD sometimes happen to reach T_{eff} and gravities not included in the spectral library, for this reason they had been extended both to high and low temperatures (Girardi et al. 2002, for details).

The extension to the region covering the higher temperatures, for $T_{eff} > 50000\ K$, has been made by simply assuming black-body spectra. A good approxiamtion for wavelengths $\lambda < 912$ $\AA$.

On the other hand, the extension to lower temperatures is quite more composite. As synthetic spectra for M giants have problems, especially in the ultraviolet-blue reagion, Girardi et al. (2002) used empirical spectra for the M giant stars, and these are taken from Fluks et al. (1994). They cover the wavelength range from 3800 $\AA$ to 9000 $\AA$, outside this interval the spectra has been extended with a best fit also computed by them.

Once defined the library of M-giant spectra, Girardi et al. (2002) associated the effective temperature by using the scale favoured by Fluks et al. (1994) in which M giants cover the temperature range from 3850 K to 2500 K. These T_{eff} values are derived by fitting the observed spectra with synthetic model atmospheres of solar metallicity, and their scale is in excellent agreement with the empirical one from Ridgway et al. (1980).

The extension of the library of synthetic spectra for cool dwarf's atmospheres, that is stars of type M and later, is provided by Allard et al. (2000). These spectra cover the following T_{eff} interval: from 4000 K to 2800 K for metallicities $[M/H] = -1.5, -1.0, -0.5, 0.0$, and for gravity values of $\log g = 5.0$ and 5.5; from 2800 K to 50 K for the only value of metallicity $[M/H] = 0.0$, and for gravity values between $\log g = 3.5$ and 6.0.

2.3 Chemo-Evolutionary Synthesis Technique

We will introduce the method with which we are able to derive spectro-photometric integrated properties of Model Galaxies that have been simulated with a cosmo-chemo-dynamical code, according to the population synthesis approach.

The idea is that of developing a code that enables us to simulate the same sort of data that is released by some of the major campaigns of wide-field photometry conducted in recent years. Of primary importance are present and future data from the HST, GAIA, SDSS, GOODS, COSMOS surveys.

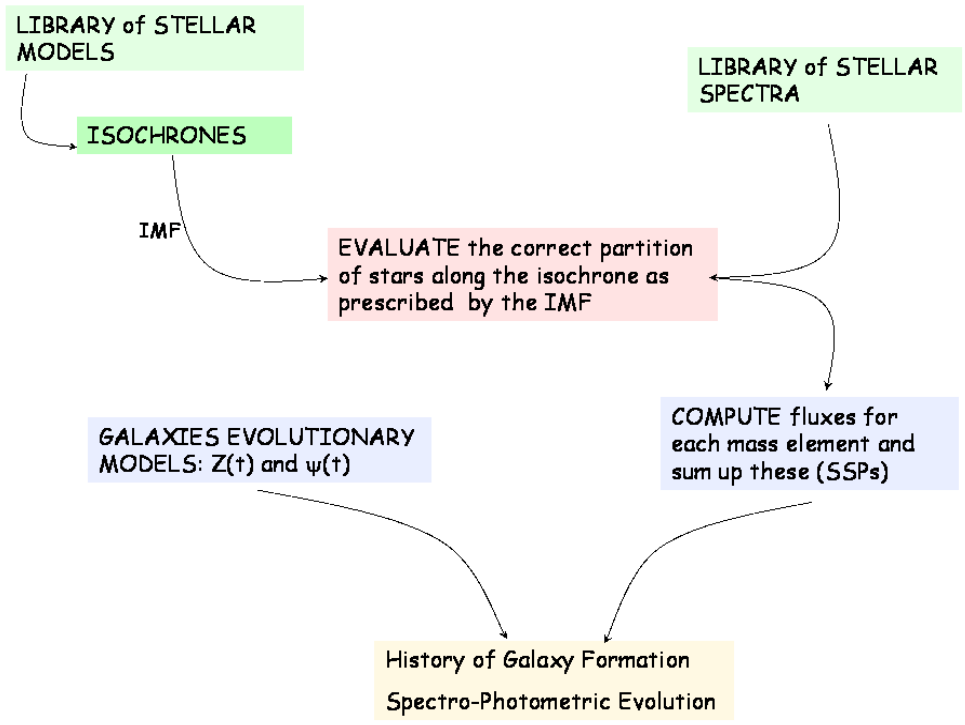

Figure 2.2: Diagram representing the evolutionary population synthesis technique: main ingredients and steps followed for the determination of the spectro-photometric properties.

Our main objective is to simulate the photometric integrated properties of early-type galaxies in several passband systems. For doing so we should be able to simulate the stellar population of the galaxy. To cope with this necessity we must adopt a code able to simulate the star formation history and the chemical enrichment of our galaxies.

This implies that we must include and describe all the ingredients necessary for computing the simulated photometric properties of the Galaxy Model.

A general scheme of the method applied is provided on Fig. 2.2. It makes use of the following main elements: a library of theoretical evolutionary tracks, a library of synthetic spectra, and a detailed description of the Simulated Galaxy components.

x The library of evolutionary tracks is pre-processed in form of theoretical isochrones (which give us the distribution of the stars in the CMD at given age, see Section 2.1).

Secondly, we need to consider a database of synthetic spectra of SSPs for different ages and chemical composition, and hence a database of magnitudes and colors (see Chapter 3). These are considered as ‘fixed input’, but can be easily changed in order to consider alternative sets of

data.

The third step consists in the combination of the database of SSPs SEDs with the Chemical Evolutionary Models that describe the star formation rate and the chemical enrichment of the simulated galaxy.

To this aim we have adopted the Cosmo-Chemo-Dynamical Model developed by the Padova Group (GALDYN) from which we get the star formation history (SFH) and the chemical enrichment (Z(t)) of the simulated galaxy. This output is fed into the photometric code.

The photometric code we have developed assigns to each star particle of the simulated galaxy the correspondig SED interpolated among the SEDs of the SSP database of different ages and metallicities. This means that we can provide the evolution of the photometric properties for all the star particles of the simulation. For what concerns the integrated properties, the spectrum of the whole galaxy is derived by making a summation over the assigned SED of all the single star particles.

From the integrated spectrum of the galaxy we derive the absolute magnitudes, colors, indices, etc., in a chosen photometric system, according to the synthetic photometry procedure adopted and described in Chapter 3. This allows the application of the procedure to a very wide set of photometric systems, provided they are broadband filter sets and deal with VEGA, AB or ST magnitude system. This calculation produces a 'photometric catalogue': we recover the rest-frame and cosmological evolution of magnitudes and colors for the set of model galaxies at our disposal.

Chapter 3

Synthetic photometry and SSPs

Simple stellar populations (SSPs) are single burst, single metallicity stellar populations, like star clusters, with all their stars having the same age and the same chemical composition. The evolution of these SSPs in terms of spectra and photometry are described by the evolutionary synthesis models.

SSPs are of interest for several reasons. They are used to test properties that range from a set of stellar evolutionary tracks to magnitudes and colors, against observations of star clusters that formed or are still forming in strong starbursts, that is from old globular clusters to young open clusters.

With the aid of the Evolutionary Population Synthesis Technique (EPS), evolutionary models for individual stellar generations with any Star Formation History (SFH) can directly be folded - in terms of luminosity or spectral evolution - to describe the composite stellar population of a galaxy, formed of stars with different ages and metallicities, and understand the spectro-photometric properties of these complex systems.

For this purpose, a complete library of spectra for SSPs of various ages and metallicities constitute a theoretical basis for population synthesis models. The EPS Technique searches for a particular linear combination of input spectra that gives best agreement with the observed spectrum of a galaxy with unknown SFH and from which photometric properties are derived. In this way, spatially resolved observable quantities are obtained from a superposition of SSPs.

In this thesis we make use of a set of SSPs of various metallicities and ages, that cover the Hubble time, and, with the aid of the EPS technique, that we describe here, recover the spectral and photometric evolution of the ETGs that derive from numerical simulations, along with the evolution of their integrated properties, as we will see in the next Chapter.

3.1 Fundamentals of Population Synthesis

In this section we will briefly describe the procedure followed to determine the spectral energy distribution (SED) of the SSPs.

The theory of stellar evolution provides the bases to build the function $l_{SSP}(\lambda,\tau,Z)$, the monochromatic luminosity of a SSP of age τ, and, starting from the tracking the physical properties of stars through age, it is possible to compute the relations connecting luminosity, effective temperature, and age for any star of given mass M and metallicity Z.

Evolutionary tracks describe (e.g. on the Herzsprung-Russel diagram) the properties of a single star of given mass M and metallicity Z as functions of the age t, while isochrones represent a picture of stellar properties 'frozen' at a given age τ and metallicity Z, for any mass M (see Fig. 2.1).

As the luminosity of a SSP is calculated by integrating along an isochrone of age τ, it has the dependence

$$l_{SSP} = [L(M,\tau,Z), T_{eff}(M,\tau,Z), G(M,\tau,Z), Z], \tag{3.1}$$

where L, T_{eff}, and G are the luminosity, the effective temperature, and gravity, respectively, of the stars of mass M lying on the isochron with age τ, and metallicity Z. For any star of mass M and metallicity Z, the relations between luminosity, effective temperature, and age are derived from the library of stellar models, while the luminosity $L(M,\tau,Z)$ emitted by a star is obtained from the library of stellar spectra.

The luminosity emitted by a simple stellar population of age (τ) is computed by summing the spectra of the stars populating the corresponding isochrone. While the precise shape of an isochrone is defined by the physics assumed to compute the theoretical evolutionary tracks, the proportions of stars in the different evolutionary stages along the isochrone are set by the adopted IMF, $\Phi(M)$, and by the lifetimes of stars in the various evolutionary phases.

In practice the SED of an isochrone is computed by dividing it in very small portions of luminosity and effective temperature ($\Delta\log L/L_{\odot}$, $\Delta\log T_{eff}$), corresponding to suitable intervals of ($\Delta\log M/M_{\odot}$, $\Delta\log g, \Delta N$), in the space of stellar physical parameters; where the number of stars per elemental interval of initial mass is defined as $\Delta N = \Phi(M)\Delta M$.

By integrating the contribution of each isochrone element along the whole isochrone, the integrated spectral energy distribution of an SSP is derived for any metallicity and age.

The stellar Initial Mass Function, $\Phi(M)$, where M is the stellar mass, is the distribution function of the masses of stars formed in one event and its determination relies on the transformation of the observed luminosity function (LF), $\Phi = dN/d\mathcal{M}$, i.e. the number of stars N per absolute magnitude interval $d\mathcal{M}$. It provides an essential diagnostic to understand the formation of stellar objects. It is an important ingredient because it determines the relative number of stars.

The classical IMF (Salpeter 1955), which describes mass distribution of the stars in the solar neighborhood, is parametrised as usual in the following way:

$$\frac{dN}{dM} = \Phi(M) \propto M^{-\alpha}, \tag{3.2}$$

where $\alpha = 2.35$, over the range of stellar masses from M to $M + dM$.

The normalization is

$$\int_{M_l}^{M_u} \Phi(M) dM = 1, \tag{3.3}$$

where M_l and M_u are the lower and upper mass limits in which the IMF has been defined.

Different prescriptions commonly used for the IMF are the power laws as Arimoto & Yoshii (1987), Kroupa (1998), and Kennicutt (1983) and the exponential ones of Larson (1998) (for solar neighborhood and steeper) and Chabrier (2001), these are presented in Appendix A.

Once the input physics is defined, the only free parameters in th SED for an SSP are those describing the IMF. The SSPs used in this thesis were obtained assuming a Kroupa (1998) or Salpeter (1955) IMF (see Table4.2).

3.1.1 Integrated SED for a SSP

Throughout this thesis, to every star of mass M on an isochrone of age τ and metallicity Z is associated an individual spectrum $(S_\star(\lambda, M, \tau, Z))$ extracted from the spectral library described in 2.2, appropriate for its effective temperature T_{eff} and surface gravity g ranges. This is done by interpolating the spectral energy distributions as a function of gravity, effective temperature and metallicity, and taking in consideration the emitting surface of the stars.

The spectra of all stars along an isochrone of given metallicity Z can be summed up, weighted with the IMF, $\Phi(M)$, to give the integrated monochromatic SED $S_{SSP}(\lambda, \tau, Z)$ of a SSP of metallicity Z at age τ

$$S_{SSP}(\lambda, \tau, Z) = \int_{M_l}^{M_u} S_\star(\lambda, M, \tau, Z) \Phi(M) dM \quad [erg\ s^{-1}\ \AA^{-1}]. \tag{3.4}$$

The total luminosity of a SSP is obtained by integrating the Eq. 3.4 over the wavelengths

$$L_{SSP}(\tau, Z) = \int_0^\infty S_{SSP}(\lambda, \tau, Z) d\lambda \quad [erg\ s^{-1}]. \tag{3.5}$$

We have at our disposal large number of SSPs with ages between 10^7 *yr* and 3×10^{12} *yr*, metallicities from $Z = 0.0001$ to 0.1, and for different presciptions for the IMF: Salpeter (1955), Arimoto & Yoshii (1987), Kennicutt (1983), Kroupa (1998), Larson (1998), Chabrier (2001). (See Appendix A for details on the IMFs.) The SED of each SSP has been computed by Tantalo (2005) adopting the library of stellar spectra assembled by Girardi et al. (2002). For each

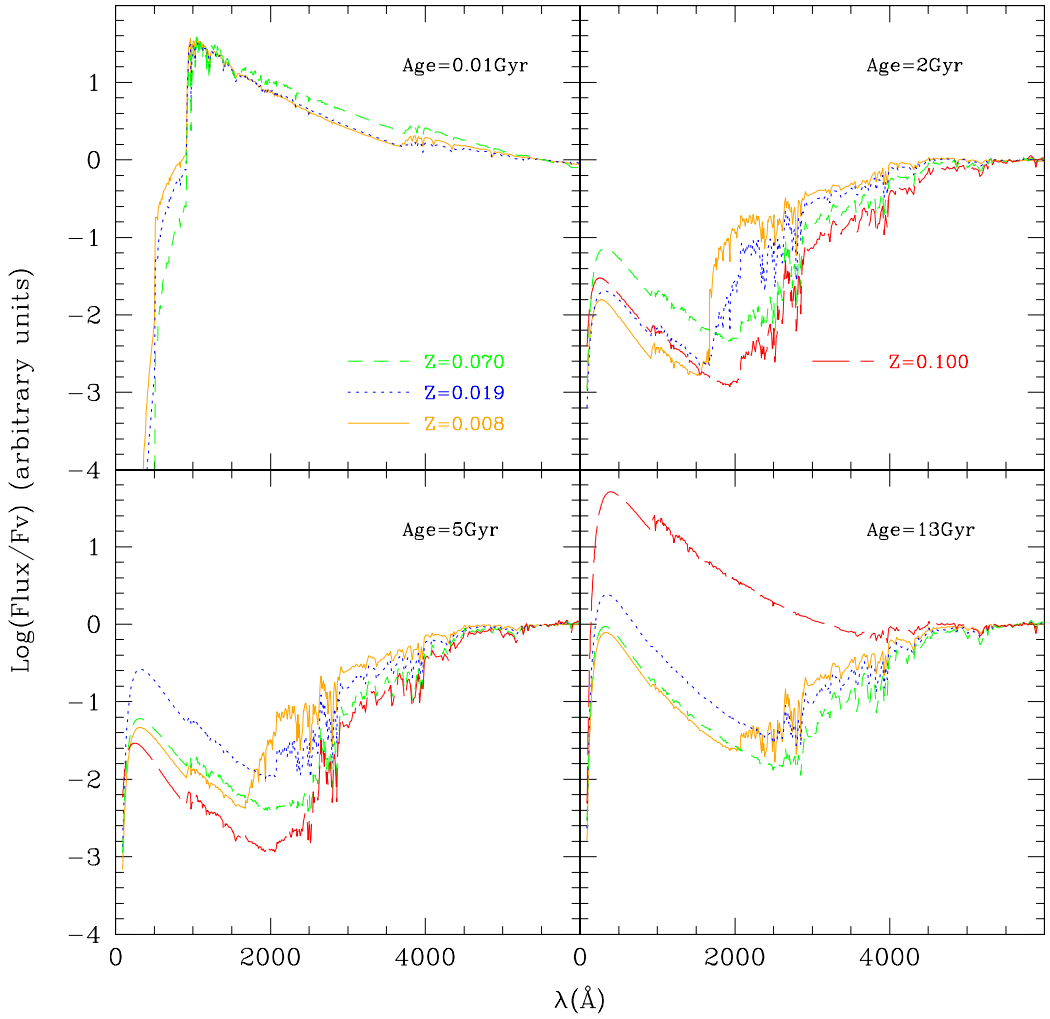

Figure 3.1: SEDs of SSPs for different ages of 10^7, 2×10^9 *yr*, 5×10^9 *yr*, and 13×10^9 *yr* and for four different values of metallicity, $Z=0.008$, $Z=0.019$, $Z=0.07$, and $Z=0.1$. All fluxes are normalized to the F_{5550} value.

metallicity we have at disposal tables of fluxes and magnitudes at varying age, for a chosen IMF.

Fluxes, and hence magnitudes, are calculated for the total mass of a SSP:

$$\int_{M_l}^{M_u} M\Phi(M)dM = M_{SSP} \tag{3.6}$$

where masses are expressed in solar units [$M_{\odot}$]. The total mass of the SSP depends on the IMF and the values of M_l and M_u (see Table A.1 in Appendix A).

SSPs are simple, given an IMF, they only depend on two parameters: age and chemical composition/metallicity. Of course, a single galaxy in the universe is not a SSP, since its star formation history is not going to be a single burst, nor its metallicity a single one. However, most (if not all) elliptical galaxies have formed their stellar populations at high redshifts in a very short duration of time and they have relatively uniform chemical compositions, thus their spectra can be correctly described by a superposition of SSPs.

As the spectro-photometric properties of composite systems derive from a superposition of SSPs, the features of these characterize directly the integrated properties of the more complex systems, for instance, galaxies. Moreover, characteristics of the single evolutionary tracks depend on the chemical composition and in particular some of the features that can be observed are the following.

The morphological properties of the stellar tracks reflect on the SED and hence on the integrated colors of the SSPs.

At young ages the UV region is dominated by the flux emitted by young massive stars, on the other hand at older ages is dominated by different emitters depending on the metal content. For the low metallicities the stars contributing to the UV flux are the classical P-AGB objects, at increasing metallicity the contribution from the AGB-manque and H-HB gets more and more important up to the extreme case of $Z = 0.1$ in which the UV flux is almost entirely generated by this type of objects.

In Fig. 3.1 is shown the spectral evolution of SSPs computed considering a Kroupa IMF, for different metallicities $Z = 0.008$, $Z = 0.019$, $Z = 0.07$, and $Z = 0.1$ [1] at the different ages of 0.01, 2, 5, and 13 *Gyr*, respectively. Enormous differences are seen both at young and old ages between SSPs of different metallicities.

3.2 Synthetic Photometry

By synthetic photometry is intended the derivation of photometric quantities based on stellar intrinsic spectra (theoretical for the most and empirical).

One of the primary aims of Evolutionary Population Synthesis (EPS) is that of explaining the photometric data, e.g. color-magnitude diagrams (CMD), luminosity functions, color histograms, of stellar populations and/or integrated properties of unresolved stellar populations. To allow a comparison between theory and data, the basic requirement is to provide the conversion of the theoretical models into the photometric observational domain so that more quantitative

[1] SSPs with metallicity $Z = 0.1$ are computed only starting from the age of 2 *Gyr*

and qualitative interpretations can be made of observations. That is, the output of the models, must be first converted in observable quantities, i.e. magnitudes, colors, indexes, etc.

In this section we will describe the method used to derive magnitudes and hence colors in a defined photometric system, given the SEDs of the SSPs and the filters for the photometric systems (e.g. Bessell-Brett, SDSS, along with any other system of which transmission curves are avalilable).

3.2.1 Integrated magnitudes

We describe briefly the generic formalism to be applied in order to derive aparent and absolute magnitudes in a wide variety of photometric systems.

For a star, the spectral flux as it arrives at the Earth, f_λ, is related to the flux at the stellar surface, f^s_λ, by

$$f_\lambda = \left(\frac{R}{d}\right)^2 f^s_\lambda, \tag{3.7}$$

where R is the stellar radius, d is its distance. Once f_λ is known, the apparent magnitude m_{S_λ}, in a given passband with transmission curve S_λ comprised in the interval $[\lambda_1, \lambda_2]$, is given by

$$m_{S_\lambda} = -2.5 log \left(\frac{\int_{\lambda_1}^{\lambda_2} \lambda f_\lambda S_\lambda d\lambda}{\int_{\lambda_1}^{\lambda_2} \lambda f^0_\lambda S_\lambda d\lambda}\right) + m^0_{S_\lambda}, \tag{3.8}$$

where f^0_λ represents a reference spectrum that reproduces a known apparent magnitude $m^0_{S_\lambda}$. In this way, f^0_λ and $m^0_{S_\lambda}$ completely define the zero-points of a synthetic photometric system.

In Eq. 3.8, the integrands $\lambda f_\lambda S_\lambda$ are proportional to the photon flux (i.e. the number of photons by unit time, surface, and wavelength interval) at the telescope detector. This kind of integration applies well to modern photometric systems that have been defined and calibrated using photon-counting devices such as CCDs.

However more traditional systems like the Bessell-Brett one, have been defined using energy-amplifier devices. In this case, energy integration, i.e.

$$m_{S_\lambda} = -2.5 log \left(\frac{\int_{\lambda_1}^{\lambda_2} f_\lambda S_\lambda d\lambda}{\int_{\lambda_1}^{\lambda_2} f^0_\lambda S_\lambda d\lambda}\right) + m^0_{S_\lambda}, \tag{3.9}$$

would be more appropriate to recover the original system. The differnce between energy and photon integration is usually very small, unless the passbands are extremely wide. The integration of photon counts is adopted.

The starting point to derive absolute magnitudes are extended libraries of stellar intrinsic spectra f^s_λ, as derived from atmosphere calculations for a grid of effective temperatures T_{eff},

surface gravities g, and metallicities Z. The library adopted in this thesis has been described in 2.2.

The absolute magnitude M_{S_λ} is derived for each star of known T_{eff}, g, Z, F_λ, the flux at the distance of $d = 10$ pc, and the stellar radius R, from Eqs. 3.7 and 3.8:

$$M_{S_\lambda} = -2.5log\left[\left(\frac{R}{10pc}\right)^2 \frac{\int_{\lambda_1}^{\lambda_2} \lambda F_\lambda S_\lambda d\lambda}{\int_{\lambda_1}^{\lambda_2} \lambda f_\lambda^0 S_\lambda d\lambda}\right] + m_{S_\lambda}^0. \tag{3.10}$$

The integrated absolute bolometric magnitude is derived from

$$M_{bol} = -2.5 \times \log\left(\frac{L_{SSP}}{L_\odot}\right) + M_{bol,\odot}, \tag{3.11}$$

where constants adopted are $M_{bol,\odot} = 4.72$ and $L_\odot = 3.844 \times 10^{33}$ $erg\ s^{-1}$.

3.2.2 Magnitude Systems: Reference spectra and zero points

By photometric zero-points are meant the constant quantities that one should add to instrumental magnitudes in order to transform them to standard magnitudes, for each filter S_λ. In the formalism adopted, the concept of instrumental magnitudes is not used, so such constants do need to be defined. By zero-points, are meant quantities in Eq. 3.8 that depend only on the choice of f_λ^0 and $m_{S_\lambda}^0$. They are constant for each filter and are responsible for the conversion of the synthetic magnitude scale into a standard system.

VEGA Magnitude System

As first magnitude system, we have based the calibration on the reference spectrum of Vega, and we will refer to this photometric system as the VEGA mag system.

This system offers a good approximation to many of the conventional photometric systems that use the spectrum of Vega to define the magnitude zero in any passband. In broadband photometry, the relevant passband integral is calculated first for the source spectrum and then again for the spectrum of Vega, and the ratio of the two results is converted to a magnitude.

It makes use of Vega (α Lyr) as the primary calibrating star. The most famous among these systems is the Bessell-Brett (*UBVRIJHKLMN* filters) one, that can be accurately recovered by simply assuming that Vega has an apparent magnitude $V = 0.03$ mag ($M_V = 0.48$), and all colors equal to 0.

Recently, composite spectra of Vega have been constructed by assembling empirical and synthetic spectra together. This has the precise scope of providing a reference spectrum for conversions between apparent magnitudes of real (observed) stars and physical fluxes.

We adopt the synthetic ATLAS9 model for Vega from Castelli & Kurucz (1994), with $T_{eff} = 9550\ K$, $\log g = 3.95$, $[M/H] = -0.5$, and microturbolent velocity $\xi = 2\ km\ s^{-1}$. In this case, the predicted fluxes at Vega's surface f_λ^S are rescaled to the Vega distance by the dilution factor (see Eq. 3.7):

$$\left(\frac{R}{d}\right)^2 = 6.25 \times 10^{-17} \tag{3.12}$$

If we assume the apparent Vega colors to be equal to zero in all passbands $\Delta\lambda$, we would obtain $Z_{\Delta\lambda} = 2.5 log\, f_{\Delta\lambda,Vega}$, and Eq. 3.8 would become

$$\begin{aligned} m_{VEGA,\Delta\lambda} &= Z_{\Delta\lambda} - 2.5 \log f_{\Delta\lambda} \\ &= -2.5 \log \frac{f_{\Delta\lambda}}{f_{\Delta\lambda,Vega}}. \end{aligned} \tag{3.13}$$

AB Magnitude System

The monochromatic AB magnitudes in the *AB* system were defined originally by Oke (1964) as

$$m_{AB,\nu} = -2.5 log\, f_\nu - 48.59. \tag{3.14}$$

This means that a reference spectrum of constant flux density per unit frequency

$$f^0_{AB,\nu} = 3.631 \times 10^{-20} \quad [erg\ s^{-1} cm^{-2} Hz^{-1}] \tag{3.15}$$

will have AB magnitudes $m^0_{AB,\nu} = 0$ at all frequencies ν. The zeropoint value is chosen for convenience so that the Vega AB_ν magnitudes are close to zero in the Johnson V passband.

This definition can be extended to any filter system, provided that we replace the monochromatic flux f_ν with the photon counts over each passband S_ν obtained from the star, compared to the photon counts that one would get by observing $f^0_{AB,\nu}$:

$$m_{AB,\nu} = -2.5 \log \left(\frac{\int d(\log \nu)\, f_\nu S_\nu}{\int d(\log \nu)\, f^0_{AB,\nu} S_\nu} \right), \tag{3.16}$$

otherwise expressed as

$$m_{AB,\nu} = -2.5 \log \left(\frac{\int d(\log \nu)\, f_\nu S_\nu}{\int d(\log \nu) S_\nu} \right) - 48.59, \tag{3.17}$$

where f_ν is expressed in $erg\ s^{-1}\ cm^{-2}\ Hz^{-1}$. Passing to wavelengths we derive the AB magnitudes

$$m_{AB,\lambda} = -2.5 log \left[\frac{\int_{\lambda_1}^{\lambda_2} (\lambda/hc)\, f_\lambda S_\lambda d\lambda}{\int_{\lambda_1}^{\lambda_2} (\lambda/hc)\, f^0_{AB,\lambda} S_\lambda d\lambda} \right], \tag{3.18}$$

where $f^0_{AB,\lambda} = f^0_{AB,\nu} c/\lambda^2$, and

$$\lambda_{pivot} = \sqrt{\frac{f_{AB,\nu}}{f_{AB,\lambda}} c} \tag{3.19}$$

is the pivotal wavelength that permits the transformation between frequencies and wavelengths.

3.3 Photometric Systems and Integrated Colors of SSPs

Several filter systems are implemented in our evolutionary synthesis code, from these we obatin photometric results that will eventually be compared with observed galaxies selected from the Surveys.

Together with the time evolution of SSP spectra, any filter system within the long wavelength range of our spectra from 90 $\AA$ through 160 μm is readily applicable. We have adopted the SSP database computed by Tantalo (2005), available online from the Padova Galaxies and Single Stellar Population Models (GALADRIEL) at *http://www.astro.unipd.it/galadriel/*.

The photometric systems adopted for the SSP database are the following:

- the Bessell-Brett
- the Hubble Space Telescope (NICMOS, WFPC2, ACS)
- the Sloan Digital Sky Srvey (SDSS)
- the GAIA mission
- the GALEX

Table 3.1: Available Systems in the GALADRIEL Database for SSPs

Photometric System	Magnitude System	Filters
Bessell-Brett	AB/VEGA	UBVRIJHKLMN
HST - NICMOS	AB/ VEGA/ST	32 filters
HST - WFPC2	AB/ VEGA/ST	36 filters
HST - ACS	AB/VEGA/ST	30 filters
SDSS	AB/VEGA/ST	ugriz
GAIA	AB/VEGA	G-band
GALEX	AB	FUV-NUV

In Table 3.1 are listed for each photometric system the corresponding magnitude system and filters adopted.

The first step toward the definition of the photometric system is to consider the transmission curves for each individual band. In this work we have considered for instance two photometric systems: the Bessell-Brett and SDSS for the VEGAmag and ABmag systems. The response functions for the varoius passbands, in which magnitudes and colors are calculated, are taken from the Asiago Database on Photometric Systems (ADPS[2]). In this way, knowing the spectrum of the source and the system response function, with this expression we can reprodue the natural magnitude system.

Bessell-Brett UBVRIJHKLMN Photometric System

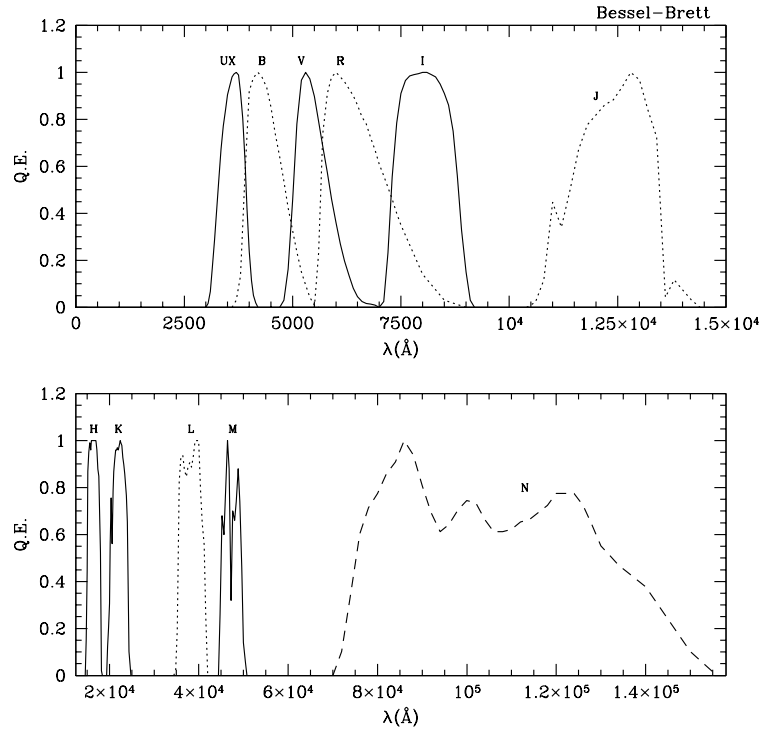

Figure 3.2: Filters for the UBVRI Bessell (1990) and JHKLM from Bessell & Brett (1988) photometric sytems. All curves are normalized to their maximum value.

.

[2]http://ulisse.pd.astro.it/Astro/ADPS

The transmission curves considered for this photometric systems are from Bessell (1990) for the *UBVRI* and from Bessell & Brett (1988) for the *JHKLMN*. The characteristics for the Bessell-Brett UBVRIJHKLMN photometric system are summarized in Table 3.2 and transmission curves are shown in Figure 3.2.

Table 3.2: Effective Wavelengths and FWHM for the Bessell-Brett system as specified in the ADPS database.

Band	U	B	V	R	I	J	H	K	L	M
λ_{eff} [Å]	3670	4360	5450	6380	7970	12200	16300	21900	34500	47500
FWHM	660	940	850	1600	1490	2130	3070	390	4720	4600

Sloan Digital Sky Survey Photometric System

The SDSS photometric system comprises five nonoverlapping passbands that range from the ultraviolet cutoff at 3000 *Å* to the sensitivity limit of silicon CCDs at 11000 *Å*. The response functions are displayed in Figure 3.3 and in Table 3.3 are listed the average wavelengths of the SDSS filter set as defined by Fukugita et al. (1996).

Table 3.3: Effective Wavelengths and FWHM for the SDSS as specified in the ADPS Database.

Band	*u*	*g*	*r*	*i*	*z*
λ_{eff} [Å]	3557	4825	6261	7672	9097
FWHM [Å]	599	1379	1382	1535	1370

UBVRIJHKLM Colors

The UBVRIJHKLM photometric system (Bessell-Brett) is usually used for stellar population studies, so in this work we have considered, for the computation of magnitudes and colors of our galaxy models, the SSPs SED derived adopting a Salpeter and Kroupa IMFs.

As an example we plot the evolution of some colors for SSPs with a Kroupa IMF in Fig 3.4. Lines are for metallicities of 0.008, 0.019, 0.07, and 0.1 respectively. As we see, the colors

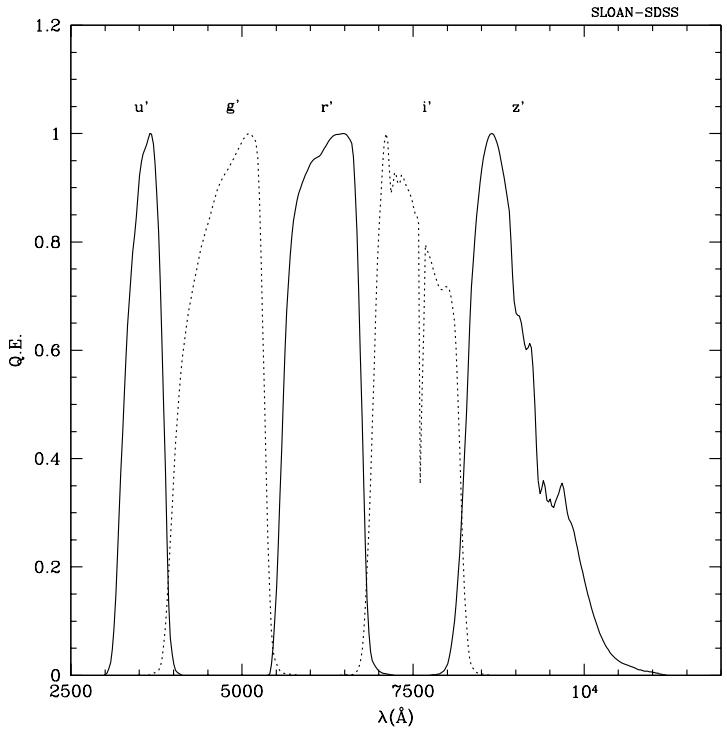

Figure 3.3: Filters for the SDSS photometric sytems. They refer to the filter throughputs as seen through airmasses of 1.3 at Apache Point Observatory. All curves are normalized to their maximum value.

.

evolve quickly when the stellar age is lower than about 2 *Gyr* and then they evolve slowly. The (B-V) color is sensitive to stellar age, while the (V-K) color is sensitive to metallicity.

As the SSP ages the color (1550-V) gets redder and redder till it turns to blue colors at critical ages that depend on the metallicity.

ugriz Colors

The Sloan Digital Sky Survey (SDSS) supplies a good deal of observational data and it uses its own *ugriz* system. In order to use its photometry data conveniently, we calculated some colors on the SDSS-*ugriz* system.

In Fig. 3.5 we show the evolution of some colors. Lines are for metallicities of .0.008, 0.019, 0.07, and 0.1 respectively. The (u-r) is an age sensitive color.

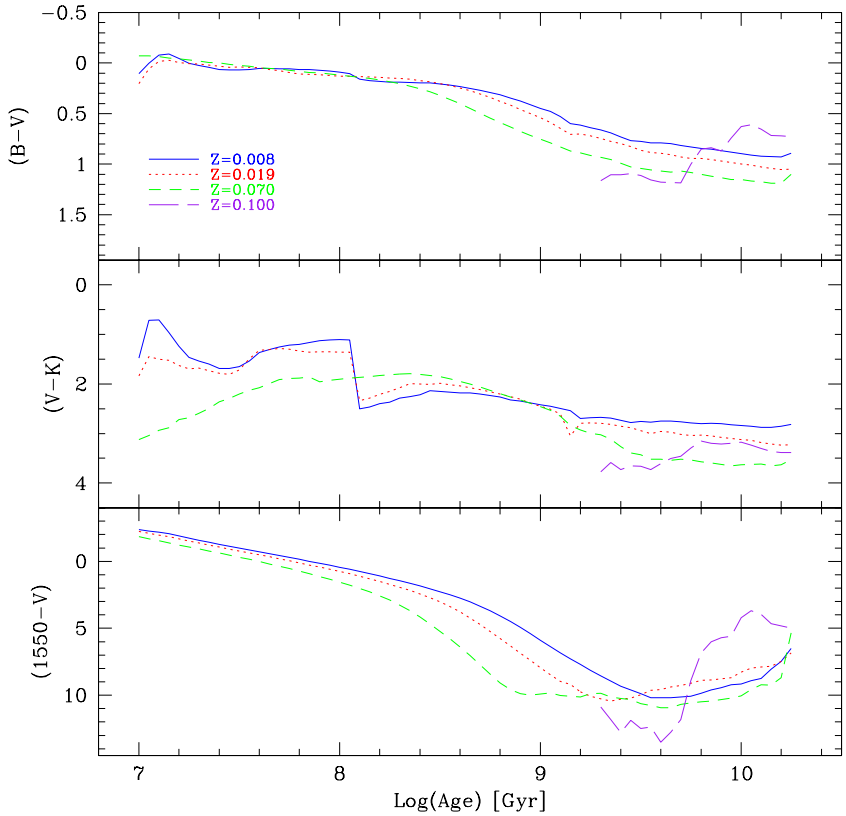

Figure 3.4: Evolution of the (B-V), (V-K) and (1550-V) colors in the Besseel-Brett photometric system for SSPs computed with a Kroupa IMF; all magnitudes are computed in the VEGAmag system.

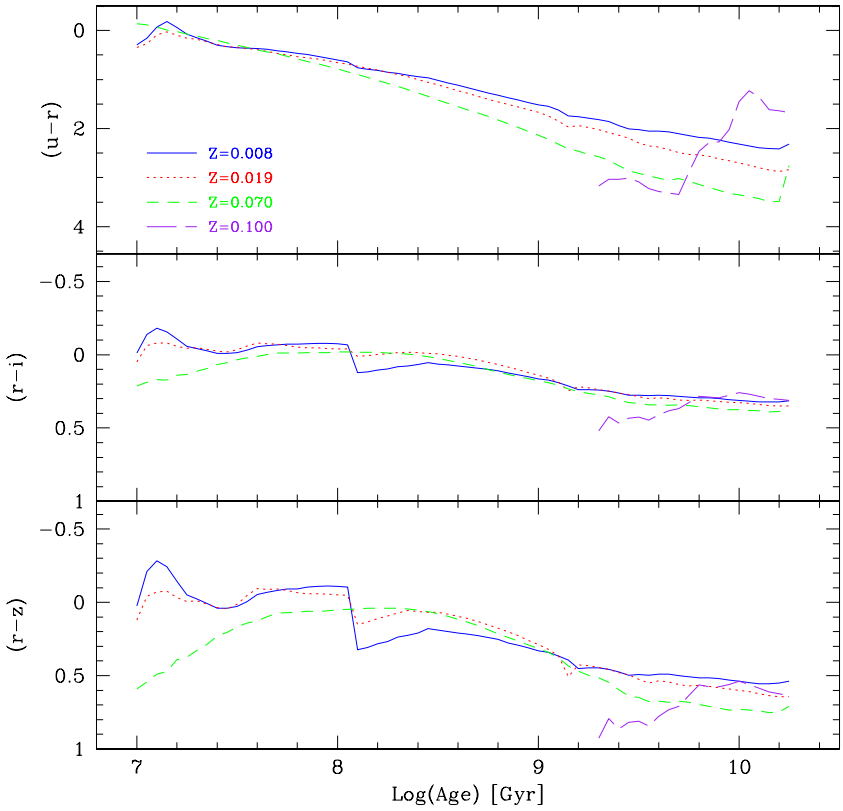

Figure 3.5: Evolution of the (u-r), (r-i) and (r-z) colors in the SDSS photometric system, for SSPs computed with a Kroupa IMF; all magnitudes are computed in the ABmag system.

Chapter 4

Spectro-Photometric Models of ETGs

Accurate models of spectro-photometric evolution of galaxies for different morphological types are needed to cast light on many key questions of galaxy formation and cosmology, and to reproduce the integrated properties of these systems. In brief, for nearby galaxies the observed integrated spectral energy distribution (SED) is used to infer the past history of star formation, while for more and more distant galaxies the observed magnitude-redshift relation, the color-redshift relation, the galaxy number counts, and the redshift distribution of galaxies are compared to the theoretical predictions from spectro-photometric models to cast light on the Hubble constant H_0 and the redshift of galaxy formation z_{for}. Over the last decade, an impressive number of chemical-photometric models for elliptical galaxies have been developed by several authors (Arimoto & Yoshii 1987; Bressan et al. 1994; Bruzual A. 1983; Bruzual A. 1992; Bruzual & Charlot 1993; Ferrini & Poggianti 1993; Guiderdoni & Rocca-Volmerange 1987; Guiderdoni & Rocca-Volmerange 1990; Guiderdoni & Rocca-Volmerange 1991; Gibson & Matteucci 1997; Renzini & Buzzoni 1986a; Rocca-Volmerange & Guiderdoni 1987; Rocca-Volmerange & Guiderdoni 1988; Rocca-Volmerange 1989; Rocca-Volmerange & Guiderdoni 1990; Tantalo et al. 1996; Tantalo et al. 1997; Tantalo et al. 1998; Tinsley 1980a; Yoshii & Takahara 1988; Kodama & Arimoto 1997; Vazdekis et al. 1996; Vazdekis et al. 1997) in which various models of evolutionary population synthesis (EPS) have been presented.

All these models adopt a chemical-evolutionary code that simulates the evolution of the galaxy as a point source, no morphological assumpion has been done. In particular the galaxy formation results from the collapse, in isolation, of a homogeneous sphere of primordial gas where star formation is taking place at the same time as the collapse proceeds, and therefore they belong to the category of dissipational collapse models. The resulting elliptical galaxies contain a composite stellar population where the metallicity ranges from zero up to several times solar.

N-body simulations are one of the best tools that permit the study of complex systems such

as galaxies and clusters of galaxies. Three-dimensional numerical simulations of early-type galaxies, including a hydrodynamic treatment of the baryonic component are useful to understand their formation and evolution, for the fact that spheroidal systems are of interest as they contain more than half of the total stellar mass in the local Universe (Fukugita et al. 1998).

In this thesis we therefore adopted cosmo-chemo-dynamical models that follow the formation of a single spheroidal galaxy, self-consistently and from CDM initial conditions, to which we apply the EPS technique with the propose of to deriving the spectro-photometric evolution of these systems.

4.1 The Cosmo-Chemo-Dynamical Evolutionary Code

We consider cosmological simulations carried on by Merlin & Chiosi (2006, Merlin & Chiosi (2007) using their cosmo-chemo-dynamical evolutionary code [GALDYN]. Their code stands on the original N-body TreeSPH formalism developed in Padova by Carraro et al. (1998).

The TreeSPH formalism combines the tree algorithm (Barnes & Hut 1986) for the computation of the gravitational forces of dark matter and stars with the SPH (Lucy 1977; Benz 1990) approach to numerical hydrodynamics of the gas component. It is fully-Lagrangian, three-dimensional, and highly adaptive in space and time owing to individual smoothing lengths and individual time-steps.

It includes self-consistently most of the important physical processes: self-gravity, hydrodynamics, radiative cooling, star formation, energy feedback, and metal enrichment. It takes into account the chemical enrichment from feedback by both SNe II and SNe Ia, and mass loss from intermediate-mass stars, and follows the evolution of the abundances of several chemical elements in both gas and interstellar components (Lia et al 2002).

The numerical recipe for star formation, feedback, and chemical enrichment along with all the other physical processes considered is described in Merlin & Chiosi (2006, Merlin & Chiosi (2007) along with the improvements to the initial conditions and the multi-phase description of the interstellar medium.

4.2 Initial conditions

The initial conditions adopted are defined as 'quasi-cosmological': starting from realistic simulations of the cosmological evolution of the Universe, these are adapted to the numerical simulations of galaxy formation and evolution.

The proto-galaxy follows the Hubble flow and evolves from an initial redshift of, z_{ini}, varying from model to model, down to the present day ($z \sim 0$). The galaxy has an intial mass and

initial radius, and is described by a number of particles that depend on the computational possibilities. The baryonic part is initially composed completely of gas and follows the Dark Matter perturbations until it is heated by mechanical friction and when radiative cooling becomes efficient the first cold clouds begin to form, and the gas component is finally turned into stars. In a star particle, SN explosions may occur, these release energy that cause evaporation of the nearby clouds which quenches the star formation.

The spheroidal galaxies evolve in a Cold Dark Matter (*CDM*) cosmological scenario: for instance the so-called Standard *CDM* (*SCDM*) in one case and the realistic Λ*CDM*, that considers the cosmological constant, with constraints following the WMAP3 (Spergel et al. 2003) is assumed for the others.

The cosmology in use has the parameters listed in Table 4.1. The initial conditions assume scale-invariant adiabatic fluctuations described by the index n. The matter density Ω_M and the cosmological constant Ω_Λ, where the mass is dominated by cold dark matter, are those of a flat, $\Omega_M + \Omega_\Lambda = 1$, universe.

The present-day expansion rate is parameterized by the Hubble parameter h[1], where h_0 is the present-day value. σ_8 is the rms mass fluctuations of the present-day Universe that normalizes the density fluctuations and fixes the initial redshift of the simulations via the amplitude of the density fluctuations within a sphere of radius 8 $h^{-1}\ Mpc$.

Table 4.1: Cosmological parameters for the different scenarios analyzed

Model	SCDM	Λ*CDM*
h_0	0.50	0.73
Ω_M	1	0.238
Ω_Λ	0	0.762
σ_8	0.5	0.74
n	1	0.951

4.2.1 Basic Physics

The gravitational forces act on all kinds of particles - dark matter, gas, stars and are described by the Tree code algorithm; the hydrodynamical processes that act only on the gas particles, the gas component is considered to be a unique fluid described by the SPH algorithm. The physical

[1] h is defined such that $H_0 = 100\ h\ km\ s^{-1} Mpc^{-1}$.

processes included are:

- gas cooling by radiative processes and inverse Compton cooling;
- star formation;
- gas heating by energy injection from SN explosions;
- chemical enrichment.

Once the formation has began, the mass evolution of the structures, the energy injection from different mechanisms, and the emitted radiation can affect the subsequent galaxy evolutionary processes. Feedback effects can either reduce or increase the efficiency of the star formation process.

All the proceses require higher computational power to have a better resolution, and need ad hoc descriptions for their treatment. We will now briefly see how all these processes are taken in consideration.

Gas cooling takes place in collapsing regions, where star particles are created from the gas that collapses. The cooling by radiative processes is included along with the inverse Compton effect that becomes important at high redshifts. Details on these processes and the cooling rates are found in Carraro et al. (1998).

Star formation is usually described by the empirical Schmidt (1959) law, following which the rate of star formation is proportional to the gas density. The fraction of gas particles turned into star particles is proportional to the density according to the law:

$$\frac{d\rho_\star}{dt} = c_\star \frac{d\rho}{t_{dyn}}, \tag{4.1}$$

where $\rho_\star$ is the stellar density and ρ the gas density, $c_\star$ the star formation efficiency, t_{dyn} the dynamical time scale. Gas particles obey this law, althogh interpreted in a probabilistic way, and are eventually transformed into star particles. To avoid this creation of new star particles Lia et al. (2002) interpreted the law as the probability that a single gas particle is completely transfomed into a star particle in the sebsequent time step.

Within numerical simulations, the most grounded idea of star formation is based on the creation of new star particles of different masses according to the chosen initial mass function (IMF). The number of particles with this assumption would be too large and due to the limited computational capability, it would be difficult to follow their evolution.

Since stars are expected to return energy to the ISM via SuperNovae (SN) explosions, and the bulk of the energy released in the ISM is known as the stellar energy feedback. Following the same approach, a star particle has assigned a probability that it will return back into the ISM.

When this takes place, the particle carries along corresponding metal production, SN rate and energy feedback. All this has the advantage of conserving the total number of particles.

Gas heating is generally due to feedback from supernovae explosions, stellar wind and UV radiation emitted by massive stars, cosmic UV light, and cosmic background radiation. The total heting rate by raditive processes is given by

$$\Gamma = \frac{E_{SNI} + E_{SNII} + E_w + E_{UV}}{\Delta t}, \tag{4.2}$$

where the terms refer to type Ia and II supernovae, stellr winds and ultraviolet flux, respectively. In the model considered, only the effects from SN feedback is taken into account, neglecting the other two. The UV flux from massive stars is absorbed by the interstellar moleculr gas and re-emitted in the far infrared and thus soon lost by radiation; the kinetic contribution by stellar wind should be traeted on much smaller scales that those permitted by the resolution of these simulations. As concerning to SN feedback, the Type Ia and II SN return to the interstellar medium gas that has been nuclearly processed.

The numerical simulations adopted in this thesis assume an *Initial mass function* (IMF) of Kroupa (1998) or Salpeter (1955), are defined in Table 4.2, for the different model galxies.

For what concerns the *chemical enrichment*, the material, processed by nuclear reactions in stellar interiors and given back to the interstellar medium by SN explosions and/or stellar winds, enriches the gas in metals. To correctly estimate the chemical enrichment, the stellar ejecta and the chemical yields per stellar generation are calculated, secondly to suitably spread the newly formed metals into the surronding gas; see Lia et al. (2002) for a complete description of the physical processes involved in the computation and of their implementation in the code. In their simulations (Merlin & Chiosi 2006; Merlin & Chiosi 2007) follow the contribution to the mass abundance of ten elements, namely Z (metals in general), He, C, O, N, Mg, Si, S, Ca, and Fe.

New Recipe with a Multi-Phase ISM. From observational data, it is clear that the interstellar medium (ISM) in galaxies is made of several different gaseous phases, of which the dominant ones are: very cold and dense molecular clouds, warm neutral gas surrounding the molecular clouds, hot ionized material, and very hot and rerefied gas expelled by supernovae explosions; not to mention other local features such as HII regions. And in all this, observations tell us that stars are created only inside the dense molecular component. So the new approach in the code developed by Merlin & Chiosi (2007) considers a multi-phase description of the IS in which star formation can occur only in the cold component.

The SPH algorithm describes properly a single-phase fluid (Marri & White 2003), but is not adequate to study a more complex mixture of different (two or more) phases in mechanical and thermodynamical equilibrium.

To study this more complicated model within the Padova NB-TSPH code of galaxy formation and evolution, Merlin & Chiosi (2007) applied the *sticky particles* algorithm of (Levinson

& Roberts 1981), in which the 'cold particles' are self-gravitating clouds that reproduce two of the listed phases lumped together, the molecular and the neutral hydrogen ones, at different temperatures and densities.

In this view, a hot gas particle, which is initially described by the SPH formalism, is transformed in a cold gas particle when its temperature falls below a defined threshold and the density becomes denser than a given value. This particle is no longer described by the SPH formalism and is free to move across the ISM without feeling drag forces, and their evolution is subject only to gravitational forces, radiative cooling, cloud-cloud collisions (mutual inelastic collisions between clouds trigger star formation) and SN feedback, thus loosing its SPH properites.

This new cold gas particle is made of two components of different temperature and density: a cold part corresponding to the molecular cloud and a hot part that represnts the surrounded warm neutral medium. In this way the warm part cools down and the mass of the cold one increases so that the relative densities change.

From this cold gas particle, a star particle is eventually formed following the Schmidt (1959) law, interpreted in the probabilistic manner as proposed by Lia et al. (2002). A stellar particle that might be subsequently transformed back into gas as a result from SN explosions, which release metals and energy to the ISM that heats up the cold gas. However, in this view, only cold particles are allowed to form stars.

The baryonic part is initially composed completely of warm gas and follows the Dark Matter perturbations, until it is heated by mechanical friction and when radiative cooling becomes efficient so that the first cold clouds begin to form, it is turned into the stellar component. In a star particle, SN explosions may occur, these release energy that cause evaporation of the nearby clouds which quenches the star formation.

Other than this, UV flux and stellar winds from massive stars is taken into account with some regard, along with energy contribution from a radial kick to gas clouds from dying star particles that explode in SN.

4.2.2 Galaxy Properties

The properties of the simulated galaxies considred in this work are summarized in Table 4.2 for the initial parameters, and in Table 4.3 for the galaxy at $z = 0$; for other parameters regarding the simulations see (Merlin & Chiosi 2006; Merlin & Chiosi 2007). We will refer to the simulations as Model *SCDM* and ΛCDM for the two different cosmologies in use; whereas the one indicated with ΛCDM_{mp} refers to the simulation that evolves following the new recipe of the multi-phase ISM, differing in initial mass and other initial parameters.

The total mass M_{tot} of the simulated galaxies within the initial sphere radius R comprises both the dark M_{DM} and baryonic matter M_b components, depending on the baryonic mass frac-

tion f_b ($f_b = \Omega_b/(\Omega_b + \Omega_{DM})$). Dark matter and baryonic particles have a mass, $M_{p,DM}$ and $M_{p,b}$ respectively, that depends on the total mass of the components (M_{DM} and M_b respectively) and the maximum total number of particles that the computational capability permits to follow. The mass of star particles resemble that of clusters as they are of the order of $\sim 10^7\ M_\odot$.

In their simulation the fixed softening lenght [2] is of the order of $\varepsilon_b = 1\ kpc$ and $\varepsilon_{DM} = 2\ kpc$, for the two components.

Table 4.2: Initial dynamical and computational parameters for the three model galaxies

Model		*SCDM*	ΛCDM	ΛCDM^a_{mp}
Initial Total Mass [$M_\odot$]	M_{tot}	1.6×10^{12}	8.8×10^{11}	2.5×10^{11}
Initial Baryonic Mass Fraction	f_b	0.1	0.176	0.176
Initial Baryonic Mass [$M_\odot$]	M_b	1.6×10^{11}	1.4×10^{11}	4.2×10^{10}
Initial Sphere Radius [kpc]	R	33.2	28	19
Initial Number of Dark Matter Particles		14000	14000	7000
Initial Number of Gas Particles		14000	14000	7000
Dark Mass for one particle [$M_\odot$]	$M_{p,DM}$	1×10^8	5.5×10^7	3×10^7
Baryonic Mass for one particle [$M_\odot$]	$M_{p,b}$	1×10^7	1×10^7	6×10^6
Initial Redshift	z_{for}	50	60	60
IMF		*Kroupa*	*Kroupa*	*Salpeter*
Softening length for Dark Matter [kpc]	ε_{DM}	2	2	2
Softening length for Baryonic Matter [kpc]	ε_b	1	1	1

[a] multi-phase simulation.

Galaxies form at redshift z_{for}, different for each model, and the evolution is followed until the present day, except for the ΛCDM simulation that stopped at redshift $z \sim 1$ due to computational problems.

In Figure 4.1 is shown the star formation history (SFH) versus time, in *Gyr*, and/or redshift, for the simulated galaxies adopted in this thesis. The stars form in clumps of cold gas that have collapsed on small scales. As is clearly shown, the galaxy forms with an initial starburst at $1-3\ Gyr$ in all cases. As the cold gas is depleted the SFR declines rapidly, and we note that

[2] The softening lenght is a term is introduced in the calculation of the gravitational forces to avoid divergence problems for distances next to zero

Table 4.3: Parameters of simulated end-product for the three model galaxies

Model		*SCDM*	ΛCDM	ΛCDM_{mp}
Final Redshift		0	0.95[a]	0
Age of the last model [*Gyr*]	T_{gal}	13	7	13
Final Number of Star Particles		8000	9000	5200
Final Star Mass [$M_\odot$]	$M^f_{star,tot}$	9.086×10^{10}	8.969×10^{10}	3.094×10^{10}
Final Gas Mass [$M_\odot$]	$M^f_{gas,tot}$	7.157×10^{10}	5.162×10^{10}	1.070×10^{10}

[a] The simulation stopped at $z \sim 1$ due to computational problems.

star formation has not completely stopped at present. At lower redshifts small amounts of the previously heated gas have cooled at the center of the galaxy, so the SFR continues even if at lower rates. At $z = 0$ the galaxy shows central star formation at a low level in all cases. See Chapter 7 for a more detailed analysis on this subject.

Quantitatively, in Fig. 4.2 is summarized the mass assembly process, where the mass evolution of the stellar component of the simulated galaxy is shown.

The final stellar mass of the galaxy is essentially fixed at $z \sim 2$, since little gaseous material is added to the galaxy afterwards stars age passively for the remaining time of the evolution. The galaxy thus has assembled completely, and its morphology at $z \sim 0$ is consistent with that of elliptical galaxies. Due to the early starburst, the galaxy is already old and very massive at a redshift of $z \sim 1-2$ for the different models.

Morphologically, the evolution turns the galaxy into a spheroid that quickly relaxes into the final configuration, which is the subject of the study we report here (see Figures 4.3, 4.5 and 4.8).

In Figres 4.3 and 4.5 is shown the spatial distribution of the stellar component of the simulated EG within a cube of 300 (physical) *kpc* box centered on the baricenter at different times and projected so that the galaxy is seen on the xy-plane. As the stars are nearly spherically distributed and show a weak asymmetry, the models are considered as spherically symmetric and the projection on any of the planes can be considerd for the analysis. The Figure summarises the global morphological properties of the stellar populations for the ETGs formed in the model galaxies until the age of $T = 13$ *Gyr*: the stars appear to have the morphology of an elliptical galaxy.

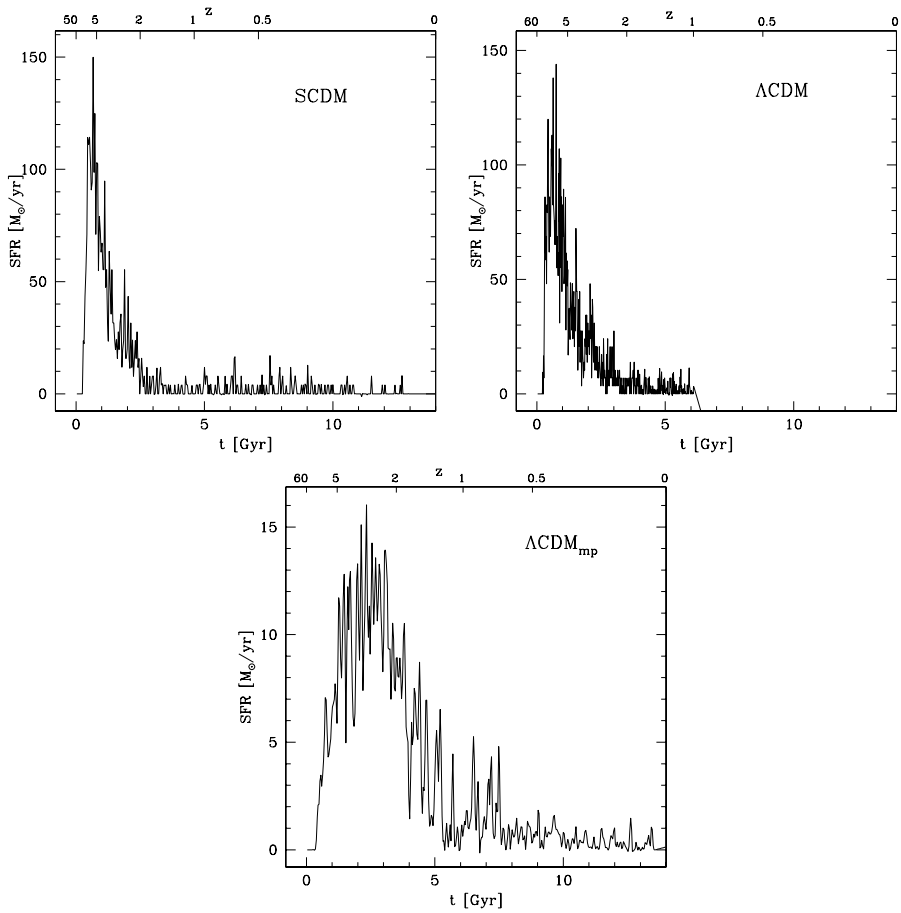

Figure 4.1: Star formation rate, in units of $M_\odot/yr$, versus age, in *Gyr*, and/or redshift for the different model galaxies considered. The star formation begins at $z \sim 50$ for the *SCDM* model (upper left), $z \sim 60$ for the Λ*CDM* model (upper right), $z \sim 60$ for the ΛCDM_{mp} model (lower).

4.3 Simulated Galaxy Spectrum

The synthetic stellar spectrum of a galaxy is a well-established theoretical tool for investigating the properties of the integrated light from distant galaxies where individual stars cannot be resolved.

One of the major approaches that have been used to compute the integrated light of a stellar population is the EPS technique, which uses a continuous distribution of stellar masses, and hence tracks, to compute the locus in luminosity and effective temperature at a given time for any mass, as we have desribed in Chapter 3. This enables us to generate a multiwavelength SED for the target galaxy, when combining the output of the cosmo-chemo-dynamical simulation

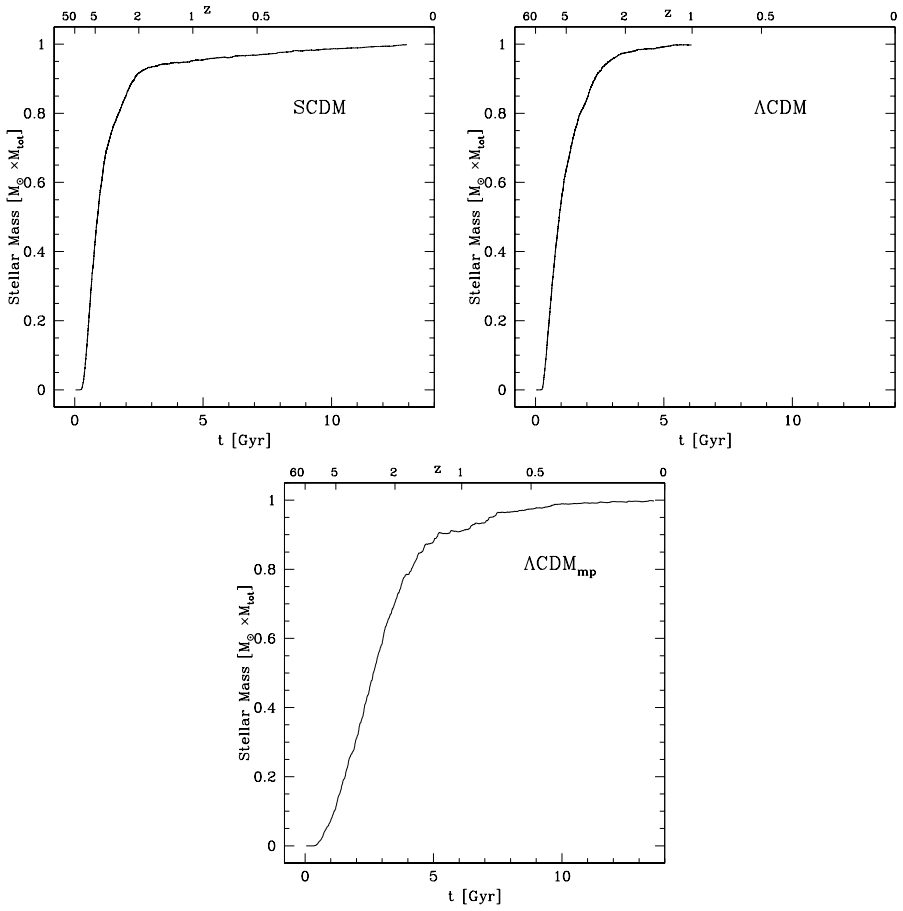

Figure 4.2: Mass assembly, in units of $M_\odot \times M_{tot}$, where M_{tot} is the total baryionic mass of the galaxy at each time, versus age, in *Gyr*, and/or redshift for the different models considred, as labeled.

with the evolutionary population synthesis code.

At any time one can compute the integrated spectrum by summing up the individual spectra of the stars in the population at that instant. The spectro-photometric modeling requires the knowledge of the metallicity of the stellar populations as function of time. The simulation code tracks the metal content of each gaseous and star particles: each carry their own age and metallicity 'tag', due to the self-consistent calculation of the cosmo-chemo-dynamical evolution.

This enables us to generate a multiwavelength integrated SED for a simulated galaxy with any star formation history that can be described by a superposition of SSP models of different ages and metallicities.

Owing to the mass resolution, due to the limited number of particles in the simulations, each

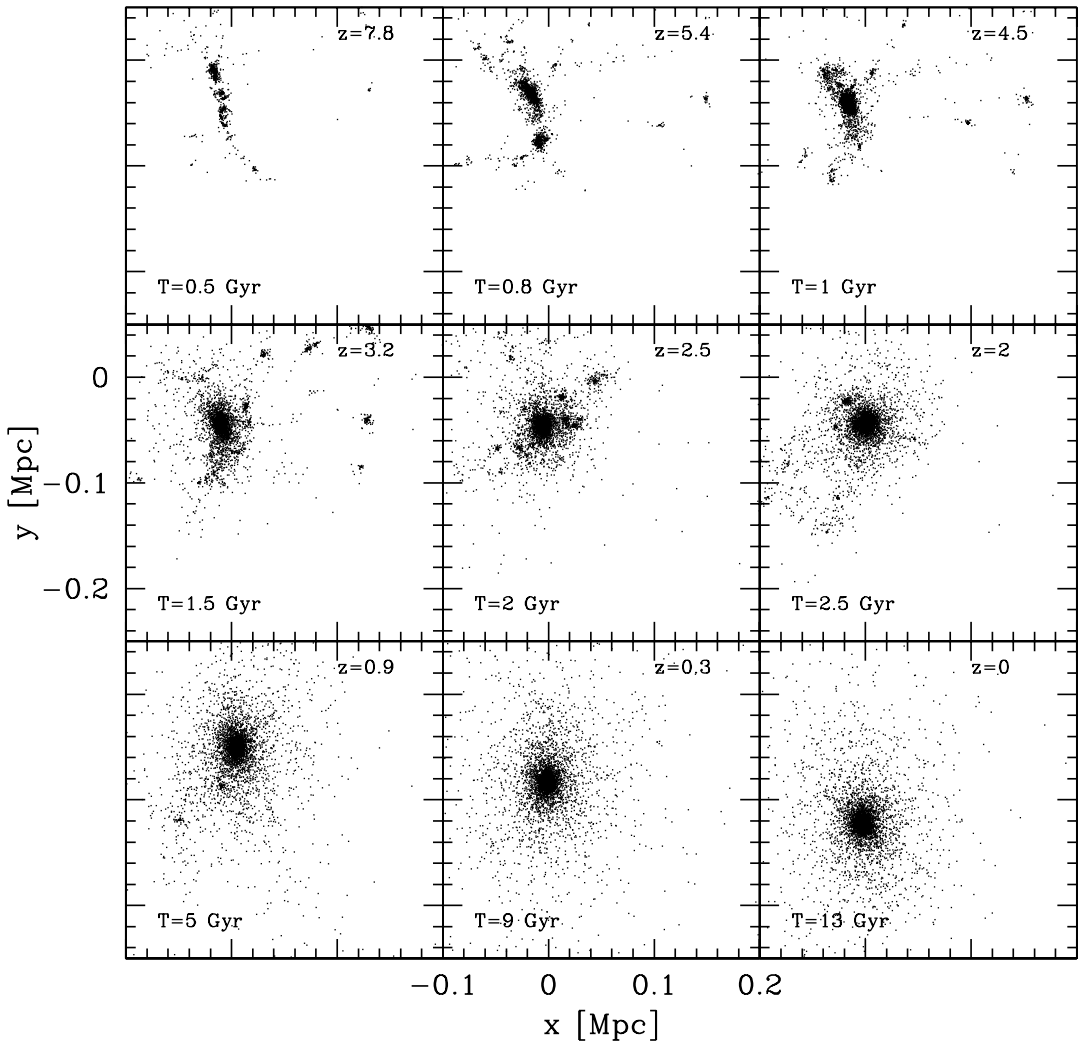

Figure 4.3: Star particle distribution for the *SCDM* model galaxy and its evolution within a region of 300 physical *kpc* on a side projected onto the xy-plane of the three-dimensional simulation, shown at different ages and/or redshifts as labeled.

star particle has the mass size of a cluster ($\sim 10^7\ M_\odot$), in which the real stars distribute according to a given initial mass function and are born in a short but intense burst of star formation, so they are homogeneous in age and also in chemical composition. In this way, each star particle can be approximated to a single stellar population (SSP) in which the stars are distributed in mass

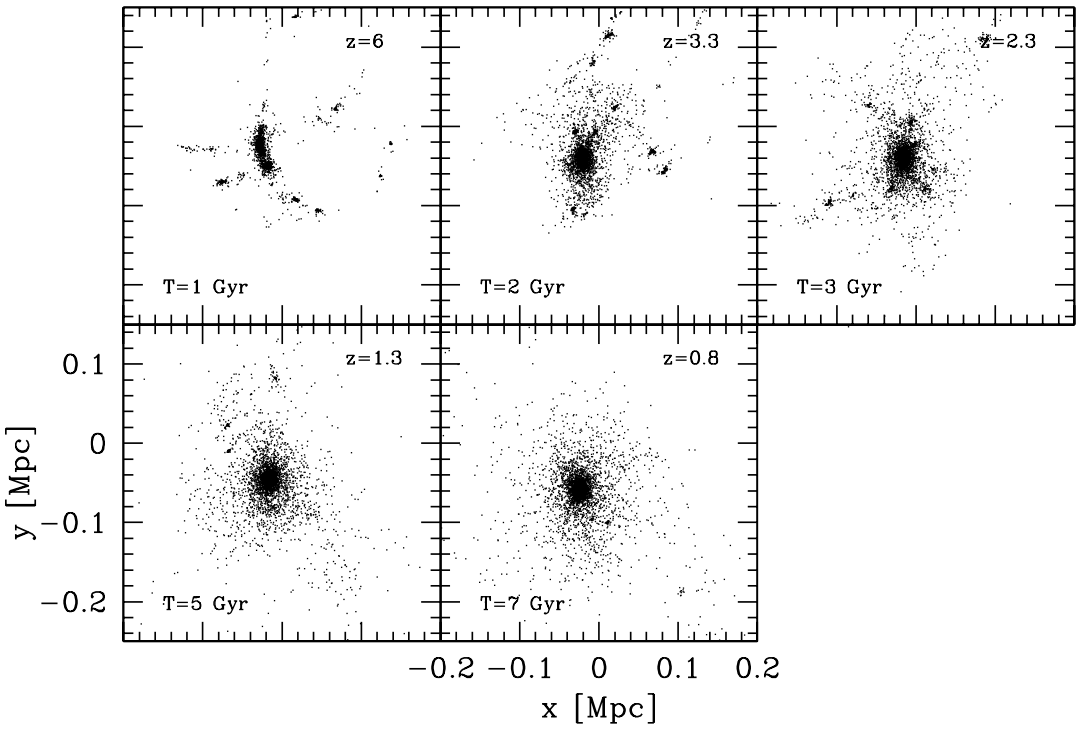

Figure 4.4: Star particle distribution for the Λ*CDM* model galaxy and its evolution within a region of 400×400 physical *kpc* on a side projected onto the xy-plane of the three-dimensional simulation, shown at different ages and/or redshifts as labeled.

following the IMF.

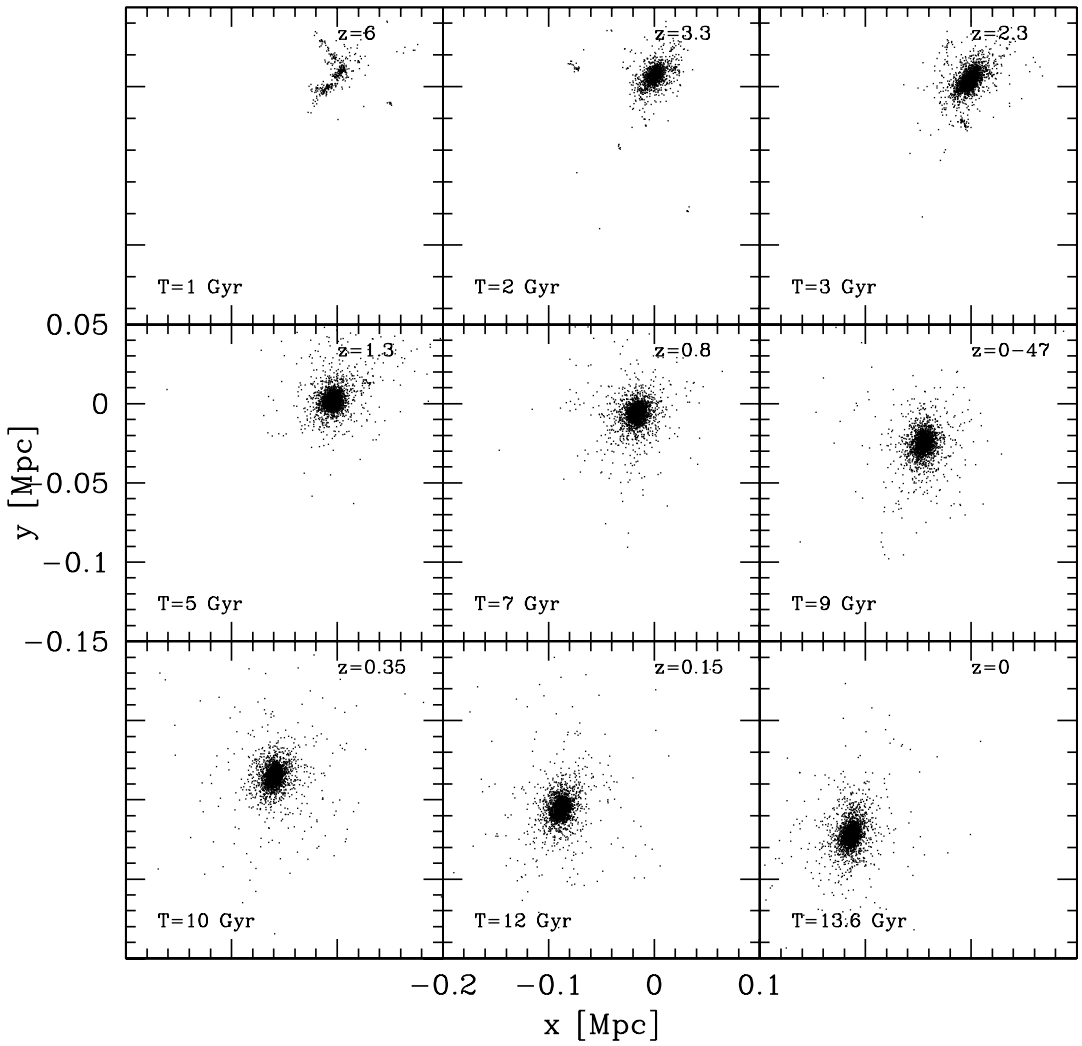

Figure 4.5: Star particle distribution for the ΛCDM_{mp} model galaxy (multi-phase) and their evolution within a region of 300×200 physical *kpc* on a side onto the xy-plane of the three-dimensional simulation, shown at different ages and/or redshifts as labeled.

4.3.1 Integrated Spectral Properties

As the stellar mass of the single particles of the simulation resembles that of a globular cluster, i.e. coeval and chemically homogeneous, here, the SED of each star particle is assumed to be that of an SSP. In this way, the integrated SED of the galaxy is computed by simply summing

the SEDs associated to the single star particle, taking into account their time of creation and the metallicity.
Thus the monochromatic flux of a galaxy with age T, $F_\lambda(T)$, is described as

$$F_\lambda(T) = \sum F_{SSP}(\lambda, Z_i, \tau_i) \times M_{p,bar}, \tag{4.3}$$

where $F_{SSP}(\lambda, Z_i, \tau_i)$ is the monochromatic flux of a SSP of age τ_i and metallicity Z_i (where the suffix *i* identifies each stellar particle), as described in 3.4, and $M_{p,b}$ the mass of each stellar particle. The age of each SSP, τ_i, is defined as $\tau_i = T - t_i$, where t_i is the time when a gas particle is converted into a stellar one and Z_i the metallicity of each stellar particle.

The flux of the SSP, $F_{SSP}(\lambda, Z_i, \tau_i)$, is obtained by interpolating in metallicity and age between the SEDs of the SSPs taken from the GALADRIEL database by Tantalo (2005)), and the summation ($\sum$) in equation 4.3 is done for all stellar particles in the model galaxy.

We have at our disposal a large number of SSP, with ages between 10^7 *yr* and 18×10^9 *yr*, and metallicities with values from $Z = 0.0001$ to 0.1, as described in § 3.1.1.

The SSPs used in this thesis were obtained assuming a Kroupa (1998) or Salpeter (1955) IMF, which are defined in Appendix A, following the IMF adopted in the numerical simulations (see Table 4.2 for details). The metallicity range considered reaches the 0.07 as higher value, excluding the 0.1 as this last SSPs are available only for ages greater than 2 *Gyr*. This choice is justified as the mean metallicity reached by the simulation is lower than solar (see Figure 4.6).

We have computed the spectrum of the simulated galaxy for the models in the *SCDM* and Λ*CDM* cosmological scenarios as described in § 4.1.

In Figure 4.7 are shown the integrated spectral energy distribution (SED) of the simulated galaxies in the rest-frame, and for different ages.

4.4 Magnitudes and Colors of the Simulated Galaxy

Due to our self-consistent treatments of chemo-dynamics, we derived, the multiwavelength properties of the simulation, which reflect the properties of stellar components, such as age and metallicity.

Once assigned a SED to each stellar particle of the simulated galaxy, we are able to derive the integrated properties of each star by convolving their single spectrum with the transmission curves of a given photometric system, and in this way derive the magnitudes of the single star particles and hence the color evolution for two of the available photometric systems, for instance, the Bessell-Brett and the SDSS.

In Figure 4.8, for instance, is shown the color evolution in the three-dimensional space of the *SCDM* model galaxy for the Bessell-Brett system. During the evolution, the galaxy

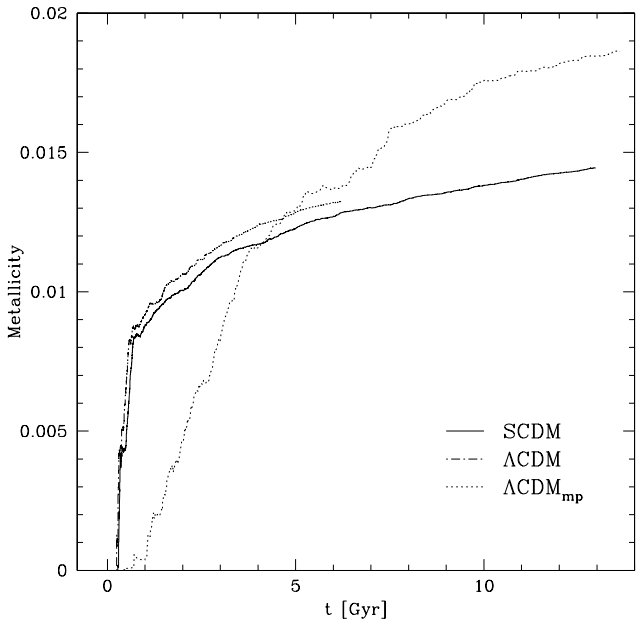

Figure 4.6: Metallicity evolution for the stellar component for all models, as labeled.

that is forming starting from an initial protogalaxy ends up to a final stage where the structure resembles that of a spheroidal system. As the galaxy is forming we can see how at initial times the star particles that collapse for first have blue colors, and as it ages the galaxy's components vary its color passing to redder colors.

In the same way the integrated spectrum of the galaxy is fed to the code to compute the evolution of the integrated magnitudes and colors.

Thorough calibration under photometric conditions is needed to convert the instrumental color profiles into meaningful calibrated colors. The approach used in deriving magnitudes and colors is described in Chapter 3.

The evolution in the rest-frame for magnitudes in the VEGA magnitude system in the Bessell-Brett photometric system is shown in Figure 4.9 and for the AB magnitude system for in the SDSS photometric system is shown in Figure 4.10, for the Model Galaxy *SCDM*. Trends are similar for all the other models.

Magnitudes computed for the model galaxies reflect the star formation history, which gives us an idea of the age distribution of stars at different times in a present-day galaxy. As we have seen in Figure 4.1, the bulk of stars is created in an initial burst at low ages that reaches a peak at $1-2$ *Gyr*, depending on the model, declining rapidly afterwards as the gas is exhausted in

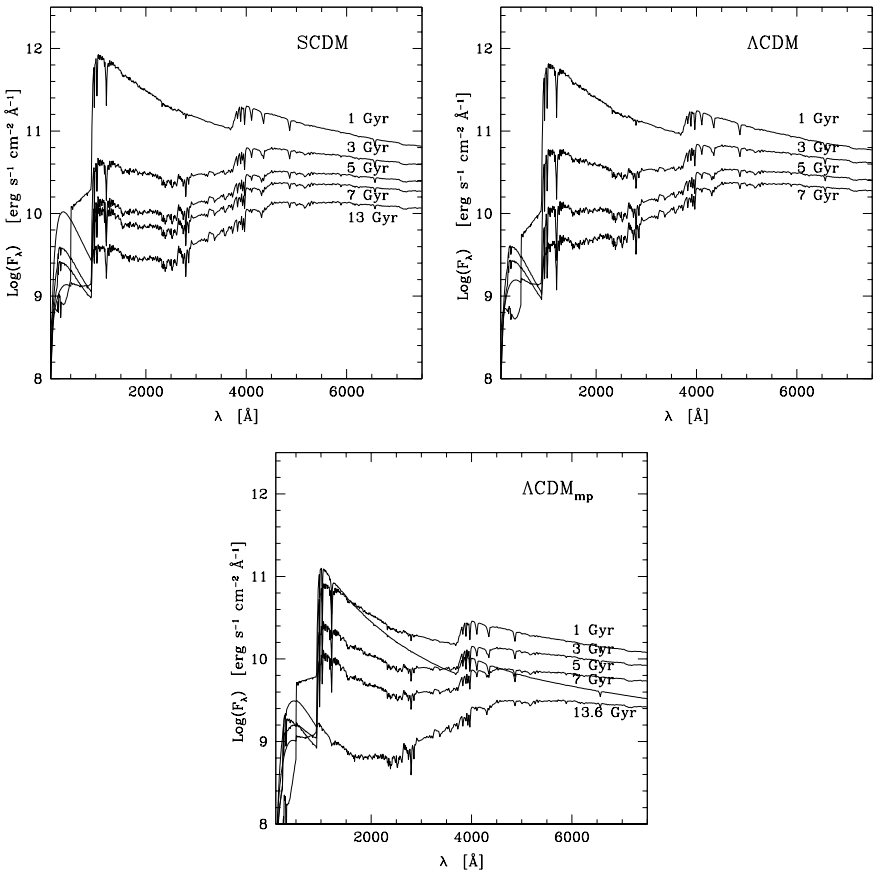

Figure 4.7: The integrated SED of the simulated model galaxies for the different cosmological scenarios, shown at different ages as indicated, for the three models (*SCDM* upper left, Λ*CDM* upper right, ΛCDM_{mp} lower panel). All curves refer to the rest-frame fluxes and ages are in units of 10^9 *yr* (*Gyr*).

the galaxy.

This physical process explains the trend seen in the magnitude evolution, in the sense that the magnitudes increase, that is the galaxy becomes more luminous and reach a maximum as the SFR has its initial burst and reaches the peak. Afterwards, the magnitudes decrease to lower values following the SFR that declines rapidly.

In particular for the Bessell-Brett system (Fig. 4.9), the magnitude at 1550, that tests the ultra-violet region of the spectrum, as all broadband magnitudes at wavelengths lower than 2000 *Å*, weights the star formation at each epoch and reproduces the trend seen in the SFR. The same effect but in lower measure is visible for the SDSS system (Fifg. 4.10 for the u' and g' bands

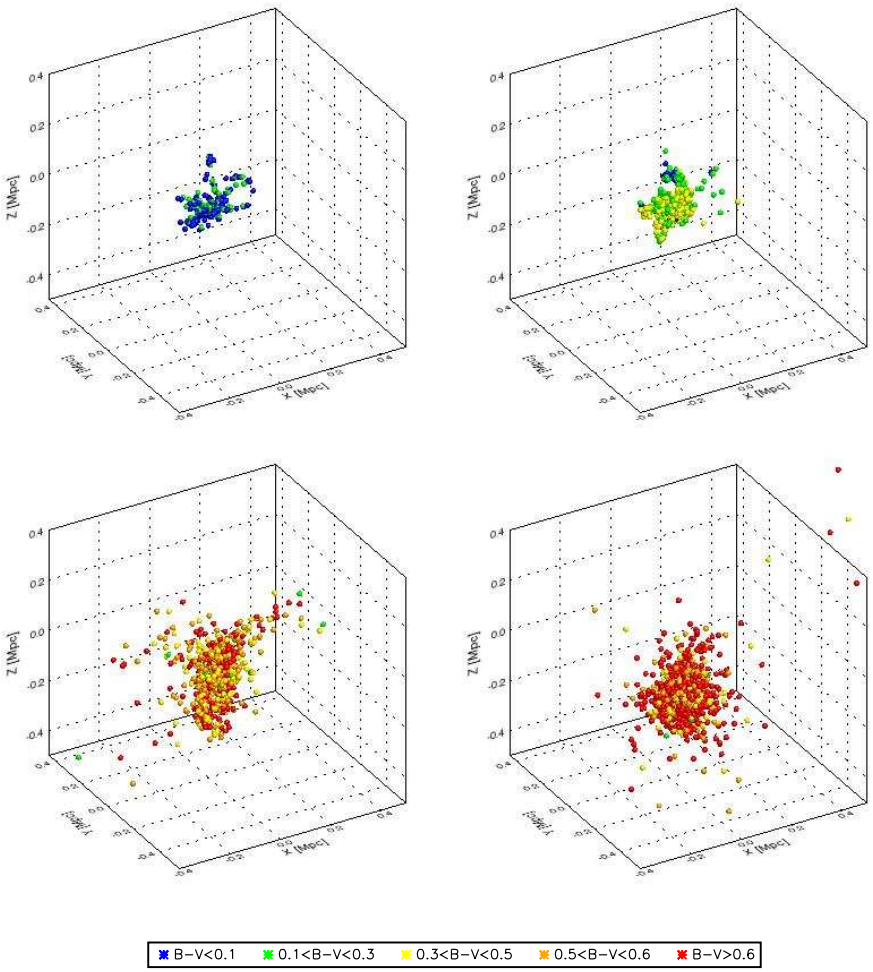

Figure 4.8: Three-dimensional view of the SCDM simulation for four epochs (1 *Gyr* upper left panel, 2 *Gyr* upper right, 5.5 *Gyr* lower left, and 13 *Gyr* lower right) of the rest-frame $B-V$ color evolution for particles within the *SCDM* model galaxy.

where the color evolution is less smooth than for the other three bands.

Color evolution for the model galaxies is shown in Figures 4.11 and 4.12. As the galaxy ages colors become redder and the differences between models are imputed to the fact that the star formation history is different for the different models.

The Λ*CDM* model has been simulated with the classical SPH formalism and has a SFR very similar to the *SCDM* one: they have similar star formation qualitatively and quantitatively, and their color evolution is also very similar.

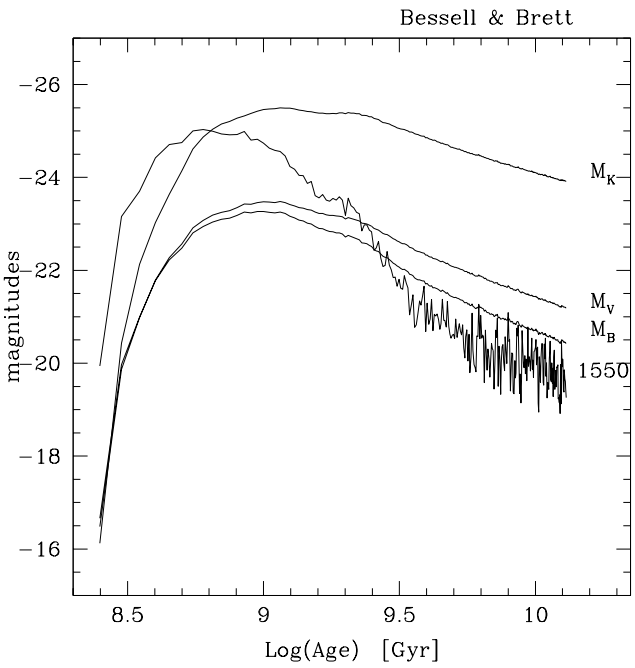

Figure 4.9: Magnitude rest-frame evolution for the Bessell & Brett photometric system applied to the *SCDM* model galaxy: M_U, M_R, M_K, and M_{1550} magnitudes are shown for reference.

The ΛCDM_{mp} was run using the new recipe with a multi-phase description: Merlin & Chiosi (2007) have shown that, due to the new prescription for star formation, the histories of formation are slightly different compared to the classical SPH treatement of the ISM. What results is that with the new prescription, the formation of the stellar mass is more gradual and lasts longer, the peak of activity is lowered and shifted to higher ages. The total mass assembled by the models is almost equal and the different behavior obtained with the two star formation prescriptions can be understood in terms of different time scale involved in the formation of new stars and is describe in detail in the reference cited above.

4.4.1 Distribution of the Stellar Populations in a Color-Magnitude Diagram

The following approach is proposed to transform the various observed colors into a likelihood distribution in age-metallicity space by using predictions of stellar population synthesis models as shown in the following diagrams.

The ‘color-magnitude’ diagrams shown in Figures 4.13 and 4.14, have been constructed for the star particles of the simulations and their associated colors derived with the photometric code. This has to be meant as a ‘check’ on the ranges of ages and metallicities that the particles

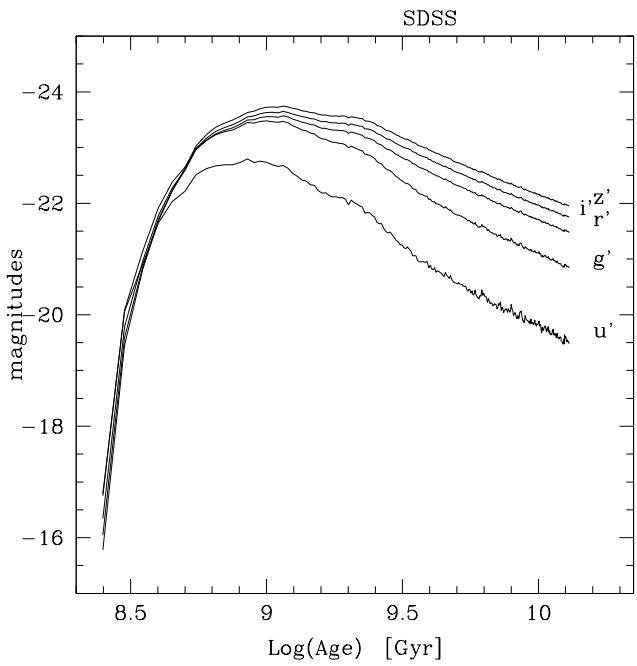

Figure 4.10: Magnitude rest-frame evolution for the SDSS photometric system applied to the *SCDM* model galaxy: magnitudes for all bands are shown.

cover. Star particles have masses that resemble those of clusters, as already specified, due to the mass resolution of the computational algorithm. This diagrams give us a coarse idea of how the particles distribuite in function of their colors, which in turn depend on their age and metallicity.

In the $V-K$ vs V diagram (Figure 4.13) we can see how particles distribute with varying metallicity: for the galaxy of 13 *Gyr* the star particles are for the most old. Star distribute along the line of older age and cover all values of metallicity. This means that the $V-K$ color tests the metallicities differences, more than the age.

The $1550-V$ vs V diagram on the other hand, tests the age differences. Stars distribute along the time line and we can see how they cover all ages lie next to the higher metallicity line.

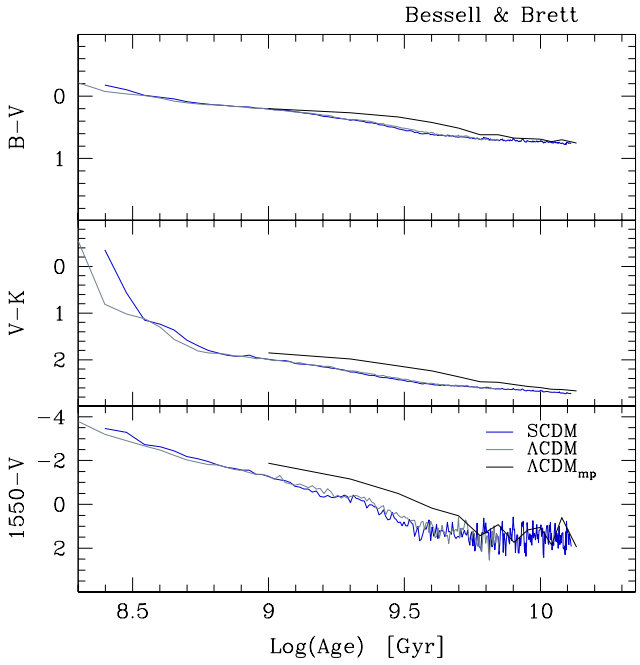

Figure 4.11: Rest-frame color evolution for the Bessell-Brett photometric system applied to all model galaxies as labeled: $B-V$, $V-K$, and $1550-V$ are shown for reference.

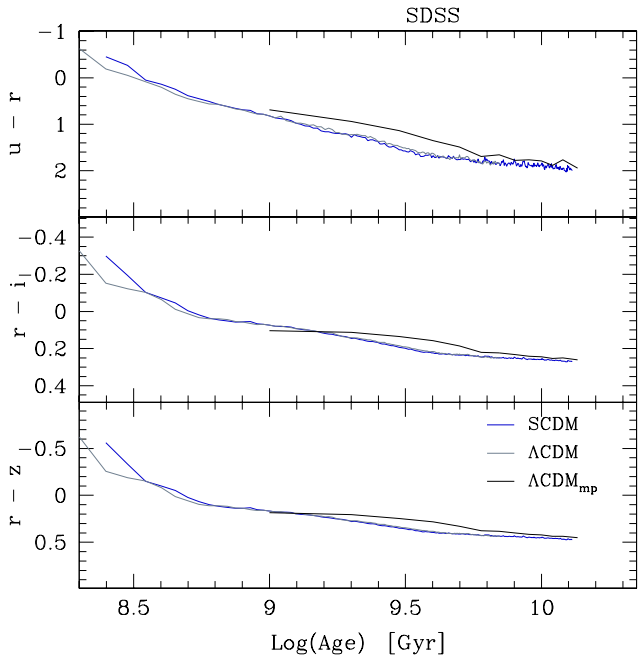

Figure 4.12: Rest-frame color evolution for the SDSS photometric system applied to all model galaxies as labeled: $u-r$, $r-i$, and $r-z$ are shown.

.

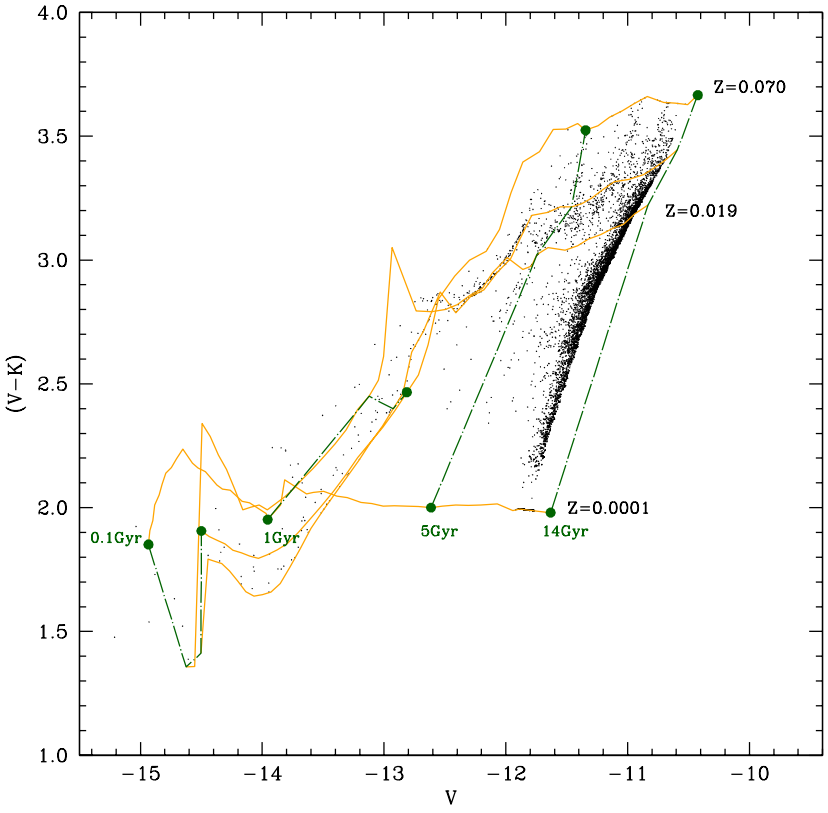

Figure 4.13: The distribution of the stellar populations in the $(V-K)-M_V$ plane for the *SCDM* model at the age of $T = 13$ *Gyr*. T he SSPs color grid is overlapped for interpretation of ages and metallicities.

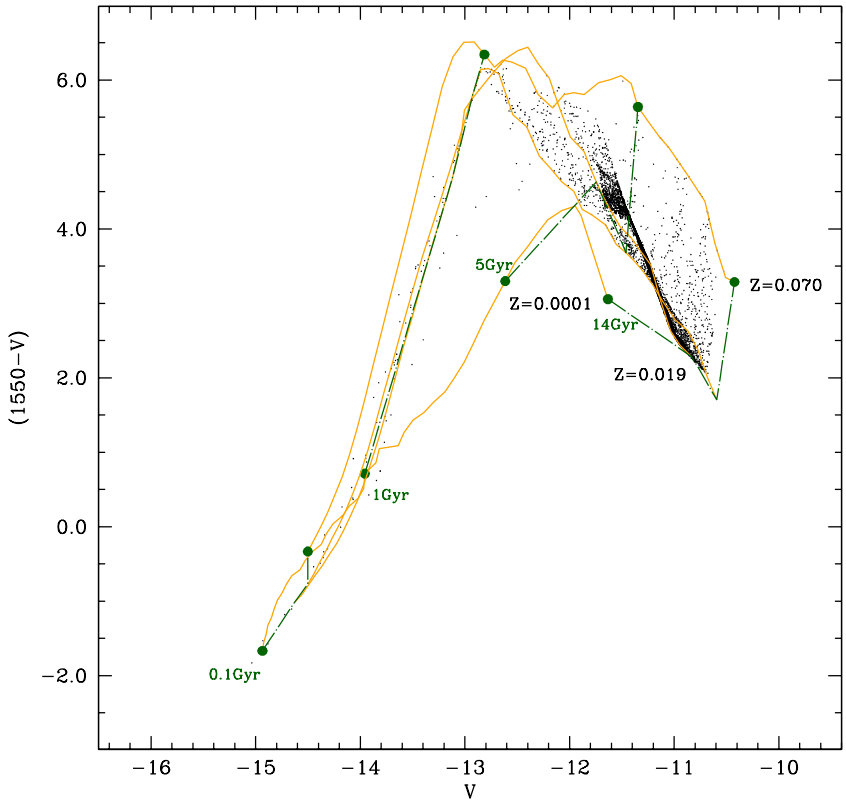

Figure 4.14: The distribution of the stellar populations in the $(1550-V)-M_V$ plane for the *SCDM* model at the $T = 13$ *Gyr*. The SSPs color grid is overlapped for interpretation of ages and metallicities.

Chapter 5

Cosmological Spectro-Photometric Evolution

The expansion of the Universe presents the challenge that sources observed at different redshifts are sampled, by any particular instrument, at different rest-frame wavelengths and, since they are compared with each other, we need to introduce the so-called '*K*-correction'. This correction term enters in the relation between the emitted-frame or rest-frame absolute magnitude of a source in one broad photometric bandpass and the observed-frame apparent magnitude of the same source in another broad bandpass.

Starting from the evolutionary synthesis results, which are not intended only for the use in the interpretation of star cluster data but also for the combination with any kind of dynamical galaxy formation and/or evolution model, we compute the evolutionary and cosmological corrections, along with the magnitudes and colors at different redshifts for the simulated galaxies described in Chapter 4.

The advent of the modern giant telescopes has opened a new era in observational cosmology and galaxy evolution can be traced back to its early stages. In this sense, deep multicolor imaging surveys are established as a powerful tool to access the population of faint galaxies with relatively high efficiency. These surveys sample the whole spectral range from the UV to the near-IR bands, enabling galaxy evolution to be followed on a wider range of redshifts. We have chosen in particular the COSMOS and the GOODS database, which allow us to select a sample of galaxies that are catalogued as early-type, in order to make a qualitative and quantitative comparison between the theoretical results obtained from our model galaxies and the observational data.

5.1 Evolutionary and Cosmological Corrections

When we consider a source observed at redshift z, we need to consider that the photon is observed at a wavelength λ_0, but it was emitted by the source at wavelength λ_e, and these two are related by

$$\lambda_e = \lambda_0/(1+z). \tag{5.1}$$

A source that has apparent magnitude m, observed through a photometric bandpass, is related to its absolute magnitude M, in the emitted-frame bandpass and to the K-correction, K_{corr}, in the following way:

$$m = M + DM + K_{corr}, \tag{5.2}$$

where DM is the distance modulus, defined by

$$DM = 5log_{10}\left(\frac{D_L(z)}{10pc}\right), \tag{5.3}$$

being $D_L(z)$ the luminosity distance and $1pc = 3.086 \times 10^{18} cm$.

If the source is at redshift z, then its luminosity is related to its spectral density flux (energy per unit time per unit area per unit wavelength) by

$$L(\lambda_e) = 4\pi(1+z)D_L^2 f(\lambda_0), \tag{5.4}$$

where $f(\lambda_0)$ is the monohromatic flux of a galaxy that has been computed as defined in Eq. 4.3.

Equation 5.2 holds if the K-correction is

$$K_{corr} = 2.5log_{10}(1+z) + 2.5log_{10}\left[\frac{L(\lambda_0)}{L(\lambda_e)}\right]. \tag{5.5}$$

In order to take a fair comparison between the samples at different redshifts, we must correct the photometric properties of our observed galaxies (magnitudes, colors, etc.) into rest-frame quantities by applying K-corrections. In addition we can also correct these rest-frame quantities for the expected evolutionary changes over the redshift range studied. These evolutionary corrections are usually performed assuming a model for the galaxy spectral energy distribution (SED) and its evolution with redshift: K- and E-corrections are generated by applying the stellar evolutionary populations synthesis technique. In this way we can recover the evolution of the absolute magnitudes and colors as a function of redshift z, including the effect of the K- and E-corrections on the integrated SED of our model galaxies.

For galaxies, the cosmological $K(z)$ and evolutionary $E(z)$ corrections are conventionally given in terms of magnitude differences:

$$K(z) = M(z,t_0) - M(0,t_0), \tag{5.6}$$

$$E(z) = M(z,t_z) - M(z,t_0), \tag{5.7}$$

where $M(0,t_0)$ is the absolute magnitude in a passband derived from the rest frame spectrum of the galaxy at the current time, $M(z,t_0)$ is the absolute magnitude derived from the spectrum of the galaxy at the current time but redshifted at z, and $M(z,t_z)$ is the absolute magnitude obtained from the spectrum of the galaxy at time t_z and redshifted at z.

The absolute magnitude, $M(z)$, in some broadband filter and at redshift z, is given by:

$$M(z) = -2.5 \log L(z,t(z)), \tag{5.8}$$

and, passing to apparent magnitudes,

$$m(z) = M(z) + E(z) + K(z) + DM(z). \tag{5.9}$$

Obviously, the relation between the cosmic time t and redshift z, $t(z)$, of a stellar population formed at a given initial redshift z_f, depends on the cosmology considered and the parameters adopted. The models presented here evolve in different cosmological scenarios, (cosmological parameters for the *SCDM* and Λ*CDM* models are listed in Table 4.1), and this has to be taken into account.

In Figure 5.1 is shown the redshifted spectrum for some values of z and for the model galaxies at our disposal. Redshifted spectra show a flow at lower wavelengths and the value at which this happens is higher with increasing redshift. This effect is due, on one part, to the fact that theoretical spectra have a lower limit of 912 $\AA$ in the rest-frame and the extension to $\lambda < 912$ $\AA$, the region covering the higher temperatures, has been made by simply assuming black-body spectra. This lower limit increases with redshift as the wavelenght is redhifted.

On the other hand, the integrated SED of model galaxies is calculated including the effect of the extinction of the stellar luminosity caused by the presence of a certain amount of metal-rich gas. The extinction is evaluated according to the relations given by Guiderdoni & Rocca-Volmerange (1987). For the effective optical thickness, τ_λ, of the gaseous component at the wavelength λ, considering the albedo, ω_λ, of the grains (Draine & Lee 1984) and the dependence of the extinction law A_λ/A_V on the metallicity $Z(t)$, Guiderdoni & Rocca-Volmerange (1987) find:

$$\tau_\lambda = 3.25(1-\omega_\lambda)^{0.5}(A_\lambda/A_V)_\odot [Z(t)/Z_\odot]^{1.35} G(t), \tag{5.10}$$

where $G(t)$ is the gas fraction and a mean value of $\omega_\lambda = 0.4$ has been taken for the albedo (Draine & Lee 1984). For the extinction law A_λ/A_V, the relation by Cardelli et al. (1989) has been adopted. From Figure 5.2 we can see how the extinction law grows exponentiallly thus increasing the absorption for decreasing wavelengths. The monochromatic flux of the galaxy with the inclusion of the effect due to extinction, $F_{\lambda,ext}$, can be expressed in function of the

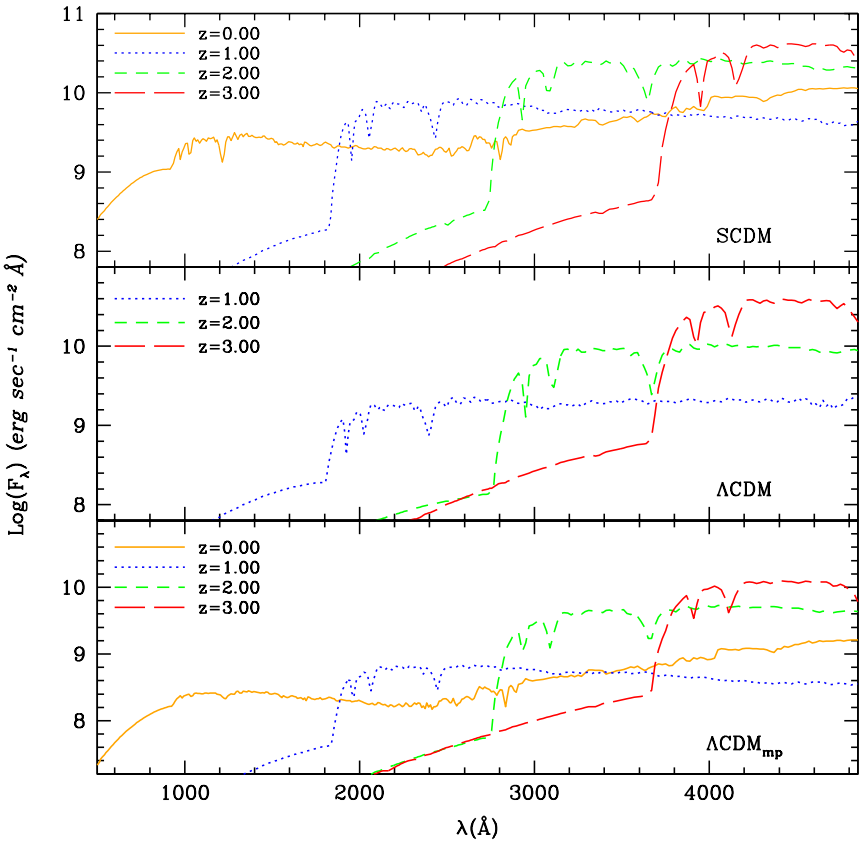

Figure 5.1: Redshifted spectra at different redshifts for the three simulated models. Internal extinction has been taken into account.

monochromatic flux of the rest-frame integrated SED of the model galaxy F_λ (see eq. 4.3):

$$F_{\lambda,ext} = F_\lambda \frac{1-\exp(-\tau_\lambda \sec i)}{\tau_\lambda \sec i}, \tag{5.11}$$

where the right-hand part of the expression is the transmission function for an angle of inclination i; a value of $i = 45$ is adopted in this context. The effect of extinction is included for wavelengths lower than 1200 $\AA$ and this internal extinction may significantly redden the colors, the effect being particularly important on the color-redshift relation.

Figure 5.3 gives us an idea of the reliability of the passband for different redshifts. As redshift increases, colors computed in bands in correspondence of the shaded area have an intrinsic uncertainty due to the two factors above mentioned. The effects together affect the redshifted spectra, as can be seen in Figure 5.1, where the flow at low wavelengths is seen at higher val-

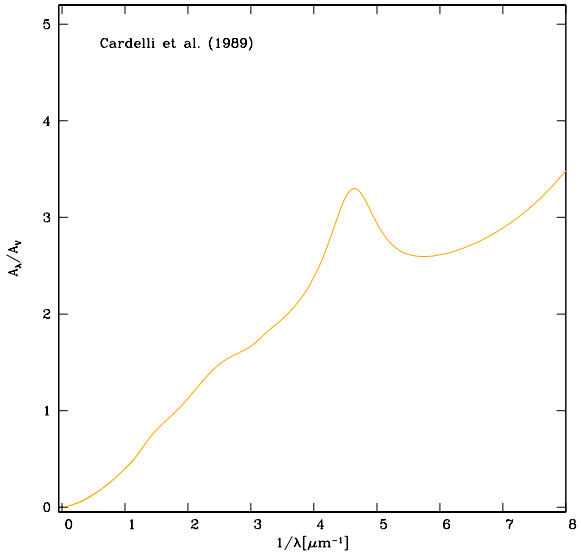

Figure 5.2: Extinction curve from Cardelli et al. (1989).

ues of λ as the redshift increases. This trend has to be taken into account in the computation of the colors the various photometric systems, in the sense that the reliability of the computed magnitudes depend on the chosen band as the redshift varies. From this consideration emerges that the reliability of the magnitudes computed, and hence the colors, depends on the redshift: for instance at a redshift of $z = 3$[1] magnitudes are considred accurate at values of wavelengths $\lambda > 4100$ *Å*.

5.2 Comparison with Data

The advent of large-scale space and ground-based surveys in a wide variety of wavelengths is giving us unprecedented acces to statistically large populations of redshifts and environments; however, the size of the galaxy samples poses a challenge when morphological classification is necessary.

At $z > 5$, traditional optical bands, e.g. U,B,V,R, fall below the rest-frame wavelength that corresponds to the Lyman-break spectral feature (1216 *Å*), where most of the stellar radiation is estinguished by interstellar or intergalactic hydrogen. Because of this, galaxies at $z > 5$ are practically invisible at those photometric bands, and even if they were detected, their colors

[1] Observational data from the surveys considered reach values of about of $z \sim 3$.

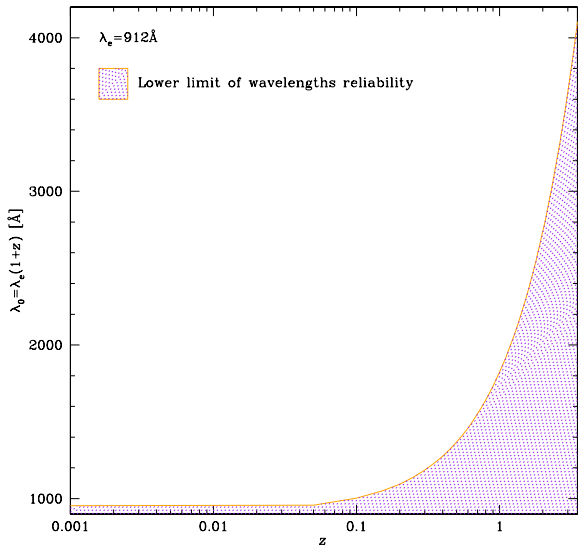

Figure 5.3: Reliability of the wavelength lower limit for the $\lambda = 912$ $\AA$ variation as a function of redshift.

would provide very little information about their stellar population.

A main characteristic of deep photometric surveys is the rich presence of galaxies, a significant fraction of which appear as point sources and cannot be easily distinguished from real stars or cannot permit a distinction between different morphologies. Thus, the object classification by means of morphological and photometric criteria is of central importance in these fields. In this Section, we will deal with two deep catalogues, which, as far as possible permit us to select early-type galaxies.

The color selection technique (the Lyman-Break Galaxy LBG by Steidel et al (1996, 1999, 2003)) has been used in some surveys to identify galaxies at high redshift, dramatically improving the efficiency of spectroscopic surveys at $z > 3$.

Photometric redshifts are the logical extension of color selection by estimating redshifts and spectral energy distributions (SEDs) from many photometric bands. Unlike color selection, photometric redshifts take advantage of all available information, enabling redshift estimates along with the age, star formation rate and mass.

Morphological selection of early-type galxies can be done using automated pipelines that isolate objects on the basis of their two-dimensional light distributions: this is the case of the first of the catalogs considered, the COSMOS survey. On the other hand within the GOODS database it is possible to select more accurately these objects by correlating a catalog of photometric and

spectroscopic redshifts with a morphological one, as we will see in the next Section.

5.2.1 COSMOS Survey

In this analysis, we use the Cosmic Evolution Survey (COSMOS) official photometric redshift catalog, designed to probe the evolution of galaxies in the context of their large scale structure out to moderate redshift. Details of the COSMOS catalog are described in Capak et al. (2007) and Mobasher et al. (2007). It covers a 2 square degree area with deep panchromatic data and includes objects whose total i magnitudes (i' or i^*) are brighter that 25.

The COSMOS multi-band catalog embraces data from different telescopes, as listed in Table 5.1, and Capak et al. (2007) present imaging data and photometry for this survey that cover various photometric bands between $0.3\ \mu m$ and $2.4\ \mu m$; the filter transmission profiles are plotted in Figure 5.4, in units of relative detector quantum efficiency normalized to 1 at the peak. The catalog was generated using SExtractor (Bertin & Arnouts 1996) and contains photometry measured over 3 arcsec diameter apertures for all the bands. All magnitudes are in the AB system. The cosmology adopted is: $H_0 = 70\ \Omega_M = 0.3\ \Omega_\Lambda = 0.7$ It also contains photometric redshifts, 68 and 95 percent confidence intervals and spectral types calculated with two different packages: the Mobasher et al. (2007) and BPZ Benítez (2000) codes.

The large database of this survey needs an automated and objective morphological classification technique. Our aim in this work is to separate early-type galaxies and the only selection possible is the morphological one, given by the automated pipeline parameter T_{phot}, which is based on a spectral type selection that separates elliptical galaxies, that we will consider in the comparison with our models, from spiral, irregular and starburst galaxies.

Table 5.1: COSMOS Survey: Telscopes and optical/IR bands

Telescope	Filters	Instrument λ Sensitivity Å
CFHT	u^*, i^*	3200-1000
CTIO	K_s	9000-25000
HST-ACS	F814W (i-band)	4000-11000
KPNO	K_s	9000-25000
SDSS	u, g, r, i, z	3200-11000
Subaru	B_J, V_J, g^+, r^+, i^+, z^+, NB816 (i-band)	4000-11000

We recovered all magnitudes and colors in the photometric system of the COSMOS survey for the three model galaxies. Colors and their cosmological evolution in different bands are shown in Figures 5.5, 5.6, and 5.7, where the $B_J - r^+$ (Subaru) , $r^+ - K_S$ (Subaru/KPNO), and the $g - r$ (SDSS) colors are plotted.

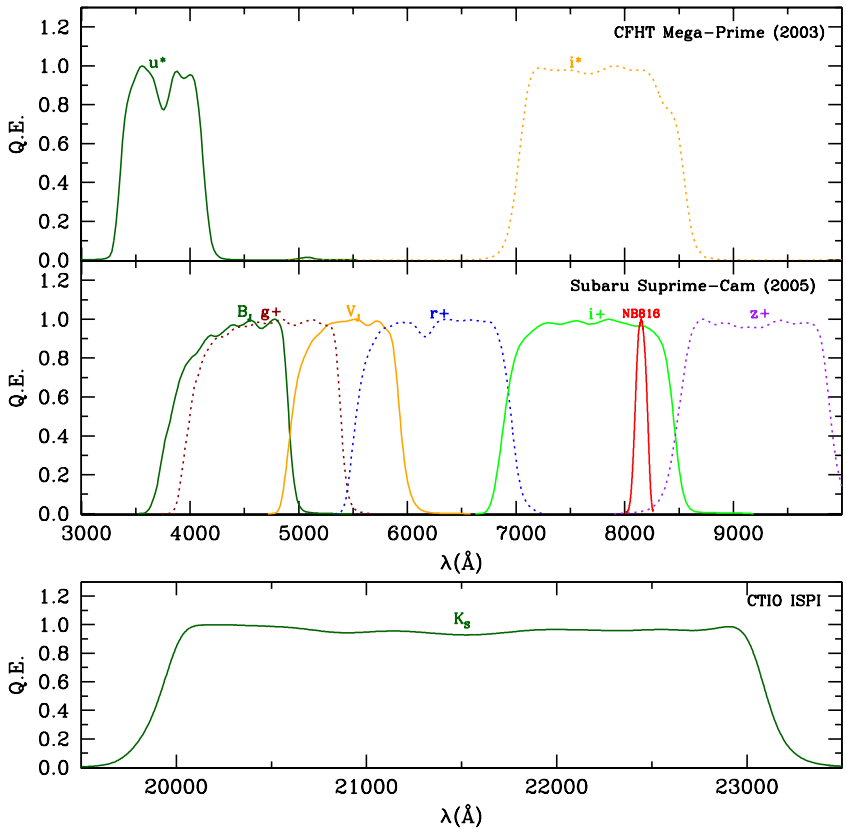

Figure 5.4: The filter transmission curves in units of relative detector quantum efficiency normalized to 1 at the peak for the COSMOS survey.

For comparison we plotted all the galaxies from the survey, independently of their classification, and superposed we distinguish the subsample of early-type galaxies selected following the classification suggested by the automated pipeline. Spectral types are distinguished with the T_{phot} parameter, and we have selected galaxies with $T_{phot} \leq 1.1$ that separate elliptical galaxies from the rest. The photometric evolution recovered for our three model galaxies is shown by the continuos (*SCDM* model) and dotted (ΛCDM models) lines that are overlapped to the data.

As can be noticed, the models follow the general trend of the observations and, in particular, are in reasonable agreement with those galaxies selected as elliptical. The three models tend to have redder colors with respect to the mean values and so are in better agreement with early-type galaxies with respect to the complete dataset, up to $z \sim 1$ in the specific case.

All colors seem to be slightly bluer than observational data, this effect might be reconduced

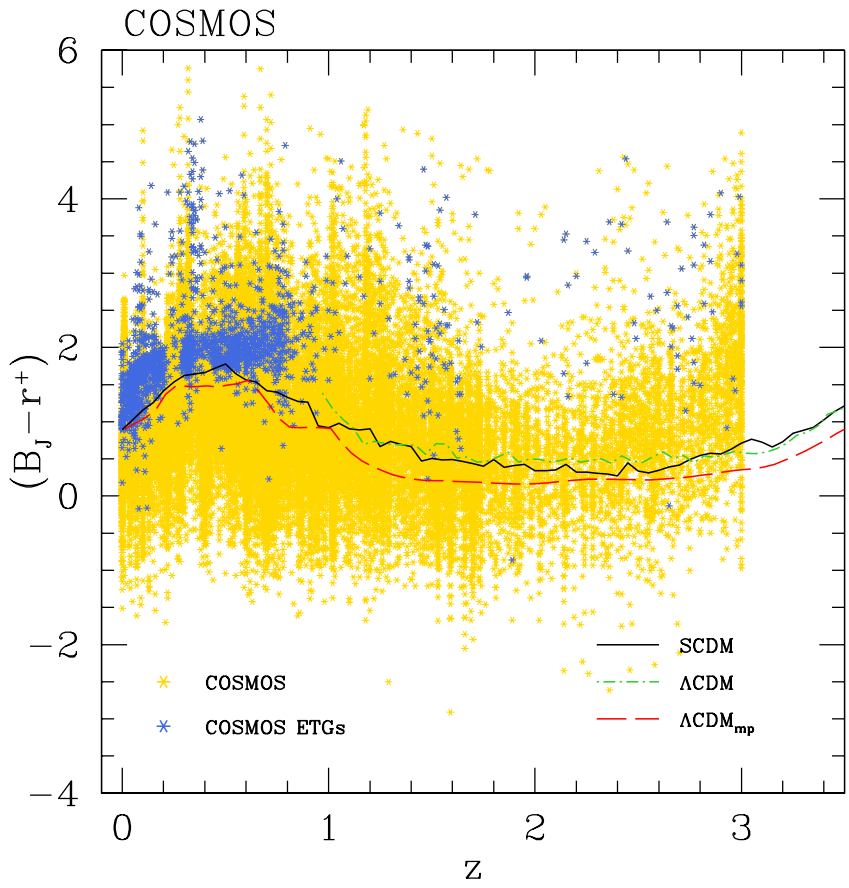

Figure 5.5: Cosmological evolution with redshift for the $(B_J - r^+)$ color of the COSMOS survey (both Subaru telescope bands). All galxies from the catalog are shown in yellow and the ETGs selected with the pipeline morphological $T_{phot} < 1.1$ parameter are marked in blue. Models of the simulated galaxies for the three different cosmological scenarios are shown superimposed to the data, continuous and dotted lines as labeled.

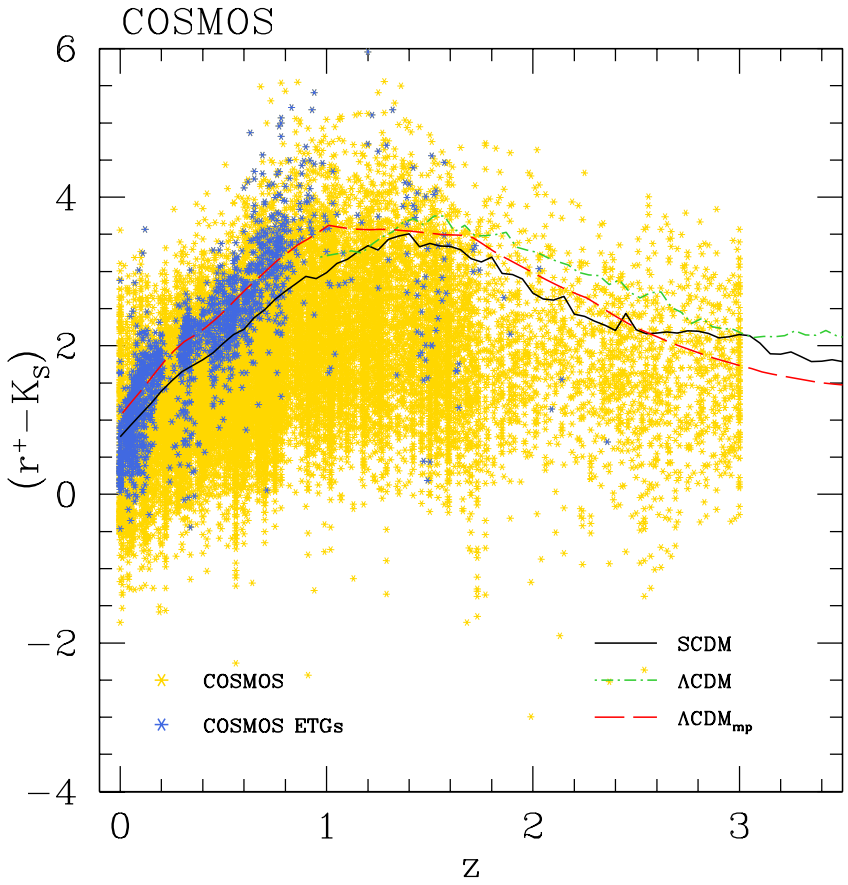

Figure 5.6: The same as Figure 5.5 but for the $(r^+ - K_S)$ colors (r^+ band from Subaru and K_S band from KPNO).

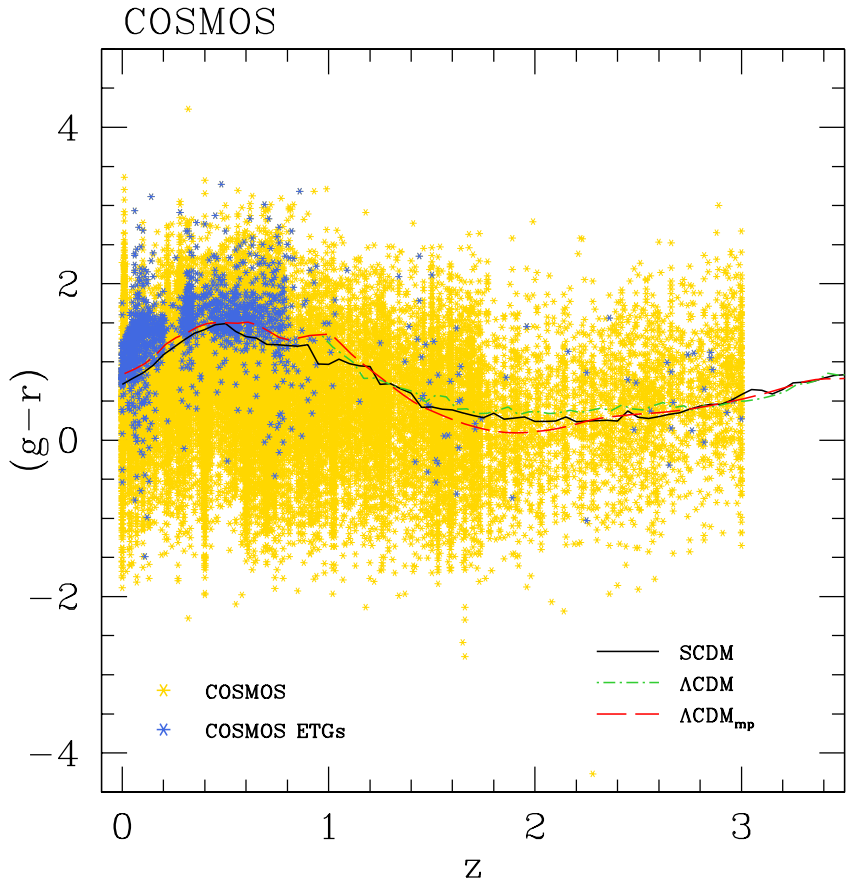

Figure 5.7: The same as Figure 5.5 but for the $(g-r)$ color (SDSS survey bands).

.

to the particular star formation history with which the simualted galaxies have been assembled and the issue will be argued in Chapter 7.

5.2.2 GOODS Database

Table 5.2: GOODS database: Telescopes and optical/IR bands

Telescope	Filters	Instrument λ Sensitivity $\AA$
ESO-WFI	U_{38}	3100-4000
VLT-VIMOS	U	3300-4000
ACS-HST	B(F435W), V(F606W), i(F775W), z(F850LP)	3400-11000
VLT-ISAAC	J, H, K_S	11000-24000
Spitzer - IRAC instrument	3.5, 4.5, 5.8, 8 μm	30000-100000

The second catalog we have considered for the comparison with the cosmological evolution of our simulated galaxy models is the Great Observatories Origins Deep Survey (GOODS) database.

The survey is based on observations of two separate fields centered on the HDFN and Chandra Deep Field South (CDFS) and includes ultradeep images from ACS on HST, from mid-IR satellite Spitzer, as well as from a number of ground-based facilities, as listed in Table 5.2.

Galaxies exhibit a range of morphologies that are difficult to qualify automatically, so classification by eye is often used to test the efficacy of automated classifiers. For this reason we have cross-correlated two catalogs that we will now describe: the GOODS-MUSIC from Grazian et al. (2006) for the redshift determination, together with the morphological one of Bundy et al. (2005), in order to select ETGs from the database. These are good catalogs to rely on: the first one has a precise redshift determination, infact Grazian et al. (2006) recover one of the best spectroscopic-photometric redshift correlation, the second has a reliable morphological determination by eye from which we selected early-type galxies.

The GOODS - MUltiwavelength Southern Infrared Catalog (GOODS-MUSIC) (Grazian et al. 2006) database comprises photometric and spectroscopic information for galaxies in the GOODS Southern Fied. They collected the spectroscopic information from public spectroscopic surveys and cross-correlated the spectroscopic redshifts with their photometric catalog. In Figure 12 of Grazian et al. (2006), is plotted the $z_{spec} - z_{phot}$ relation where they show the excellent agreement found between photometric and spectroscopic redshifts over the redshift range $0 < z < 6$. Up to now, it is the highest precision ever obtained on faint samples spanning such a wide range in redshift.

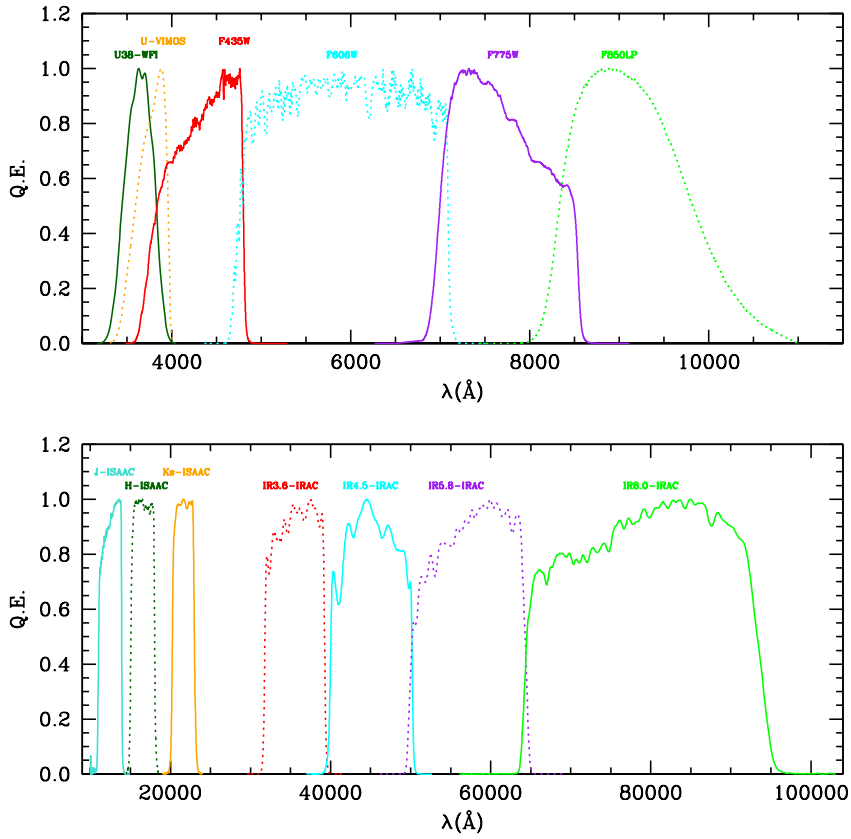

Figure 5.8: The filter transmission curves in units of relative detector quantum efficiency normalized to 1 at the peak for the GOODS database.

As already mentioned, morphological selection is one of the most difficult issues to cope with and a classification done by eye is certainly more reliable than the autometed classifiers. Bundy et al. (2005) presented a morphological catalog of galaxies in the GOODS North and South Fields, and the determination was done visually by them.

The study relies on the combination of many different data sets in the GOODS fields including infrared observations as listed in Table 5.2 and with filter response function shown in Figure 5.8, spectroscopic and photometric redshifts, and HST morphologies.

The catalog contains objects with a magnitude limit based on HST-ACS imaging data released by the GOODS team (Giavalisco et al. 2004), a z-band selected catalog was constructed with a magnitude limit of $z_{AB} < 22.5$, where reliable visual morphological classification was deemed possible, and, for instance, all magnitudes are defined in the ABmag system. They as-

sume a cosmological model with $\Omega_M = 0.3$, $\Omega_\Lambda = 0.7$, and $H_0 = 70\ km\ s^{-1}\ Mpc^{-1}$. Their final catalog contains 928 galaxies with spectroscopic redshift, 668 of which with reliable redshift determination.

The resulting sample of 2978 objects over both GOODS fields was inspected visually by Bundy et al. (2005) who classified each object using the technique discussed in Brinchmann & Ellis (2000) according to a scale that separates stars form compact objects and galaxies of different morphological type.

We cross-correlated the two catalogs described above to recover a dataset of galaxies with a reliable morphological classification and a precise redshift determiantion, and for this reason these galaxies should be retained of better selection than the one defined with COSMOS. Following this criteria, a subsample of elliptical galaxies is selected from the complete database recovering 118 elliptical galaxies.

In Figures 5.9, 5.10, and 5.11 are shown the $(V-i)$, $(V-z)$, and $(V-K_S)$ colors respectively. For all of the colors shown there is good agreement for the photometric cosmological evolution with redshift between the simulated galaxies and the observational data.

Theoretical colors seem to match better with GOODS data than what found for the COSMOS survey. Having a better morphological classificator, the selection is done by eye for GOODS in contrast to the automated pipelines used for COSMOS, is certainly discriminating in favour of this second database. For both datasets we can see how colors simulated in the different cosmological scenarios follow a general trend at lower redshifts, thus following a slightly different trend only for values of $z \sim 1$, where the number of early-type galaxies observed falls abruptly. Within this redshift range the simulated colors reproduce well the observational data.

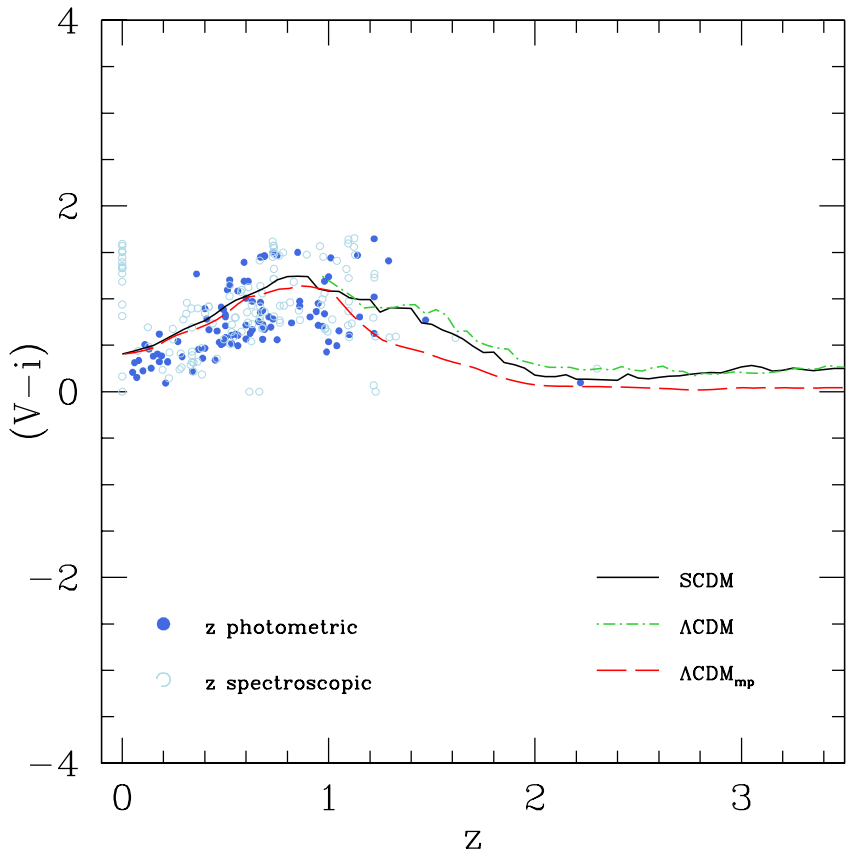

Figure 5.9: Cosmological evolution with redshift for the $V(F606W) - i(F775W)$ colors of the GOODS survey (ACS-HST bands) for early-type galxies with spectroscopic (light blue-empty circle) and photometric (blue-filled circles) redshift determination as indicated. Models of the simulated galaxies for the three different cosmological scenarios are shown superimposed to the data, continuous and dotted lines as labeled.

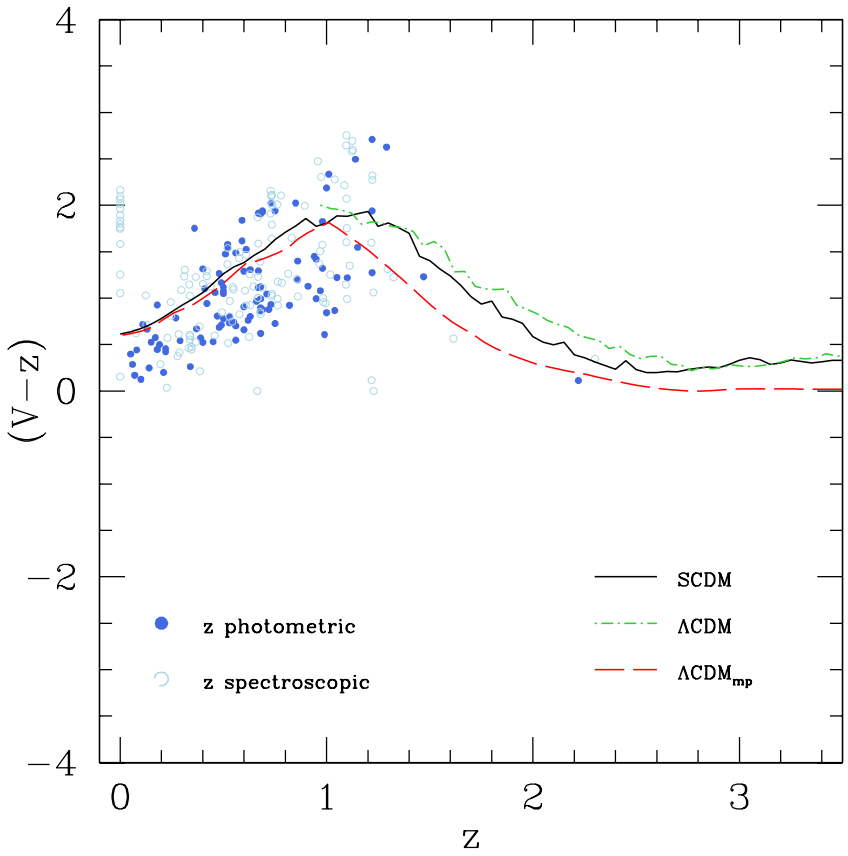

Figure 5.10: The same as Figure 5.9 but for the $V(F606W) - z(F850LP)$ colors (ACS-HST bands).

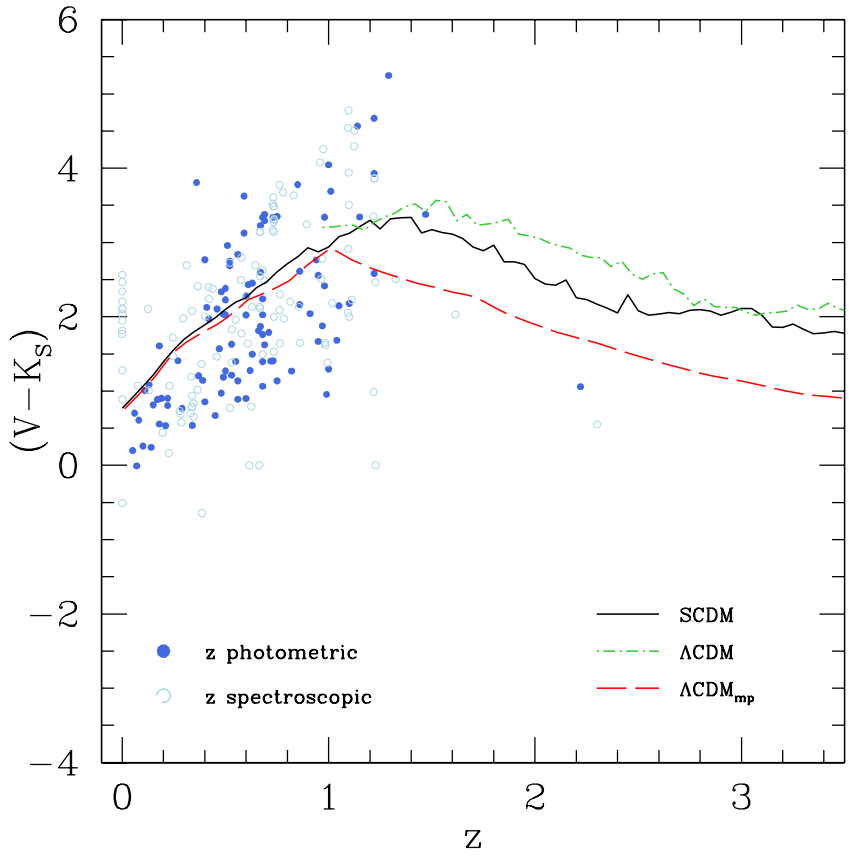

Figure 5.11: The same as Figure 5.9 but for the $V(F606W) - K_S$ colors (V band from ACS-HST and K_S band from VLT-ISAAC).

Chapter 6

Artificial Images of ETGs

Early-type galaxies (ETGs) are a remarkably regular family of stellar systems and they have similar structural and dynamical properties, as photometric and spectroscopic observations tell us. However, many relevant observable quantities depend systematically on their global properties: their mass, radius, or luminosity. The uniform nature of ETGs strongly suggests a common formation scenario for this family of objects, and, no matter which, it must have to reproduce all the observed properties. That is, any formation scenario that involves a formation mechanism, must produce a systematic variation of the galaxy's properties from the small to the largest mass scales. ETGs satisfy some notable empirical scaling laws, among which the most significant is the Fundamental Plane (Djorgovski & Davis 1987), usually used in extragalactic distance scale studies.

In this Section we will show how, starting from a three-dimensional numerical simulation of a galaxy we can add photometry and recover 'artficial' images in a bi-dimensional plane, from which structural parameters, such as the effective radius and effective luminosity, can be derived. These parameters allow us to compare our simulated results with the observational data within the scaling laws, and especially the Kormendy relation, a projection of the Fundamental Plane in the luminosity-radius plane.

The multiwavelength photometric properties which are examined are derived, first of all, by building artificial images in terms of fluxes or magnitudes in a given photometric system, and afterwards analyzing them as if they were realistic images of galaxies taken with a telescope. In particular we have worked within the SDSS photometric system, whose characteristics have been described in Section 3.3, in the work carried on throughout this Chapter.

Surface photometry represents one of the most important and most powerful tools to study the properties and history of elliptical galaxies. The analysis technique adopted is based on fitting ellipses to the isophotes of the galaxy. The oldest proposed model to fit the radial intensity profile is the empirical "*de Vaucouleurs law*" (de Vaucouleurs 1948) that has now been extended

with the more flexible "*Sérsic profile*". The derived properties, of which the most important are the intensity distribution, the radial ellipticity and the position angle profiles, provide basic information such as effective radius, deviations from ellipses, isophote twisting, triaxiality and absolute magnitudes. The associated higher order Fourier coefficients from the fits reveal the intrinsic "boxy" or "disky" appearance of the isophotes which can be used to uncover underlying stellar components.

We focus on the global photometric properties, such as the luminosities, magnitudes, and the colors of the target galaxy, which are obtained from these projected images by analyzing these in same way as in the analysis of observational imaging data. In this way we derive not only intensity profiles, but also all the related radial profiles such as color and structural radial profiles.

Structural parameters are derived for the SDSS photometric system, this allows a comparison between the luminosities and effective radii we derive for the simulated galaxies and a set of early-type galaxies selcted from the survey, within the Kormendy law that relates the two above mentioned parameters.

6.1 Artificial Images

Since the observational data which our results should be compared with provide the luminosity distribution projected onto a plane, we need to derive a bi-dimensional projection of the three-dimensional distribution of star particles of the simulated galaxy. With this regard, we can construct synthetic images projected onto one of the planes that will be hence analyzed: these provide information similar to the imaging data obtained in actual observations.

Galaxies are observed in projection on the sky: in order to compare the simulated results with observations we construct photometric images of the simulated cosmo-chemo-dynamical three-dimansional galaxies introduced in Chapter 4 and recover galaxy images as the projection of $|z| < 100\ kpc$ on the $x-y$ plane. The output we have from the simulated galaxy are the space coordinates of particles and the corresponding value of the flux computed with the evolutionary synthesis technique. We create a grid of this projection of the galaxy onto a plane and derive the projected distribution of the SEDs starting from the three-dimensional structure and compute for each grid point the total flux considering all particles along the third direction (the line of sight). These fluxes are fed to the photometric code that computes the magnitude and/or color in a given band, as described in Chapters 3 and 4, for each mesh point of the grid and, in this way, create an artificial image.

These artificial images were created by deriving a mesh large enough to encompass the star particles of the model galaxy and with a different number of grid points in order to have varying

scale lengths that create a smooth image. A length of $80-100\ kpc$ covers a wide enough region that includes all particles and a mesh of a number of $100-200$ grid points is good to create a smooth image; the best combination in order to obtain a satisfactory result is a scale of 0.4 to 0.8 kpc per grid point. In Table 6.1 is shown for reference the resolution with which images have been created: the selection of the scale depends on the singular galaxy and the diameter it reaches.

Table 6.1: Artifial images construction: dimensions and grid scales

	40 kpc	60 kpc	80 kpc	100 kpc	200 kpc
50 gp	0.8 $\frac{kpc}{gp}$	1.2	1.6	2.0	4.0
100 gp	0.4	0.6	0.8	1.0	2.0
200 gp	0.2	0.3	0.4	0.5	1.0
500 gp	0.08	0.12	0.16	0.2	0.4

Images have been constructed for the last output of the galaxy simulation, at an age defined in Table 4.3. In Figure 6.1 is shown the two-dimensional distribution of the simulated optical *r*-band magnitude image in the SDSS photometric system for the model galaxies at the last age of evolution, where a 200×200 mesh points has been chosen to span a square region of side 80 kpc. In all models the old stars appear to have the morphology of an elliptical galaxy. Upper panel refers to the *SCDM* model, middle to the ΛCDM, and lower to the ΛCDM_{mp}, whose properties have been defined in Chapter 4.

In displaying the frames of these elliptical galaxies, the intensity contrast between the bright central regions of ellipticals and the low surface brightness of the outer parts is very difficult to portray using a linear relation, for this reason it is better to display the image with a logarithmic transformation.

6.2 Isophotal Analysis

In the following analysis we use images similar to the ones displayed in the Figure 6.1 above but we employ a 100×100 pixel mesh to span a square region of side 80 kpc.

This resulting image is analyzed with the IRAF package *stsdas.isophot* and the tasks within in the way desribed as follows.

The procedure that we will briefly outline is designed for predominantly elliptical isophotes. The algorithm used for the photometric analysis extracts the intensity levels from the image and fits ellipses to all the points at the same intensity level determining the center, the ellipticity, the position angle, and the semi-major axis length. The isophotes are representable by ellipses,

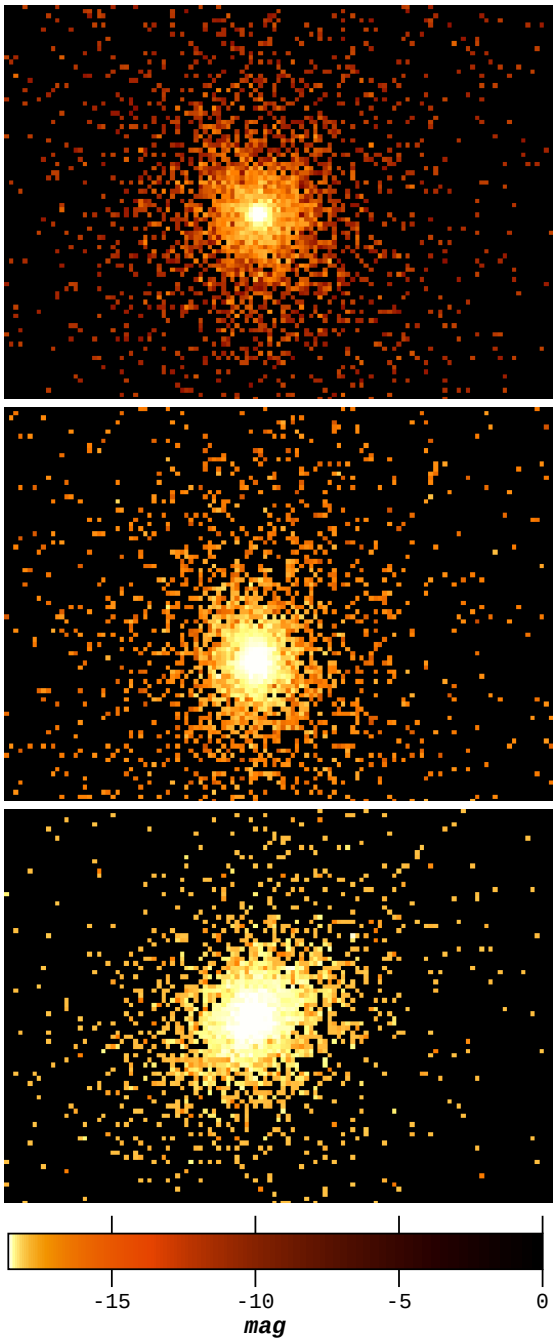

Figure 6.1: r-band artificial image of a $80 \times 80\ kpc^2$ region with a 200×200 mesh points for the last age of the evolution of the model galaxies: *SCDM* upper, ΛCDM middle, ΛCDM_{mp} lower.

however small but significative deviations from pure ellipses are also measured. These quantities are measured by working on the coordinates of the points on an isophote and are recovered via a Fourier analysis on the distance of the contour points of the ellipses as a function of the azimuthal angle. This method uses all the data from the galaxy image and calculates the ellipse center, the ellipticity, the position angle, and the non-ellipse coefficients.

The IRAF task *ellipse* has been designed explicitly for the derivation of a galaxy brightness distribution and is used to fit elliptical isophotes to the galaxy's image, and to measure isophotal parameters for each simulated galaxy in all filters of the SDSS photometric system. It produces as output the parameters for each fitted isophote. *Ellipse* adopts the methodology described in Jedrzejewski (1987): for each semi-major axis length, the intensity in the galaxy image around the ellipse $I(\phi)$ is azimuthally sampled along an elliptical path described by an initial guess for the isophote's center coordinates (X,Y), ellipticity (ε), and semi-major axis position angle (ϕ). $I(\phi)$ is then expanded into a Fourier series as:

$$I(\phi) = I_0 + \sum_k [A_k \sin(k\phi) + B_k \cos(k\phi)]. \tag{6.1}$$

The best fitting set of parameters $X, Y, \varepsilon, \theta$ are those that minimize the sum of the squares of the residuals between the data and the ellipse when the expansion is truncated to the first two moments (which completely describe an ellipse). The image is sampled along an elliptical path producing an intensity profile in function of the position angle that is fitted by weighted least-squares:

$$I = I_0 + A_1 \sin(\phi) + B_1 \cos(\phi) + A_2 \sin(2\phi) + B_2 \cos(2\phi) \tag{6.2}$$

Each one of the harmonic amplitudes A_1, B_1, A_2, B_2 is related to a specific ellipse geometric parameter in the sense that it gives information on how much the parameter derived deviates from the 'true' one, so they give the errors in the fitting procedure. The image data sample is fitted by the following function

$$I = I_0 + A_3 \sin(3\phi) + B_3 \cos(3\phi) + A_4 \sin(4\phi) + B_4 \cos(4\phi), \tag{6.3}$$

where the amplitudes A_3, B_3, A_4, B_4 measure the isophote's deviations from perfect ellipticity.

Higher order moments ($k \geq 3$) define deviations of the isophotes from ellipses. In practice, moments beyond the fourth cannot be measured accurately; third and fourth-order moments are calculated from the equation above by fixing the first and second-order moments to their best-fit values. The third-order moments (A_3 and B_3) represent isophotes with three-fold deviations from ellipses (e.g., egg-shaped or heart-shaped) while the fourth-order moments (A_4 and B_4) represent four-fold deviations. Rhomboidal or diamond-shaped isophotes translate into a non-zero A_4. For galaxies which are not distorted by interactions, B_4 is the most meaningful moment: a positive B_4 indicates "disky" isophotes (i.e., with semi-major axis $B_4 \times 100$ percent longer than

the best fitting ellipse), while a negative B_4 indicates "boxy" isophotes (i.e., with semi-major axis $B_4 \times 100$ percent shorter than the best fitting ellipse; Jedrzejewski (1987)).

When running *ellipse* on the program galaxies, we adopted the following guidelines. The semi-major axis length was increased logarithmically, i.e., each isophote was calculated at a semi-major axis 10% longer than that of the isophote preceding it, and the new interation started using the best-fit parameters from the previous isophote. In general, all parameters were allowed to vary freely, although in some cases it fails to converge on isophotes which display large deviation from ellipses: in such cases to achieve convergence it was found necessary to fix the value of one or more parameters. The isophotal center was not allowed to wander by more than 2 grid points between consecutive isophotes; in practice, when X and Y were allowed to vary, the center was found to be stable.

The x-coordinate is the equivalent radius of the best-fitting ellipse, that is, the 'geometric mean', r_{geo}, of the semi-major and semi-minor axes, defined as:

$$r = a\sqrt{1-\varepsilon(a)} \tag{6.4}$$

where a is the radius measured along the isophotal semi-major axis. This has the effect of reducing all profiles to equivalent circular profiles.

Then the integrated intensity is measured within the corresponding circle with the same center and radius equal to the semi-major axis length. After the fitting that corresponds to the first guess of the semi-major axis value is done, the axis length is incremented. In this way we are able to recover radial profiles in function of the semi-major axis length of the mean isophotal intensity, ellipticity, position angle, local radial intensity gradient, mean isophotal magnitude, and 3^{rd} and 4^{th} order deviations from ellipse.

Errors in intensity, magnitude and gradient are obtained from the rms scatter of intensity data along the fitted ellipse. Ellipse geometry parameter errors are obtained from the internal errors in the harmonic fit, after removal of the first and second fitted harmonics. Harmonic amplitude errors are obtained from the fit error after removal of all harmonics up to and including, the one being considered.

After using the *ellipse* task to measure the mean radial intensity profiles and fit ellipses to the image, the program *bmodel* was then used to reconstruct a model image from the results of isophotal analysis. The *bmodel* task creates a 2-dimensional model image containing a noiseless photometric model of a source image. The model is built from the results of isophotal analysis generated by the isophote fitting task, *ellipse*. In Figure 6.2 are shown the derive smooth models for the three simulations corresponding to the images in Figure 6.1, whereas in Figure 6.3 are shown the model images with the elliptical isophotes overlapped.

The 3rd and 4th harmonics from the photometry are added to the model. This option is most useful when working close to the central intensity peak. As explained in Jedrzejewski's paper

the sampling at small radii is prone to introduce a "boxy" component. More accurate modelling at the central region is generally achieved when including this component.

6.3 Parametrization of the Intensity Profile

The intensities $I(r)$ and corresponding surface brightnesses $\mu(r)$ at the effective radius r_e are related by the Sérsic law as:

$$I(r) = I_e \exp\left\{ b_n \left[\left(\frac{r}{r_e} \right)^{1/n} - 1 \right] \right\}, \tag{6.5}$$

where I_b is the central intensity;

$$\mu(r) = \mu_e - 2.5 b_n \left[\left(\frac{r}{r_e} \right)^{1/n} - 1 \right] \log e. \tag{6.6}$$

For a Sérsic model with values of $n \geq 1$, that is $1 \lesssim n \lesssim 10$, the effective radius r_e contains roughly half the integrated light of the model if approximated by the form $b_n = 2n - 0.324$ (Trujillo, Graham & Caon 2001). Effectively, therefore, the number of free parameters in a Sérsic model is three. The parameter n controls the overall shape of a Sérsic profile, with low n values producing curved profiles with logarithmic slopes which are shallow in the inner regions, and steep in the outer parts, while high n values produce extended profiles with less overall curvature (i.e. steep inner profiles and shallow outer profiles).

Conveniently, the parameters are chosen such that the model reduces to the de Vaucouleurs law for a value of $n = 4$, while also staying consistent with the usual interpretation of r_e coinciding with the half-light radius.

The Sérsic model offers significant advantages. First and foremost, they provide a good description of the inner (100 pc scale) profiles, and a significantly better description when the profiles are extended to kpc-scale (Graham et al. 2003; Trujillo et al. 2004).

The intensity profile has been fitted with the aid of the *nfit1d* task that fits 1-dimensional, non-linear functions to the image. Chi-square fitting is performed. As the task supports any form of interpreted function, which allows the fit of almost any analytic function, given the initial guesses for the function coefficients, we have fitted the intensity profile of the simulated galaxy with a Sérsic law with varying index.

We fitted the intensity profile with the Sérsic law allowing the index n to vary, together with the effective radius R_e and the effective intensity I_e values. Figure 6.4 shows the best fitting Sérsic function for the r-band in the particular sample; the profile inside a region equal to $1-2$ times the softening length (described in §4.2.2), that in our case amounts to $1-2$ kpc, was excluded from the fit as it is likely to be influenced by force softening. In the outer region,

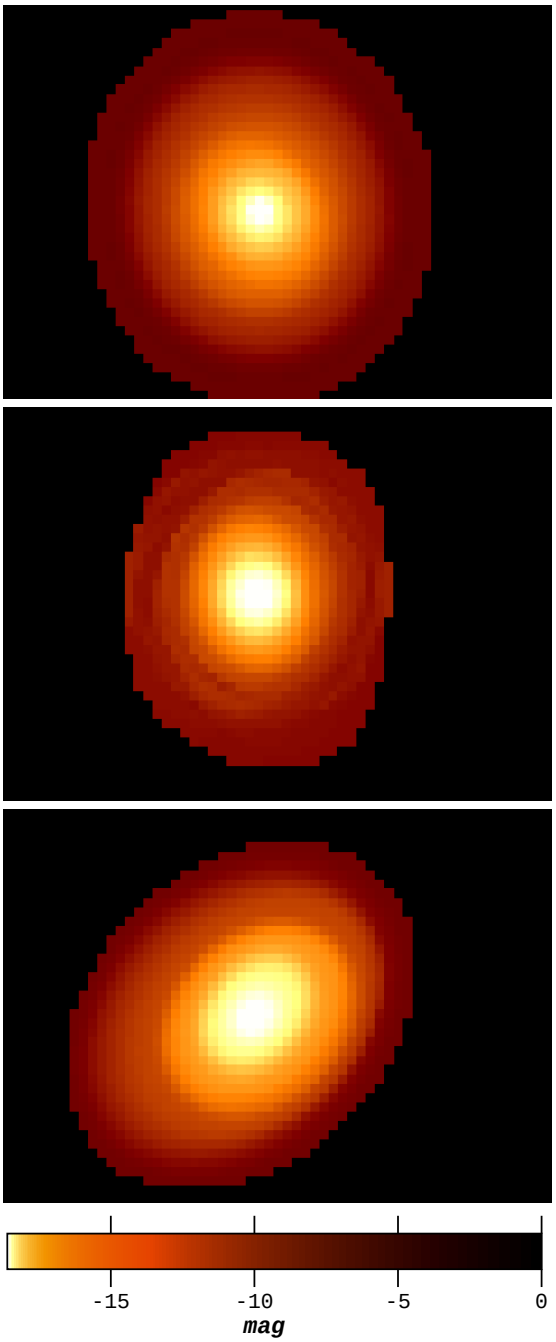

Figure 6.2: The two-dimensional models of the optical r-band magnitude in the xy-plane of the images shown in Figure 6.1.

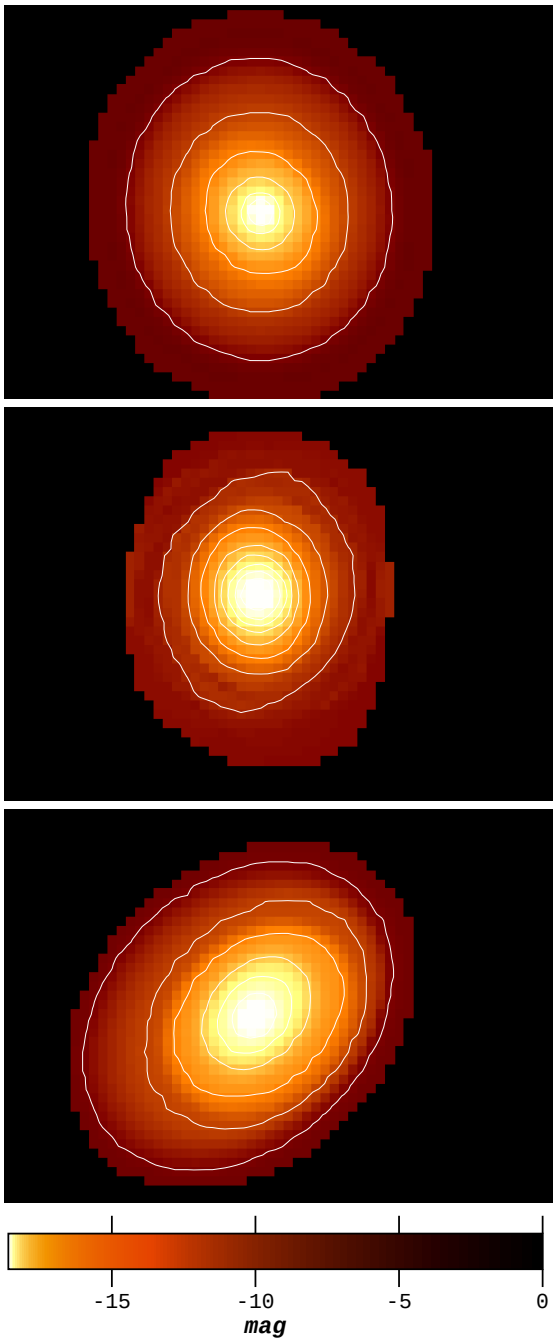

Figure 6.3: The same as Figure 6.2 but with elliptical isophotes are superimposed.

to derive the proper effective radii in the simulation, we reach large enough regions such as $40 - 80\ kpc$. The solid curve represents the best-fit Sérsic model to the final profile (shown as

solid symbols).

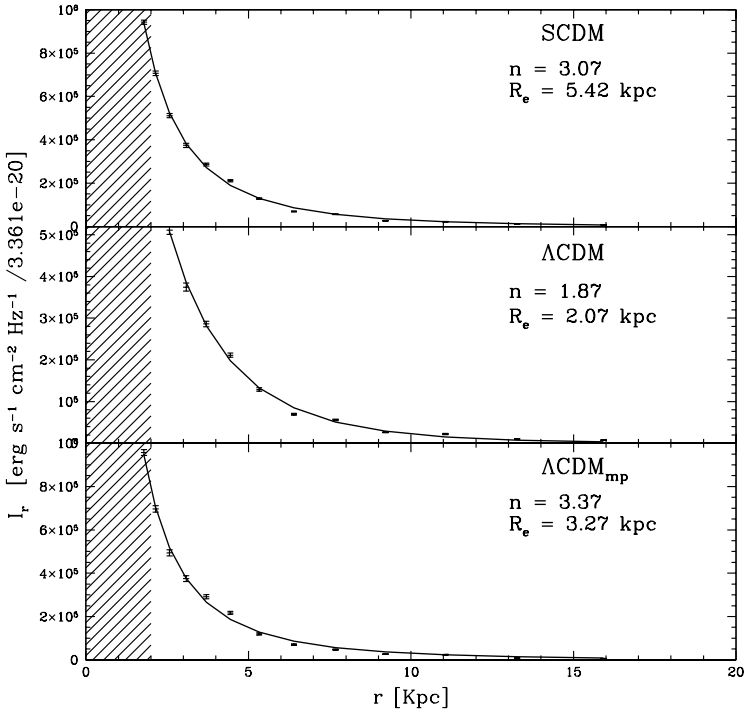

Figure 6.4: Intensity profiles fitted with a Sérsic law of variable index. The *r*-band Sérsic index of n and the effective radius R_e are specified in panel for the three models. We exclude the central region within $r \sim 1-2\ kpc$ (shaded area) when fitting intensity, because the profile is smeared out due to the softening of the gravity.

From the fitted profiles of intensity and with the best-fit parameters in hand, we calculated the effective radii R_e and the total magnitudes in all bands. Values recovered for the index n and the effective radius R_e for the simulated models and in the different bands are summarized in Table 6.2.

What results is that the effective radius varies in function of the band in which is computed, decreasing as the band moves toward the higher wavelengths. Bernardi et al. (2003c) found that half-light angular sizes of the galaxies in their sample are indeed larger in the bluer bands and they show how the effective physical radii in their sample changes in the four[1] bands. For what concerns our results, we find that this trend is followed by the simulated galaxies we consider:

[1]They exclude the *u*-band as the measurements are affected by errors larger than the others

Table 6.2: Sérsic indexes and effective radii, expressed in kpc for the SDSS photometric passbands and for all model galaxies.

	SCDM		ΛCDM		ΛCDM_{mp}	
band	n	R_e	n	R_e	n	R_e
u	3.22	6.42	2.2	2.38	3.97	4.31
g	3.08	5.78	2.1	2.43	3.69	3.67
r	3.07	5.42	1.87	2.7	3.37	3.27
i	3.86	5.83	1.99	2.73	3.14	3.07
z	4.42	5.98	2.21	2.6	2.94	2.95

there is particular good agreement for the ΛCDM_{mp} model. The other two models follow this trend for the bluer bands, the radius increases again toward the longer wavelengths.

6.3.1 Structural and Photometric Properites

The results of the analysis for the simulated model galaxies are shown in Figure 6.5 for the *SCDM*, ΛCDM, and Λ, CDM_{mp} models respectively, for instance, results are shown for the r-band image. Ellipticity ε, position angle ϕ (measured in degrees from North to East) of the major axis, and deviation of the isophotes from pure ellipses are plotted in Figure 6.5 as a function of the 'geometric mean' radius r_{geo}, as defined in Eq. 6.4, for all the model galaxies.

Although the isophotes shown in Figure 6.3 are well approximated by ellipses, small but significant deviations from perfect ellipsoidal shapes are also robustly measured. Of particular interest is the a_4[2] parameter, which measures $m = 4$ deviations from perfect ellipses: $a_4 < 0$ signals 'boxy' isophotes, whereas $a_4 > 0$ implies 'disky' deviations from perfect ellipses.

The radial profile of the a_4 parameter indicates that the deviations from perfect ellipses are generally negligibly small for the *SCDM* and ΛCDM_{mp} models, thus showing no obvious features. The ΛCDM show negative values of the a_4 parameter in the outer region telling us that there is a boxy structure.

[2] a_4 corresponds to the fourth order moment B_4 of Eq. 6.3

6.4 Color Profiles

Deep multi-band photometry of elliptical galaxies reveal color gradients in their radial profiles. As mentioned before, Bernardi et al. (2003c) found that half-light angular sizes of the galaxies change in function of the band in which they are measured, finding larger radii at bluer bands. On average, the fact that ETGs have this trend indicates that they present color gradients. It is known from observations that these gradients are such that ETGs are redder in their cores and become continuously bluer with increasing radius, towards their edges. This fact is thought to originate from variations in age or metallicity of the stellar population (e.g. Worthey 1994, Tantalo et al. (1998)).

One of the goals of this work is to derive the radial color profiles of the simulated galaxies, and we extract these with the help of surface photometry analysis. Figures 6.6, 6.7, and 6.8 show the $u-g$, $g-r$, $r-i$, and $i-z$ color profiles in the SDSS photometric system for the three model galaxies.

Observed elliptical galaxies show a mild propensity for reddish cores, which is not reproduced in the simulated galaxies, except for the ΛCDM_{mp} model. The physical processes considered, that characterize the formation of the simulated galaxy, lead to a fairly uniform stellar component with little sign of radial gradients in stellar age for the *SCDM* and ΛCDM models as shown in Figures 6.6 and 6.7, whereas the ΛCDM_{mp} model has a color gradient that varies with the radius, as shown in Figure 6.8. What we find from the analysis of the the simulated galaxies is that colors get bluer towards larger radii, apart from the core of the galaxy for models *SCDM* and ΛCDM that is bluer, within a few kpc, while the ΛCDM_{mp} shows a reddish core. This issue will be discussed in Chapter 7.

6.5 The Kormendy Relation

A powerful diagnostic of the success of simulations in reproducing the observed properties of galaxies results from comparing their photometric and structural properties, such as the luminosity and size, within the scaling relations linking these properties in galaxies of various types.

The Kormendy relation is the projection of the more general and significant FP in the luminosity-radius: it is used to determine the luminosity evolution of the ETGs and gives useful information on physical mechanisms involved in the galaxy's evolution.

The SDSS Sample

For a reliable comparison we have chosen a subsample of ETGs from the Sloan Digital Sky Survey (SDSS; York 2000, Stoughton 2002) database. The SDSS survey has mapped in detail

one-quarter of the entire sky, producing a detailed image of it and determining the positions and photometric properties of more than 100 million celestial objects.

The SDSS obtains high-resolution imaging in five different bands that allow a reliable identification of early-type galaxies and precise measurements of their photometric properties. Five bandpasses (*u, g, r, i, z*) centered in (3560, 4680, 6180, 7500, 8870 *Å*) (Fukugita et al. (1996)).

Galxies can be selected using automated pipelines that isolate objects on the basis of their two-dimensional light distributions. We consider early-type galaxies from the DR2 release selected following the criteria described in Bernardi et al. (2003c): they have constructed a catalog of ~ 9000 low-redshift early-type galaxies, selected using a combination of SDSS pipeline parameters. This catalog contains galaxies with a high *i*-band concentration index $(r_{50}/r_{90}) > 2.5$ and in which a de Vaucouleurs (1948) fit to the surface brightness profile is significantly more likely than an exponential fit. Details of the selection can be found in Bernardi et al. (2003c).

In Figure 6.9 we show the magnitude-radius relation, e.g, in the *r*-band for the three simulated galaxies considered in this work. Values of effective radius and magnitude have been recovered by analyzing the synthetic bi-dimensional images created with the method described in the previous sections. Two of the models, the *SCDM* and the ΛCDM_{mp} seem to lie next to the average value that described quite well the observational trend that galaxies follow. The third galaxy, the ΛCDM model, appears to detach from the observational fit. An explanation might be that the numerical simulation that follows its evolution stopped at a redshift of $z \sim 1$, thus not letting the galaxy form completely, but at roughly half of the formation. Even if at this ages the star formation has already stopped (see Figure 4.1) and the galaxy evolves passively after, this has to be taken into account since we could argue that if the simulation would have reached the end, magnitudes would continue evolving. Looking at the rest-frame magnitude evolution for the galaxies in Figure 4.10, we note that, for all bands, magnitudes reach a minimum value after which, in the last stages of the evolution, they increase towards higher magnitudes. In this sense, we suppose the point would move towards the average values descibed by the fitted line and fall on the region covered by the observational data.

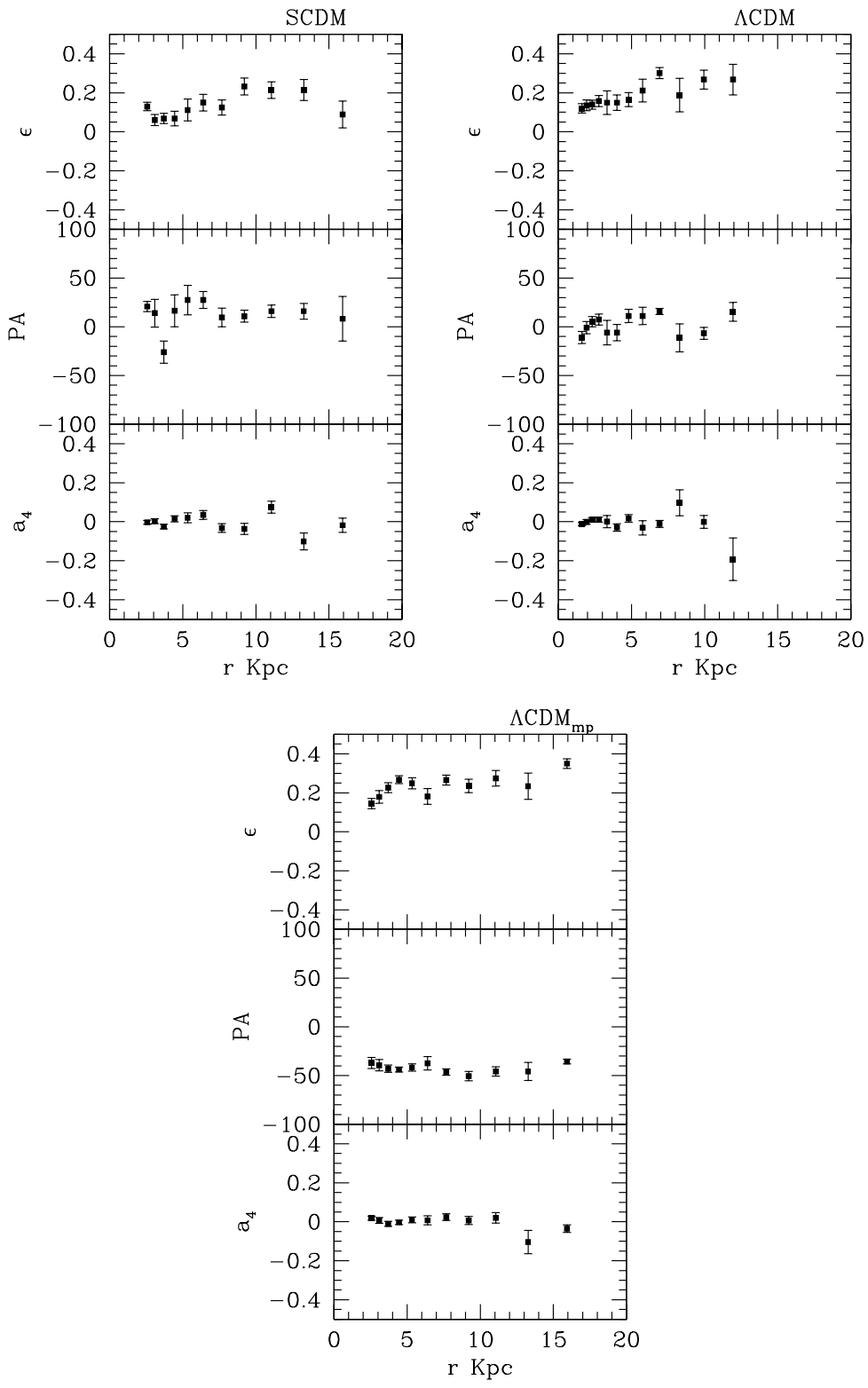

Figure 6.5: Ellipticity ε, position angle *PA*, and a_4 radial profiles of the galaxy versus the radius *r* for the *SCDM* model.

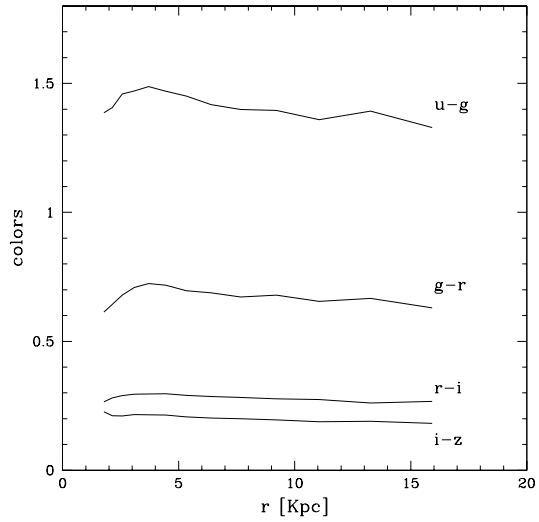

Figure 6.6: Radial profiles of the *SDSS* colors for the *SCDM* model derived from the simulated image 100×100 grid points shown in Figure 6.1

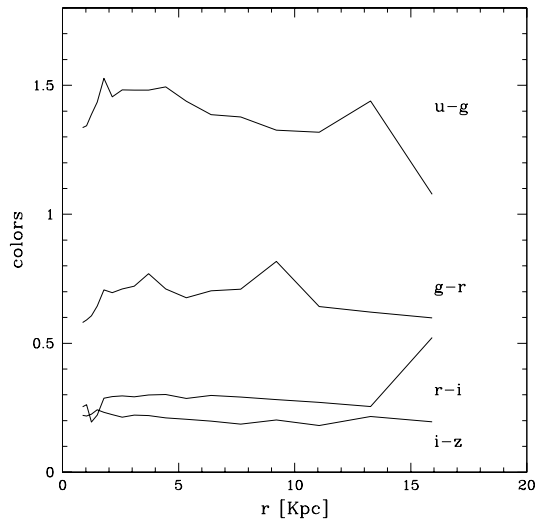

Figure 6.7: Radial profiles of the colors for the Λ*CDM* derived from the simulated image 100×100 grid points shown in Figure 6.1

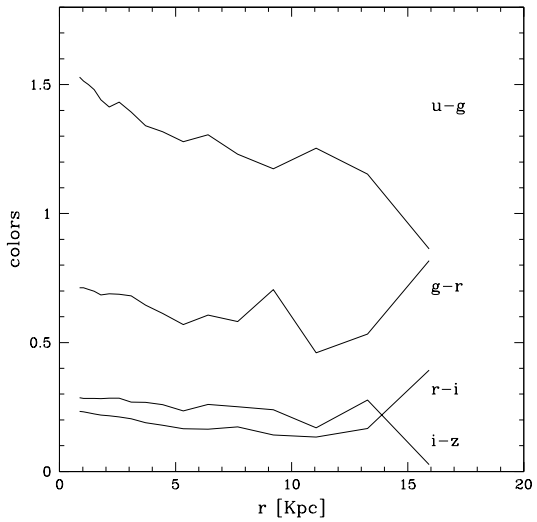

Figure 6.8: Radial profiles of the colors for the ΛCDM_{mp} derived from the simulated image 100×100 grid points shown in Figure 6.1

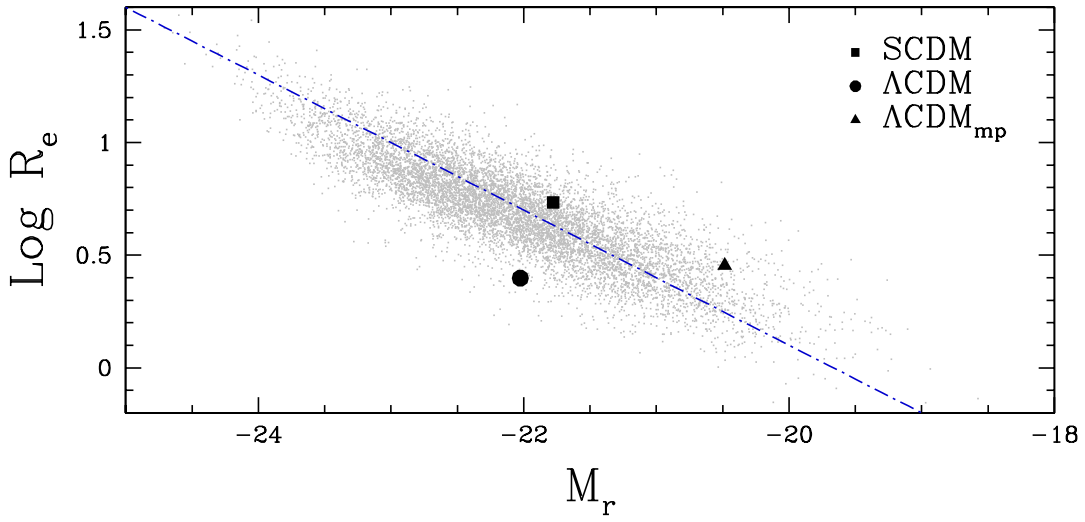

Figure 6.9: Kormendy relation in the *r*-band for ETGs selected from the SDSS DR2 database following the criteria from Bernardi et al. (2003c). Model galaxies for the three models, as labeled, with the parameters recovered form the analysis of the artificial images.

Chapter 7

Discussion

We have described the synthetic photometry algorithm and the various applications to template galaxies in numerical simulations that provide magnitudes and colors computed from a spectral energy flux distribution and the response functions of a photometric system.

We have so far presented the main results that we will here discuss: the evolution of colors of ETGs in several photometric bands in the rest-frame; the evolution in a cosmological context and the comparison with galaxies selected from the database of two surveys; the derivation of artificial images from which we recover morphological and structural parameters; and the comparison with observable data within the scaling relations.

Evolution with redshift

In tracking the evolution with redshift, one potential problem for studies of massive ETGs is the morphological classification that allows to select galaxies that can be compared to our simulated objects.

We have considered two of the present-day most important surveys of cosmological evolution and presented the results in Chapter 5. Colors derived for the simulated galaxies are consistent with the general trend followed by the observational data (see Figures 5.5, 5.6, and 5.7), when considering all the galaxies form the COSMOS catalog. In particular synthetic colors are in good agreement with those galaxies selected as ellipticals, up to $z \sim 1$, which show however slightly bluer colors than observable data. For the galaxies selected from the GOODS database, theoretical colors seem to match better with data than what found for the COSMOS galaxies (see Figures 5.9, 5.10, and 5.11).

An important issue is the reliability of the objects selected. Having a good morphological classificator is essential when considering a defined class of objects: the selection in the GOODS database is done by correlating two catalogs, one that comprises photometric and spectroscopic

redshifts and a morphological one where classification is done by eye, as described in Section 5.2.2. In contrast, the selection derived from the COSMOS database follows the automated pipelines classification; this is certainly discriminating in favour of the GOODS database of elliptical galaxies. For both datasets however, we can see how colors simulated for the different cosmological scenarios follow the general trend at lower redshifts and in good agreement with the data up of $z \sim 1$, where the number of observed ETGs falls abruptly. Within this redshift range all the simulated colors reproduce quite well the observational data.

Artificial images

As we have seen in Chapter 6, the basic idea is to create two-dimensional artificial images of the three-dimensional simulated galaxies that can be analyzed photometrically with the same criteria followed for the imaging of observational data. The derived global properties, photometric and structural parameters, such as their light distribution in different broadbands, are compared with those we obtain from elliptical galaxies selected form the database of one of the major present day surveys, the Sloan Digital Sky Survey. This comparison with published observations allow us to understand if the current modelling does indeed explain the properties of real galaxies, or if our theoretical understanding of such events needs to be modified. For instance, these artificial images have been created for the last output of the simulation, that is for the present-day $z = 0$ epoch, whereas a study of the evolution with redshift is matter of future studies.

The distribution in luminosity is analyzed with the IRAF packages and profiles are derived and fitted in order to recover the photometric and structural parameters; results are shown in Chapter 6 for the three simulations. As already said, the Sérsic law gives an idea of the shape of the intensity profile, with the index n indicating the overall shape of the profile.

The results found in Chapter 6 from the Fourier isophotal analysis of the artificial images and the Sérsic fit to the intensity profile, give different values for the effective radius and the Sérsic index when computed through different passbands of the SDSS photometric system. As mentioned, from observations results that measures of half-light angular sizes are larger in the bluer bands.

For the ΛCDM model, the simulated radii measured in the different filters, follow the trend found for the observable data (see e.g. SDSS Bernardi et al. (2003a)) with values of the radius of $3-4.3\ kpc$ on average and a Sérsic index of $3-4.4$, thus congruent with a de Vaucouleurs (1948) fit with index $n = 4$. For the *SCDM* model the trend radius-filter passband is not fairly followed, but only for the bluer bands, thus increasing again towards the reddest. Values of $\sim 6\ kpc$ are for all bands, with an index $n = 3-4.4$, again resembling a de Vaucouleurs (1948) profile of an elliptical galaxy. Congruent also with the fact that the galaxy has a greater mass

than the ΛCDM_{mp}, independently of differences in cosmological scenarios, hence must have a larger radius. The ΛCDM shows a shallower profile in the inner part, with a lower Sérsic index $n \sim 1.8 - 2.2$ and effective radius of $\sim 2 - 3\ kpc$. We always have to remember that the simulation for this model stopped before reaching present-day formation at $z = 0$, but we analyzed it anyway.

Other than the strctural parameters, from the analysis of the images we can derive radial profiles of the morphological paramters, for instance, we have shown the ellipticity, position angle radial profiles, along with the profile of the a_4 parameter that gives an idea of the deviation of isophotes from pure ellipses. Profiles show no particular trend with average values, except maybe for the a_4 parameter for the ΛCDM model that shows a boxy structure in the outer regions.

Moreover, from the intensity radial profiles in the different bands we can recover color profiles of the simulated images. What results from our findings is that there is evidence in our simulated galaxies in showing a bluer center with respect to the outer regions for two out of three models. We will try to give an explanation to this, a result that seems to disagree with what is found in observed elliptical galaxies.

Color Profiles and evolution in the rest-frame

From observations we know that ETGs are redder in the cores and become bluer toward the outer region. As we already mentioned in Chapter 6 this trend is not exactly reproduced in the simulated galaxies. We have shown from the color profiles derived that our models are slightly bluer than observational colors in the central parts. The interpretation of this discrepancy between our simulations and the data might be due to the ongoing star formation at older ages. In this sense, a physical process that stops star formation at earlier stages of the evolution might be needed to recover colors that resemble those of real galaxies. Even if it is likely, however, that such a tendency could be a result of metallicity gradients.

We considered, for instance, the *SCDM* model. From Figure 4.1 we can see from the star formation trend (see Figure 4.1) that a tail of stellar activity results from these simulations and a number of stars is continuously forming until $z = 0$.

By considering the stellar distribution of Figure 7.1 and assigning a color to each stellar particle in the simulated galaxy, in function of their age and metallicity, as described in Section 4.4, we derive the color evolution shown in Figure 7.2, which is simply the projection of Figure 4.8 along the xy-plane. The evolution in the $B-V$ color of the Bessell-Brett photometric system is roughly described, but at a first glance we can see how, as the galaxy ages, colors become redder but for the very central regions that remain bluer even in the last stages of the evolution.

We have quantitatively tested the code by stopping the star formation at earlier ages, in order

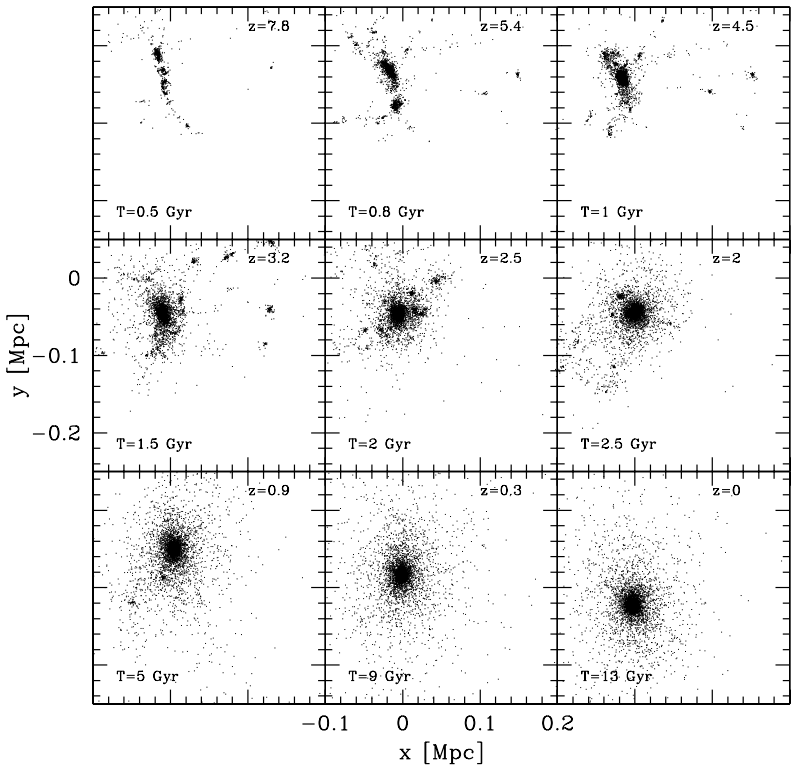

Figure 7.1: Rest-frame color evolution for the stellar distribution in the bidimensional plane for the *SCDM* model galaxy.

to see if an improvement of this kind in the simulation might be a solution to the problem. We have done this by stopping star formation by means of photometry. We assumed that recently formed stars younger than 2 $\times 10^9$ *yrs* are obscured and do not contribute to the total flux. By comparison we also considered the case in which stars younger than 3-4-5 $\times 10^9$ *yrs* are obscured, as shown in Figure 7.3. We see that the color recovered in these cases result in values of color $B-V$ slightly higher than the cases with complete star formation considered, thus giving similar values in all cases with redder in the $B-V$ color of the order of 0.1 *mag*.

Moreover, we also distinguished in regions confined within different raddi (see Figure 7.4), for the two particular cases of star formation stopped at 2 and 5 *Gyr* of the galaxy's evolution. Results of the color evolution are shown in Figures 7.5 and 7.6, where star formation is halted for particles born in the last 2 and 5 $\times 10^9$ *yrs* and enclosed into a given radius: within 50 *kpc*, that cover almost the entire region of the galaxy, 15 *kpc*, within the effective radius R_e and half

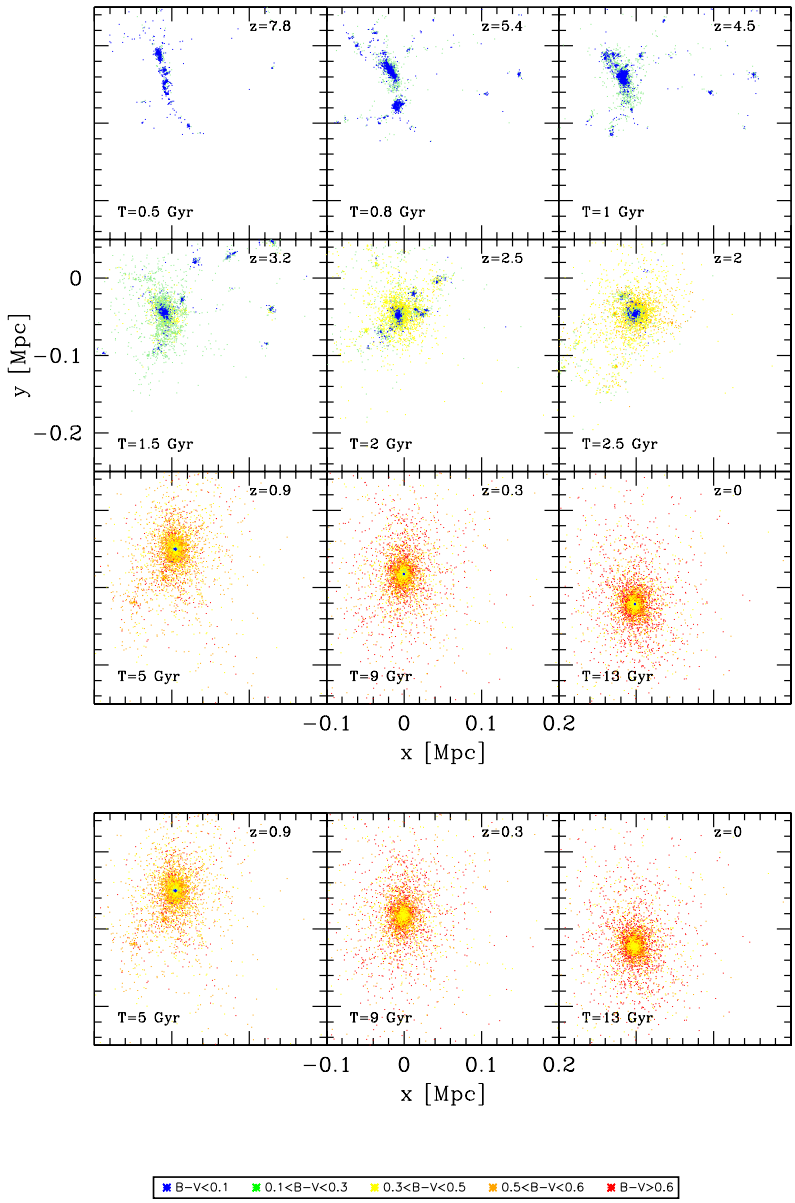

Figure 7.2: Rest-frame color evolution for the B-V color in the bidimensional plane for the *SCDM* model galaxy. In the upper panel is shown the galaxy with the entire star formation as shown in Figure 4.1 (upper left pane), in the lower section is shown the evolution with star formation that has been stopped at 5 Gyr, so that there is only passive evolution after this epoch.

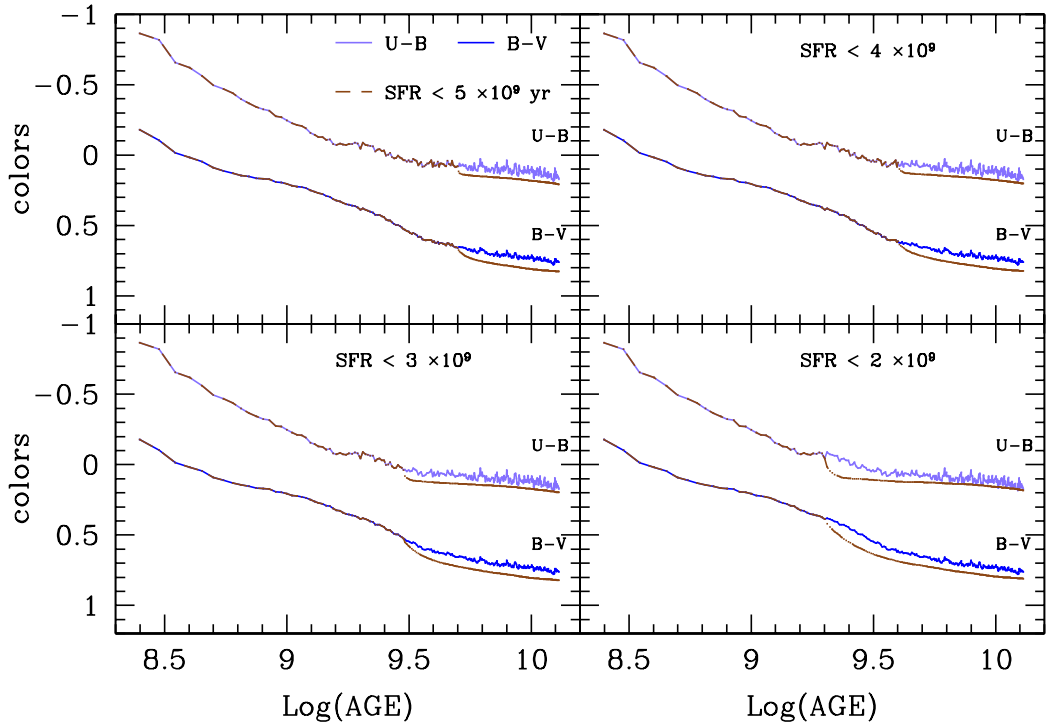

Figure 7.3: Rest-frame color evolution for the U-B and B-V Bessell-Brett photometric ssystem for the *SCDM* model. Comparison between models where SFR is halted at different ages.

of R_e, and for comparison is shown the trend when entire star formation is included. For both cases the difference in magnitudes recovered for the colors in their evolution is similar, thus depending on the radius inside which particles are considered. These trends show that going towards the central regions colors become redder if star formation is quenched at earlier stages of evolution, thus demonstrating that this effect refers to the central regions.

From Figure 7.2 follows that, as expected, if the contribution of the young stars was ignored, that is, if the SFR is halted in some way, the resulting colors would end up to be redder. This can be seen geometrically from the bottom panel of Figure 7.2, where the evolution of the last ages is plotted for comparison. We estimated a $B-V$ color difference of $0.1-0.2$ magnitudes in average. Considering this offset, if the contribution of the young stars was ignored, the resulting colors would agree better the observed data.

Thus, to bring the simulated *SCDM* model into closer agreement with observation, the treatment of the physical processes would require a major revision to the way in which star formation

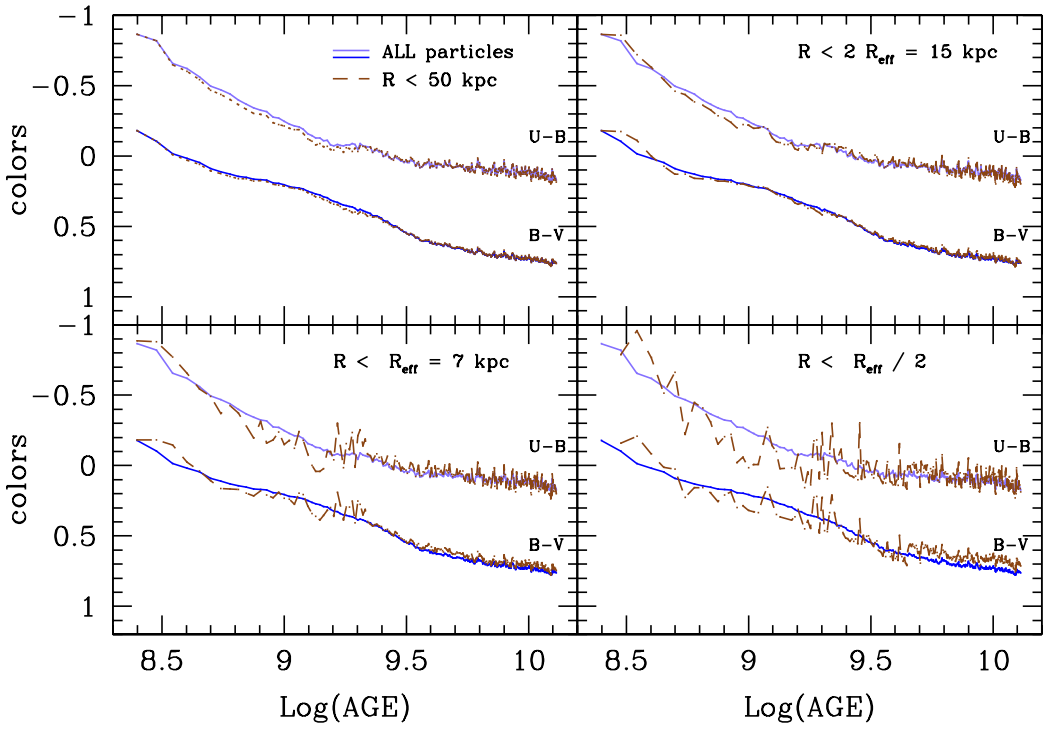

Figure 7.4: The same as Fgure 7.3. Comparison bewteen models at different radii.

and any other physical process (e.g. feedback) are modelled in the numerical code.

For the ΛCDM model, the color profiles are consistent with observations. This model has been simulated with the new recipe for the ISM, as described in Chapter 4; the star formation results more extended through the evolution with low SFR in the latter ages and woth lower values than the *SCDM* model at $z = 0$. However, more studies and on a larger number of simulation must be done to give a more detailed interpretation.

It seems clear from this discussion that shedding light on this issue will require further investigation of other star formation and feedback implementations, and a better resolution is certainly required to analyze and photometric properties in more detail in the central zones.

Scaling Laws

In Chapter 6 we presented the results we performed on the template galaxies in order to establish the consistency of our models with photometric constraints. We construced the Kormendy

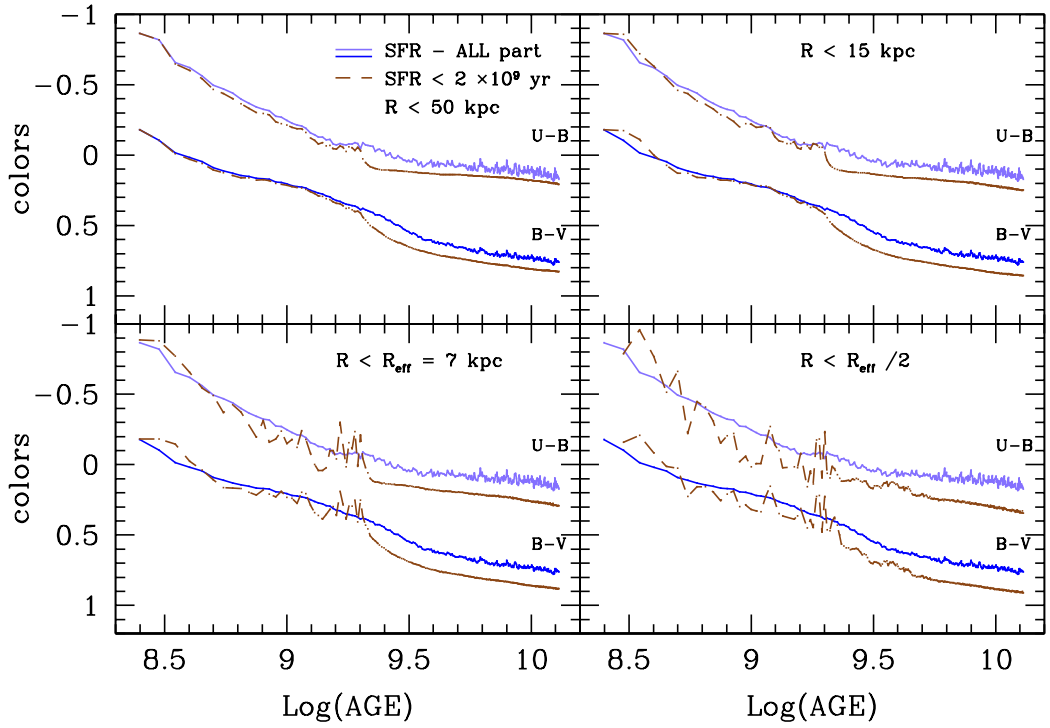

Figure 7.5: The same as Fgure 7.3. Comparison beween models where SFR is halted at for stars older than 2×10^9 and for different radii.

relation from data selected from the SDSS and overlapped our simulated data. In Figure 6.9 we see how two of the simulated galaxies, the *SCDM* and the ΛCDM_{mp} models lie next to the observational data, while the third model, the ΛCDM, clearly stands out from the rest. We have to keep in mind that in this case, due to computational problems, the simulation stopped earlier, and, as explained in Section 6.5, probably the galaxy would have reached a lower value of magnitude, as follows from the trend seen in the magnitude evolution, thus gaining the difference needed to reach values comparable to the observed ones.

In order to situate the simulated galaxy within the FP, we would need to estimate its central velocity dispersion, σ_0. This value is recovered within an aperture typically less than about half the effective radius. Unfortunately, velocities within such small radii in the simulated galaxy are significantly affected by the gravitational softening that in our case amounts to 1 kpc.

With a better resolution in future will be possible to recover this parameter and reprodce the FP, but, for the moment, computational capabilities don't enable us to undertake this study.

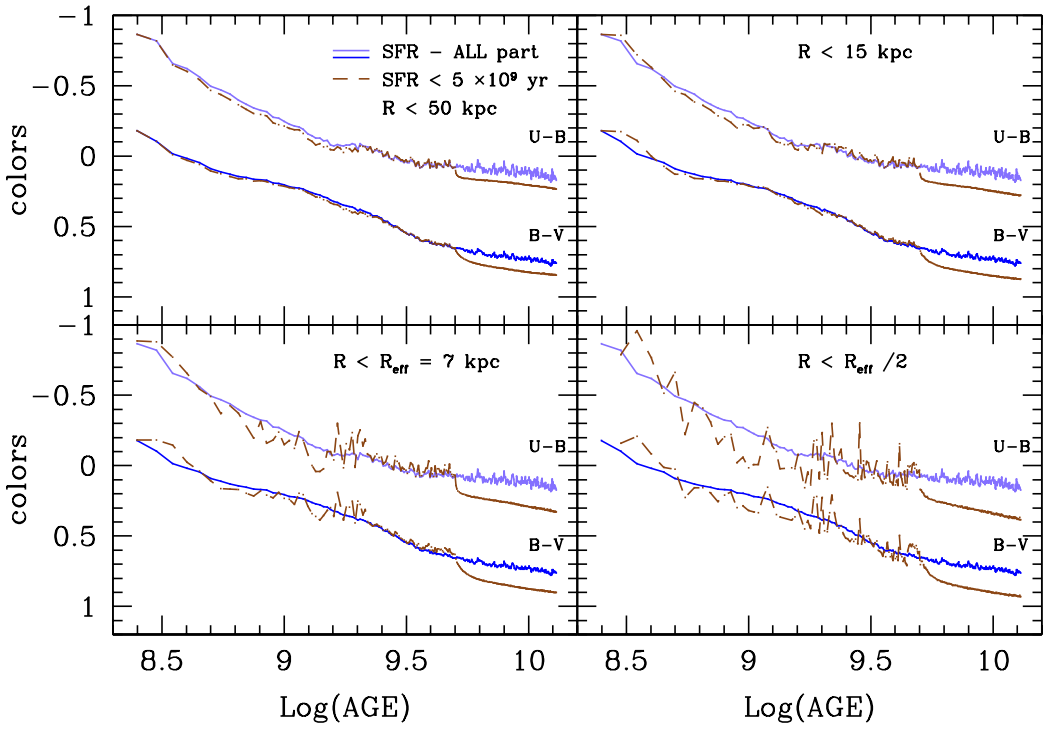

Figure 7.6: The same as Fgure 7.3. Comparison between models where SFR is halted at for stars older than 5×10^9 and for different radii.

Measuring the three parameters that enter the FP for ellipticals with the varying of redshift z emphasizes some important questions which bear on the age, formation history and internal properties of elliptical galaxies. It can answer questions such as how far in the past does the FP apply and if its parameters evolve significantly with time. A study of the galaxy properties as a function of look-back time provides a sensitive probe of the possible evolutionary differences. In this sense, we intend to continue the study of the empirical scaling laws at intermediate redshift by deriving the parameters that enter the relation not only at the present-day but also as function of time, by considering the evolution with redshift of the population of ETGs.

Dust

The present model does not consider the effects of dust extinction on the integrated SEDs of galaxies. In order to incorporate gaseous emission into our model, we need to combine the

N-body simulation code with both our adopted photometric tool by considering the gaseous component of the structures (Piovan et al. 2006a; Piovan et al. 2006b). For instance, the next step will be to include SSPs built with dust (Piovan et al. 2003), this is task that needs to be taken into account and will be added in future studies.

Summary and Conclusions

This work is part of a larger project which is aimed to constrain the dominant mechanism for the formation and evolution of ETGs. The combination of the photometric code with the cosmological chemo-dynamical simulations make it possible to undertake quantitative comparisons between the theoretical models of ETGs and the observational data in any spectral regime.

The principles of synthetic photometry for the theoretical stellar energy distributions and passbands of the photometric systems are discussed. The equations utilized in the algorithm to compute the magnitudes and colors are also provided. A main positive characteristic of the code is the flexibility in the way input libraries (evolutionary tracks, stellar atmospheres) and functions (initial mass function, star formation rate, metallicity) can be changed, tested, and added to the database for future use.

We have so far analyzed three test models of elliptical galaxies in the following photometric systems: Bessell-Brett, SDSS, COSMOS and GOODS filters among all the ones we have at dipsosal, and the code is ready to be implemented with any photometric system; moreover, any broadband VEGA, AB, ST magnitude system can be considered as well.

Our main results may be summarized as follows:

Starting from the evolutionary synthesis results we compute the evolutionary and cosmological corrections, along with magnitudes and colors and their evolution at different redshifts for the simulated galaxies at our disposal. We consider the COSMOS and the GOODS databases, which allow us to select a sample of galaxies that are catalogued as early-type and to make a qualitative and quantitative comparison between the theoretical results obtained from our model galaxies and the observational data. For both datasets our findings show that simulated colors for the different cosmological scenarios follow the general trend at lower redshifts and are in good agreement with the data up to $z \sim 1$, where the number of early-type galaxies observed falls abruptly. In conclusion, within the redshift range considered, all the simulated colors reproduce quite well the observational data.

By matching the population synthesis models with the three-dimensional geometric information of the galaxy's structure along with the chemical details, both provided by the N-body simulations, we create synthetic images of a galaxy in a given photometric system, from which we derive the structural and morphological parameters, as the galaxy's effective radius and the luminosity within this, the shape indices through Fourier and Sérsic analysis, color profiles, and radial profiles of most of the parameters that define the structure of galaxies.

The luminosity profiles of the galaxy at $z = 0$ can be reasonably fitted with an $R^{1/n}$ law. The effective radius of the simulated galaxy are recovered for the three model galaxies and in the different photometric bands adopted by the SDSS. Isophotes are well approximated by ellipses, with only a weak radial variation in position angle and ellipticity. Small but significant deviations from perfect ellipses are also measured; the simulated galaxy appears 'boxy' for one of the template galaxies.

The most interesting aspect of these results is that the investigation of the simulated galaxies, via the photometric analysis of the artificial images, lead us to recover properties that resemble those of observed galaxies. The results obtained in this way are studied and compared within the scaling laws, the Kormendy relation in particular, as it is the only one we can construct so far, due to the limited resolution of our simulations. The observational data with which we compare our simulated results have been selected form the SDSS database. We separate a subsample of elliptical galaxies, and our findings show that the values of luminosities and effective radii, the two parameters that compare in the Kormendy relation, measured for our model galaxies are consistent with the archivial data from the SDSS.

The application of this tool to the simulated galaxies at our disposal allows to understand that the method, still at its infancy, provides good results that permit a comparison between the numerical models and the observational data.

Even if a small sample of simulated galaxies does not allow for a statistical generalization and we have to attend a more complete library of simulated galaxies that, e.g., evolve in the same cosmological scenario, cover a wider range in mass, etc., the main result of this thesis consists in the fact that the method developed to follow the spectro-photometric evolution of galaxies stands up.

As our simulated sample grows, we expect to be able to elucidate better the trends and to provide insight into the meaning of the correlations (or lack thereof) between shape, kinematics, and photometry within the hierarchical merger model for the formation of elliptical galaxies.

Appendix A

Initial Mass Functions

SSPs from GALADRIEL database[1] are calculated by Tantalo (2005) for six different prescriptions for the IMF: four power-laws (Salpeter 1955, Kennicutt 1983, Kroupa 1998, Arimoto & Yoshii 1987) and three exponential-laws (Larson 1998, for solar neighbourhood and steeper, and Chabrier 2001).

In the following we list the most common laws and will indicate the stellar mass M in solar units. Values of mass range for the different IMF are listed in Table A.1, where M_{SSP} is the integrated mass of a SSP.

(1) A Salpeter (1955) IMF, extended over the typical stellar mass–range [0.1–100] $M_{\odot}$:

$$\Phi(M) = C_s M^{-1.35} \qquad C_s = 0.1716$$

where C_s is a normalization coefficient fixed so that the IMF is normalized to unit mass when integrated between the low and high stellar mass ends.

(2) The Kroupa (1998) IMF, derived for field stars in the Solar Neighbourhood and often adopted in chemical evolution models for disc galaxies (e.g. Boissier & Prantzos 1999):

$$\Phi(M) = \begin{cases} C_{kr1} M^{-0.5} & 0.1 < M < 0.5 \\ C_{kr} M^{-1.2} & 0.5 < M < 1 \\ C_{kr} M^{-1.7} & 1 < M < 100 \end{cases}$$

$$C_{kr1} = 0.480 \qquad C_{kr} = 0.295$$

[1] available online from the Padova Galaxies and Single Stellar Population Models (GALADRIEL) at *http://www.astro.unipd.it/galadriel/*

where C_{kr1} and C_{kr} are fixed so as to guarantee normalization and continuity of the IMF over the range [0.1–100] $M_{\odot}$.

(3) The Kennicutt (1983) IMF, often advocated as adequate to reproduce the global properties of spiral galaxies (e.g. KTC94, Sommer-Larsen 1996), again with the typical mass range [0.1–100] $M_{\odot}$.

$$\Phi(M) = \begin{cases} C_{k83}\, M^{-0.4} & 0.1 < M < 1 \\ C_{k83}\, M^{-1.5} & 1 < M < 100 \end{cases}$$

$$C_{k83} = 0.328$$

(1) The Arimoto & Yoshii (1987) IMF, extended over the typical stellar mass–range [0.1–100] $M_{\odot}$:

$$\Phi(M) = C_A\, M^{-1.} \qquad C_A = 0.14476$$

where C_A is a normalization coefficient fixed so that the IMF is normalized to unit mass when integrated between the low and high stellar mass ends.

(5) The Larson (1998) IMF, over the mass range [0.01–100] $M_{\odot}$, that is down to the sub-stellar regime (which in this case has, however, a negligible contribution to the mass budget):

$$\Phi(M) = C_{L1}\, M^{-1.35}\, exp\left(-\frac{M_{L1}}{M}\right)$$

$$C_{L1} = 0.317 \qquad M_{L1} = 0.3375$$

(6) A modified Larson IMF:

$$\Phi(M) = C_{L2}\, M^{-1.7}\, exp\left(-\frac{M_{L2}}{M}\right)$$

$$C_{L2} = 0.4337 \qquad M_{L2} = 0.425$$

(7) The IMF suggested by Chabrier (2001, his case IMF3):

$$\Phi(M) = C_C\, M^{-2.3}\, exp\left[-\left(\frac{M_C}{M}\right)^{0.25}\right]$$

$$C_C = 40.33 \qquad M_C = 716.4$$

over the mass range [0.01–100] $M_{\odot}$.

Table A.1: Masses for the considered IMF's

IMF	$M_l(M_\odot)$	$M_u(M_\odot)$	$M_{SSP}(M_\odot)$
Salpeter	0.1	100	5.826
Kennicutt	0.1	100	3.048
Kroupa	0.1	100	3.385
Arimoto & Yoshii	0.1	100	6.908
Larson (1)	0.01	100	3.154
Larson (2)	0.01	100	2.719
Chabrier	0.01	100	0.025

References

Abazajian, K., J. K. Adelman-McCarthy, M. A. Agüeros, S. S. Allam, K. Anderson, S. F. Anderson, J. Annis, N. A. Bahcall, I. K. Baldry, S. Bastian, A. Berlind, M. Bernardi, M. R. Blanton, J. J. Bochanski, Jr., W. N. Boroski, J. W. Briggs, J. Brinkmann, R. J. Brunner, T. Budavári, L. N. Carey, S. Carliles, F. J. Castander, A. J. Connolly, I. Csabai, M. Doi, F. Dong, D. J. Eisenstein, M. L. Evans, X. Fan, D. P. Finkbeiner, S. D. Friedman, J. A. Frieman, M. Fukugita, R. R. Gal, B. Gillespie, K. Glazebrook, J. Gray, E. K. Grebel, J. E. Gunn, V. K. Gurbani, P. B. Hall, M. Hamabe, F. H. Harris, H. C. Harris, M. Harvanek, T. M. Heckman, J. S. Hendry, G. S. Hennessy, R. B. Hindsley, C. J. Hogan, D. W. Hogg, D. J. Holmgren, S.-i. Ichikawa, T. Ichikawa, Ž. Ivezić, S. Jester, D. E. Johnston, A. M. Jorgensen, S. M. Kent, S. J. Kleinman, G. R. Knapp, A. Y. Kniazev, R. G. Kron, J. Krzesinski, P. Z. Kunszt, N. Kuropatkin, D. Q. Lamb, H. Lampeitl, B. C. Lee, R. F. Leger, N. Li, H. Lin, Y.-S. Loh, D. C. Long, J. Loveday, R. H. Lupton, T. Malik, B. Margon, T. Matsubara, P. M. McGehee, T. A. McKay, A. Meiksin, J. A. Munn, R. Nakajima, T. Nash, E. H. Neilsen, Jr., H. J. Newberg, P. R. Newman, R. C. Nichol, T. Nicinski, M. Nieto-Santisteban, A. Nitta, S. Okamura, W. O'Mullane, J. P. Ostriker, R. Owen, N. Padmanabhan, J. Peoples, J. R. Pier, A. C. Pope, T. R. Quinn, G. T. Richards, M. W. Richmond, H.-W. Rix, C. M. Rockosi, D. J. Schlegel, D. P. Schneider, R. Scranton, M. Sekiguchi, U. Seljak, G. Sergey, B. Sesar, E. Sheldon, K. Shimasaku, W. A. Siegmund, N. M. Silvestri, J. A. Smith, V. Smolčić, S. A. Snedden, A. Stebbins, C. Stoughton, M. A. Strauss, M. SubbaRao, A. S. Szalay, I. Szapudi, P. Szkody, G. P. Szokoly, M. Tegmark, L. Teodoro, A. R. Thakar, C. Tremonti, D. L. Tucker, A. Uomoto, D. E. Vanden Berk, J. Vandenberg, M. S. Vogeley, W. Voges, N. P. Vogt, L. M. Walkowicz, S.-i. Wang, D. H. Weinberg, A. A. West, S. D. M. White, B. C. Wilhite, Y. Xu, B. Yanny, N. Yasuda, C.-W. Yip, D. R. Yocum, D. G. York, I. Zehavi, S. Zibetti, & D. B. Zucker (2004, July). The Second Data Release of the Sloan Digital Sky Survey. *AJ 128*, 502–512.

Alexander, D. R. & J. W. Ferguson (1994, December). Low-temperature Rosseland opacities. *ApJ 437*, 879–891.

Allard, F., P. H. Hauschildt, D. R. Alexander, J. W. Ferguson, & A. Tamanai (2000). Model Atmospheres and Spectra of Brown Dwarfs to Giant Planets. In C. A. Griffith & M. S. Marley (Eds.), *From Giant Planets to Cool Stars*, Volume 212 of *Astronomical Society of the Pacific Conference Series*, pp. 127–+.

Alongi, M., G. Bertelli, A. Bressan, & C. Chiosi (1991, April). Effects of envelope overshoot on stellar models. *A&A 244*, 95–106.

Alongi, M., G. Bertelli, A. Bressan, C. Chiosi, F. Fagotto, L. Greggio, & E. Nasi (1993, March). Evolutionary sequences of stellar models with semiconvection and convective overshoot. I - Z = 0.008. *A&AS 97*, 851–871.

Aragon-Salamanca, A., R. S. Ellis, W. J. Couch, & D. Carter (1993, June). Evidence for systematic evolution in the properties of galaxies in distant clusters. *MNRAS 262*, 764–794.

Arimoto, N. & Y. Yoshii (1987, February). Chemical and photometric properties of a galactic wind model for elliptical galaxies. *A&A 173*, 23–38.

Aune, S., O. Boulade, X. Charlot, P. Abbon, P. Borgeaud, P.-H. Carton, M. Carty, J. Da Costa, D. Desforge,

H. Deschamps, D. Eppellé, P. Gallais, L. Gosset, R. Granelli, M. Gros, J. de Kat, D. Loiseau, J. L. Ritou, J. Y. Roussé, P. Starzynski, N. Vignal, & L. G. Vigroux (2003, March). The CFHT MegaCam 40 CCDs camera: cryogenic design and CCD integration. In M. Iye & A. F. M. Moorwood (Eds.), *Instrument Design and Performance for Optical/Infrared Ground-based Telescopes. Edited by Iye, Masanori; Moorwood, Alan F. M. Proceedings of the SPIE, Volume 4841, pp. 513-524 (2003).*, Volume 4841 of *Presented at the Society of Photo-Optical Instrumentation Engineers (SPIE) Conference*, pp. 513–524.

Bahcall, J. N., M. H. Pinsonneault, & G. J. Wasserburg (1995, October). Solar models with helium and heavy-element diffusion. *Reviews of Modern Physics 67*, 781–808.

Barger, A. J., L. L. Cowie, I. Smail, R. J. Ivison, A. W. Blain, & J.-P. Kneib (1999, June). Redshift Distribution of the Faint Submillimeter Galaxy Population. *AJ 117*, 2656–2665.

Barnes, J. & P. Hut (1986, December). A Hierarchical O(NlogN) Force-Calculation Algorithm. *Nature 324*, 446–449.

Barnes, J. E. & L. Hernquist (1996, November). Transformations of Galaxies. II. Gasdynamics in Merging Disk Galaxies. *ApJ 471*, 115–+.

Bekki, K., W. J. Couch, Y. Shioya, & A. Vazdekis (2005, May). Origin of E+A galaxies - I. Physical properties of E+A galaxies formed from galaxy merging and interaction. *MNRAS 359*, 949–965.

Bell, E. F., C. Wolf, K. Meisenheimer, H.-W. Rix, A. Borch, S. Dye, M. Kleinheinrich, L. Wisotzki, & D. H. McIntosh (2004, June). Nearly 5000 Distant Early-Type Galaxies in COMBO-17: A Red Sequence and Its Evolution since z˜1. *ApJ 608*, 752–767.

Bender, R. (1988, March). Velocity anisotropies and isophote shapes in elliptical galaxies. *A&A 193*, L7–L10.

Bender, R. (1997). Structure; Formation and Ages of Elliptical Galaxies. In M. Arnaboldi, G. S. Da Costa, & P. Saha (Eds.), *The Nature of Elliptical Galaxies; 2nd Stromlo Symposium*, Volume 116 of *Astronomical Society of the Pacific Conference Series*, pp. 11–+.

Bender, R. & J.-L. Nieto (1990, November). Internal kinematics of low-luminosity ellipsoidal galaxies. *A&A 239*, 97–112.

Bender, R., R. P. Saglia, B. Ziegler, P. Belloni, L. Greggio, U. Hopp, & G. Bruzual (1998, January). Exploring Cluster Elliptical Galaxies as Cosmological Standard Rods. *ApJ 493*, 529–+.

Bender, R., B. Ziegler, & G. Bruzual (1996, June). The Redshift Evolution of the Stellar Populations in Elliptical Galaxies. *ApJ 463*, L51–L54.

Benítez, N. (2000, June). Bayesian Photometric Redshift Estimation. *ApJ 536*, 571–583.

Benz, W. (1990). Smooth Particle Hydrodynamics - a Review. In J. R. Buchler (Ed.), *Numerical Modelling of Nonlinear Stellar Pulsations Problems and Prospects*, pp. 269–+.

Bernardi, M., R. K. Sheth, J. Annis, S. Burles, D. J. Eisenstein, D. P. Finkbeiner, D. W. Hogg, R. H. Lupton, D. J. Schlegel, M. SubbaRao, N. A. Bahcall, J. P. Blakeslee, J. Brinkmann, F. J. Castander, A. J. Connolly, I. Csabai, M. Doi, M. Fukugita, J. Frieman, T. Heckman, G. S. Hennessy, Ž. Ivezić, G. R. Knapp, D. Q. Lamb, T. McKay, J. A. Munn, R. Nichol, S. Okamura, D. P. Schneider, A. R. Thakar, & D. G. York (2003a, April). Early-Type Galaxies in the Sloan Digital Sky Survey. III. The Fundamental Plane. *AJ 125*, 1866–1881.

Bernardi, M., R. K. Sheth, J. Annis, S. Burles, D. J. Eisenstein, D. P. Finkbeiner, D. W. Hogg, R. H. Lupton, D. J. Schlegel, M. SubbaRao, N. A. Bahcall, J. P. Blakeslee, J. Brinkmann, F. J. Castander, A. J. Connolly, I. Csabai, M. Doi, M. Fukugita, J. Frieman, T. Heckman, G. S. Hennessy, Ž. Ivezić, G. R. Knapp, D. Q. Lamb, T. McKay, J. A. Munn, R. Nichol, S. Okamura, D. P. Schneider, A. R. Thakar, & D. G. York (2003b, April). Early-type Galaxies in the Sloan Digital Sky Survey. II. Correlations between Observables. *AJ 125*, 1849–1865.

Bernardi, M., R. K. Sheth, J. Annis, S. Burles, D. J. Eisenstein, D. P. Finkbeiner, D. W. Hogg, R. H. Lupton, D. J. Schlegel, M. SubbaRao, N. A. Bahcall, J. P. Blakeslee, J. Brinkmann, F. J. Castander, A. J. Connolly, I. Csabai, M. Doi, M. Fukugita, J. Frieman, T. Heckman, G. S. Hennessy, Ž. Ivezić, G. R. Knapp, D. Q. Lamb, T. McKay, J. A. Munn, R. Nichol, S. Okamura, D. P. Schneider, A. R. Thakar, & D. G. York (2003c, April). Early-Type Galaxies in the Sloan Digital Sky Survey. I. The Sample. *AJ 125*, 1817–1848.

Bernardi, M., R. K. Sheth, J. Annis, S. Burles, D. P. Finkbeiner, R. H. Lupton, D. J. Schlegel, M. SubbaRao, N. A. Bahcall, J. P. Blakeslee, J. Brinkmann, F. J. Castander, A. J. Connolly, I. Csabai, M. Doi, M. Fukugita, J. Frieman, T. Heckman, G. S. Hennessy, Ž. Ivezić, G. R. Knapp, D. Q. Lamb, T. McKay, J. A. Munn, R. Nichol, S. Okamura, D. P. Schneider, A. R. Thakar, & D. G. York (2003, April). Early-Type Galaxies in the Sloan Digital Sky Survey. IV. Colors and Chemical Evolution. *AJ 125*, 1882–1896.

Bertelli, G., A. Bressan, C. Chiosi, F. Fagotto, & E. Nasi (1994, August). Theoretical isochrones from models with new radiative opacities. *A&AS 106*, 275–302.

Bertin, E. & S. Arnouts (1996, June). SExtractor: Software for source extraction. *A&AS 117*, 393–404.

Bessell, M. S. (1990, October). UBVRI passbands. *PASP 102*, 1181–1199.

Bessell, M. S. & J. M. Brett (1988, September). JHKLM photometry - Standard systems, passbands, and intrinsic colors. *PASP 100*, 1134–1151.

Bessell, M. S., F. Castelli, & B. Plez (1998, May). Model atmospheres broad-band colors, bolometric corrections and temperature calibrations for O - M stars. *A&A 333*, 231–250.

Böhm-Vitense, E. (1958). Über die Wasserstoffkonvektionszone in Sternen verschiedener Effektivtemperaturen und Leuchtkräfte. Mit 5 Textabbildungen. *Zeitschrift fur Astrophysik 46*, 108–+.

Boulade, O., X. Charlot, P. Abbon, S. Aune, P. Borgeaud, P.-H. Carton, M. Carty, J. Da Costa, H. Deschamps, D. Desforge, D. Eppellé, P. Gallais, L. Gosset, R. Granelli, M. Gros, J. de Kat, D. Loiseau, J.-. Ritou, J. Y. Roussé, P. Starzynski, N. Vignal, & L. G. Vigroux (2003, March). MegaCam: the new Canada-France-Hawaii Telescope wide-field imaging camera. In M. Iye & A. F. M. Moorwood (Eds.), *Instrument Design and Performance for Optical/Infrared Ground-based Telescopes. Edited by Iye, Masanori; Moorwood, Alan F. M. Proceedings of the SPIE, Volume 4841, pp. 72-81 (2003).*, Volume 4841 of *Presented at the Society of Photo-Optical Instrumentation Engineers (SPIE) Conference*, pp. 72–81.

Bower, R. G., J. R. Lucey, & R. S. Ellis (1992, February). Precision photometry of early-type galaxies in the Coma and Virgo clusters: A test of the universality of the colour-magnitude relation. I - The data. II. Analysis. *MNRAS 254*, 589–613.

Bressan, A., C. Chiosi, & F. Fagotto (1994, August). Spectrophotometric evolution of elliptical galaxies. 1: Ultraviolet excess and color-magnitude-redshift relations. *ApJS 94*, 63–115.

Bressan, A., C. Chiosi, & R. Tantalo (1996, July). Probing the age of elliptical galaxies. *A&A 311*, 425–445.

Bressan, A., F. Fagotto, G. Bertelli, & C. Chiosi (1993, September). Evolutionary sequences of stellar models with new radiative opacities. II - Z = 0.02. *A&AS 100*, 647–664.

Bressan, A. G., C. Chiosi, & G. Bertelli (1981, September). Mass loss and overshooting in massive stars. *A&A 102*, 25–30.

Brinchmann, J. & R. S. Ellis (2000, June). The Mass Assembly and Star Formation Characteristics of Field Galaxies of Known Morphology. *ApJ 536*, L77–L80.

Bruzual, G. & S. Charlot (1993, March). Spectral evolution of stellar populations using isochrone synthesis. *ApJ 405*, 538–553.

Bruzual, G. & S. Charlot (2003, October). Stellar population synthesis at the resolution of 2003. *MNRAS 344*, 1000–1028.

Bruzual A., G. (1983, October). Spectral evolution of galaxies. I - Early-type systems. *ApJ 273*, 105–127.

Bruzual A., G. (1992). Evolutionary Population Synthesis. In B. Barbuy & A. Renzini (Eds.), *The Stellar Populations of Galaxies*, Volume 149 of *IAU Symposium*, pp. 311–+.

Bundy, K., R. S. Ellis, & C. J. Conselice (2005, June). The Mass Assembly Histories of Galaxies of Various Morphologies in the GOODS Fields. *ApJ 625*, 621–632.

Butcher, H. & A. Oemler, Jr. (1978, January). The evolution of galaxies in clusters. I - ISIT photometry of C1 0024+1654 and 3C 295. *ApJ 219*, 18–30.

Capak, P., H. Aussel, M. Ajiki, H. J. McCracken, B. Mobasher, N. Scoville, P. Shopbell, Y. Taniguchi, D. Thompson, S. Tribiano, S. Sasaki, A. W. Blain, M. Brusa, C. Carilli, A. Comastri, C. M. Carollo, P. Cassata, J. Colbert, R. S. Ellis, M. Elvis, M. Giavalisco, W. Green, L. Guzzo, G. Hasinger, O. Ilbert, C. Impey, K. Jahnke, J. Kartaltepe, J.-P. Kneib, J. Koda, A. Koekemoer, Y. Komiyama, A. Leauthaud, O. Lefevre, S. Lilly, C. Liu, R. Massey, S. Miyazaki, T. Murayama, T. Nagao, J. A. Peacock, A. Pickles, C. Porciani, A. Renzini, J. Rhodes, M. Rich, M. Salvato, D. B. Sanders, C. Scarlata, D. Schiminovich, E. Schinnerer, M. Scodeggio, K. Sheth, Y. Shioya, L. A. M. Tasca, J. E. Taylor, L. Yan, & G. Zamorani (2007, September). The First Release COSMOS Optical and Near-IR Data and Catalog. *ApJS 172*, 99–116.

Cardelli, J. A., G. C. Clayton, & J. S. Mathis (1989, October). The relationship between infrared, optical, and ultraviolet extinction. *ApJ 345*, 245–256.

Carraro, G., C. Lia, & C. Chiosi (1998, July). Galaxy formation and evolution - I. The Padua tree-sph code (pd-sph). *MNRAS 297*, 1021–1040.

Castelli, F. (1999, June). Synthetic photometry from ATLAS9 models in the UBV Johnson system. *A&A 346*, 564–585.

Castelli, F., R. G. Gratton, & R. L. Kurucz (1997, February). Notes on the convection in the ATLAS9 model atmospheres. *A&A 318*, 841–869.

Castelli, F. & R. L. Kurucz (1994, January). Model atmospheres for VEGA. *A&A 281*, 817–832.

Caughlan, G. R. & W. A. Fowler (1988). Thermonuclear Reaction Rates V. *Atomic Data and Nuclear Data Tables 40*, 283–+.

Chabrier, G. (2001, June). The Galactic Disk Mass Budget. I. Stellar Mass Function and Density. *ApJ 554*, 1274–1281.

Charlot, S., G. Worthey, & A. Bressan (1996, February). Uncertainties in the Modeling of Old Stellar Populations. *ApJ 457*, 625–+.

Chiosi, C. (2000, December). Gas and iron content of galaxy clusters. *A&A 364*, 423–442.

Chiosi, C., G. Bertelli, & A. Bressan (1992). New developments in understanding the HR diagram. *ARA&A 30*, 235–285.

Chiosi, C. & G. Carraro (2002, September). Formation and evolution of elliptical galaxies. *MNRAS 335*, 335–357.

Davies, R. L., G. Efstathiou, S. M. Fall, G. Illingworth, & P. L. Schechter (1983, March). The kinematic properties of faint elliptical galaxies. *ApJ 266*, 41–57.

de Jager, C., H. Nieuwenhuijzen, & K. A. van der Hucht (1988, February). Mass loss rates in the Hertzsprung-Russell diagram. *A&AS 72*, 259–289.

de Vaucouleurs, G. (1948, January). Recherches sur les Nebuleuses Extragalactiques. *Annales d'Astrophysique 11*, 247–+.

Djorgovski, S. & M. Davis (1987, February). Fundamental properties of elliptical galaxies. *ApJ 313*, 59–68.

Draine, B. T. & H. M. Lee (1984, October). Optical properties of interstellar graphite and silicate grains. *ApJ 285*, 89–108.

Dressler, A. (1980, March). Galaxy morphology in rich clusters - Implications for the formation and evolution of galaxies. *ApJ 236*, 351–365.

Dressler, A., D. Lynden-Bell, D. Burstein, R. L. Davies, S. M. Faber, R. Terlevich, & G. Wegner (1987, February). Spectroscopy and photometry of elliptical galaxies. I - A new distance estimator. *ApJ 313*, 42–58.

Eggen, O. J., D. Lynden-Bell, & A. R. Sandage (1962, November). Evidence from the motions of old stars that the Galaxy collapsed. *ApJ 136*, 748–+.

Ellis, R. S., I. Smail, A. Dressler, W. J. Couch, A. J. Oemler, H. Butcher, & R. M. Sharples (1997, July). The Homogeneity of Spheroidal Populations in Distant Clusters. *ApJ 483*, 582–+.

Elston, R. (1998, August). FLAMINGOS: a multiobject near-IR spectrometer. In A. M. Fowler (Ed.), *Proc. SPIE Vol. 3354, p. 404-413, Infrared Astronomical Instrumentation, Albert M. Fowler; Ed.*, Volume 3354 of *Presented at the Society of Photo-Optical Instrumentation Engineers (SPIE) Conference*, pp. 404–413.

Faber, S. M. (1972, September). Quadratic programming applied to the problem of galaxy population synthesis. *A&A 20*, 361–374.

Faber, S. M., A. Dressler, R. L. Davies, D. Burstein, & D. Lynden-Bell (1987). Global scaling relations for elliptical galaxies and implications for formation. In S. M. Faber (Ed.), *Nearly Normal Galaxies. From the Planck Time to the Present*, pp. 175–183.

Faber, S. M. & R. E. Jackson (1976, March). Velocity dispersions and mass-to-light ratios for elliptical galaxies. *ApJ 204*, 668–683.

Fagotto, F., A. Bressan, G. Bertelli, & C. Chiosi (1994a, April). Evolutionary sequences of stellar models with new radiative opacities. III. Z=0.0004 and Z=0.05. *A&AS 104*, 365–376.

Fagotto, F., A. Bressan, G. Bertelli, & C. Chiosi (1994b, May). Evolutionary sequences of stellar models with new radiative opacities. IV. Z=0.004 and Z=0.008. *A&AS 105*, 29–38.

Fagotto, F., A. Bressan, G. Bertelli, & C. Chiosi (1994c, May). Evolutionary sequences of stellar models with very high metallicity. V. Z=0.1. *A&AS 105*, 39–45.

Fanelli, M. N., R. W. O'Connell, & T. X. Thuan (1987, October). Spectral synthesis in the ultraviolet. I - Far-ultraviolet stellar library. *ApJ 321*, 768–779.

Fanelli, M. N., R. W. O'Connell, & T. X. Thuan (1988, November). Spectral synthesis in the ultraviolet. II - Stellar populations and star formation in blue compact galaxies. *ApJ 334*, 665–687.

Ferrini, F. & B. M. Poggianti (1993, June). Evolution of elliptical galaxies. I - The multiphase model. *ApJ 410*, 44–55.

Fluks, M. A., B. Plez, P. S. The, D. de Winter, B. E. Westerlund, & H. C. Steenman (1994, June). On the spectra and photometry of M-giant stars. *A&AS 105*, 311–336.

Franx, M. (1995). Measuring the Evolution of the M/L Ratio from the Fundamental Plane. In P. C. van der Kruit & G. Gilmore (Eds.), *Stellar Populations*, Volume 164 of *IAU Symposium*, pp. 269–+.

Fukugita, M., C. J. Hogan, & P. J. E. Peebles (1998, August). The Cosmic Baryon Budget. *ApJ 503*, 518–+.

Fukugita, M., T. Ichikawa, J. E. Gunn, M. Doi, K. Shimasaku, & D. P. Schneider (1996, April). The Sloan Digital Sky Survey Photometric System. *AJ 111*, 1748–+.

Giavalisco, M., H. C. Ferguson, A. M. Koekemoer, M. Dickinson, D. M. Alexander, F. E. Bauer, J. Bergeron, C. Biagetti, W. N. Brandt, S. Casertano, C. Cesarsky, E. Chatzichristou, C. Conselice, S. Cristiani, L. Da Costa, T. Dahlen, D. de Mello, P. Eisenhardt, T. Erben, S. M. Fall, C. Fassnacht, R. Fosbury, A. Fruchter, J. P. Gardner, N. Grogin, R. N. Hook, A. E. Hornschemeier, R. Idzi, S. Jogee, C. Kretchmer, V. Laidler, K. S. Lee, M. Livio, R. Lucas, P. Madau, B. Mobasher, L. A. Moustakas, M. Nonino, P. Padovani, C. Papovich, Y. Park, S. Ravindranath, A. Renzini, M. Richardson, A. Riess, P. Rosati, M. Schirmer, E. Schreier, R. S. Somerville,

H. Spinrad, D. Stern, M. Stiavelli, L. Strolger, C. M. Urry, B. Vandame, R. Williams, & C. Wolf (2004, January). The Great Observatories Origins Deep Survey: Initial Results from Optical and Near-Infrared Imaging. *ApJ 600*, L93–L98.

Gibson, B. K. & F. Matteucci (1997, January). On Dwarf Galaxies as the Source of Intracluster Gas. *ApJ 475*, 47–+.

Girardi, L., G. Bertelli, A. Bressan, C. Chiosi, M. A. T. Groenewegen, P. Marigo, B. Salasnich, & A. Weiss (2002, August). Theoretical isochrones in several photometric systems. I. Johnson-Cousins-Glass, HST/WFPC2, HST/NICMOS, Washington, and ESO Imaging Survey filter sets. *A&A 391*, 195–212.

Girardi, L., A. Bressan, G. Bertelli, & C. Chiosi (2000, February). Evolutionary tracks and isochrones for low- and intermediate-mass stars: From 0.15 to 7 M_{sun}, and from Z=0.0004 to 0.03. *A&AS 141*, 371–383.

Girardi, L., E. K. Grebel, M. Odenkirchen, & C. Chiosi (2004, July). Theoretical isochrones in several photometric systems. II. The Sloan Digital Sky Survey ugriz system. *A&A 422*, 205–215.

Grazian, A., A. Fontana, C. de Santis, M. Nonino, S. Salimbeni, E. Giallongo, S. Cristiani, S. Gallozzi, & E. Vanzella (2006, April). The GOODS-MUSIC sample: a multicolour catalog of near-IR selected galaxies in the GOODS-South field. *A&A 449*, 951–968.

Grevesse, N. & A. Noels (1993). Atomic data and the spectrum of the solar photosphere. *Physica Scripta Volume T 47*, 133–138.

Guiderdoni, B. & B. Rocca-Volmerange (1987, November). A model of spectrophotometric evolution for high-redshift galaxies. *A&A 186*, 1–2.

Guiderdoni, B. & B. Rocca-Volmerange (1990, January). Constraints on the evolution of high-redshift galaxies and on q(0) from faint galaxy counts. *A&A 227*, 362–378.

Guiderdoni, B. & B. Rocca-Volmerange (1991, December). The faint galaxy counts revisited in an $\Omega_0 = 1$ universe. *A&A 252*, 435–448.

Halliday, C., R. L. Davies, H. Kuntschner, M. Birkinshaw, R. Bender, R. P. Saglia, & G. Baggley (2001, September). Line-of-sight velocity distributions of low-luminosity elliptical galaxies. *MNRAS 326*, 473–489.

Iglesias, C. A. & F. J. Rogers (1993, August). Radiative opacities for carbon- and oxygen-rich mixtures. *ApJ 412*, 752–760.

Im, M., R. E. Griffiths, K. U. Ratnatunga, & V. L. Sarajedini (1996, April). Luminosity Functions of Elliptical Galaxies at $Z < 1.2$. *ApJ 461*, L79+.

Itoh, N. & Y. Kohyama (1983, December). Neutrino-pair bremsstrahlung in dense stars. I - Liquid metal case. *ApJ 275*, 858–866.

Jedrzejewski, R. I. (1987, June). CCD surface photometry of elliptical galaxies. I - Observations, reduction and results. *MNRAS 226*, 747–768.

Jorgensen, I., M. Franx, & P. Kjaergaard (1996, May). The Fundamental Plane for cluster E and S0 galaxies. *MNRAS 280*, 167–185.

Jorgensen, I. & J. Hjorth (1997). The Fundamental Plane at Z = 0.18. In L. N. da Costa & A. Renzini (Eds.), *Galaxy Scaling Relations: Origins, Evolution and Applications*, pp. 175–+.

Kauffmann, G., S. D. M. White, & B. Guiderdoni (1993, September). The Formation and Evolution of Galaxies Within Merging Dark Matter Haloes. *MNRAS 264*, 201–+.

Kawata, D. & B. K. Gibson (2003, November). Multiwavelength cosmological simulations of elliptical galaxies. *MNRAS 346*, 135–152.

Kennicutt, Jr., R. C. (1983, September). The rate of star formation in normal disk galaxies. *ApJ 272*, 54–67.

Kippenhahn, R., H. C. Thomas, & A. Weigert (1965). Sternentwicklung IV. Zentrales Wasserstoff- und Heliumbrennen bei einem Stern von 5 Sonnenmassen. Mit 4 Textabbildungen. *Zeitschrift fur Astrophysik 61*, 241–+.

Kodama, T. & N. Arimoto (1997, April). Origin of the colour-magnitude relation of elliptical galaxies. *A&A 320*, 41–53.

Komiyama, Y., S. Miyazaki, M. Yagi, N. Yasuda, S. Okamura, M. Sekiguchi, M. Doi, K. Shimasaku, F. Nakata, H. Furusawa, M. Kimura, M. Ouchi, M. Hamabe, & H. Nakaya (2003, March). Suprime-Cam: Subaru prime focus camera. In M. Iye & A. F. M. Moorwood (Eds.), *Instrument Design and Performance for Optical/Infrared Ground-based Telescopes. Edited by Iye, Masanori; Moorwood, Alan F. M. Proceedings of the SPIE, Volume 4841, pp. 152-159 (2003).*, Volume 4841 of *Presented at the Society of Photo-Optical Instrumentation Engineers (SPIE) Conference*, pp. 152–159.

Kormendy, J. (1977, June). Brightness distributions in compact and normal galaxies. I - Surface photometry of red compact galaxies. *ApJ 214*, 359–361.

Kroupa, P. (1998, July). On the binary properties and the spatial and kinematical distribution of young stars. *MNRAS 298*, 231–242.

Kroupa, P. (2001, April). On the variation of the initial mass function. *MNRAS 322*, 231–246.

Kurucz, R. L. (1992). Model Atmospheres for Population Synthesis. In B. Barbuy & A. Renzini (Eds.), *The Stellar Populations of Galaxies*, Volume 149 of *IAU Symposium*, pp. 225–+.

La Barbera, F., G. Busarello, P. Merluzzi, M. Massarotti, & M. Capaccioli (2003, September). On the Invariant Distribution of Galaxies in the r_e-¡μ¿$_e$ Plane out to z=0.64. *ApJ 595*, 127–136.

Landre, V., N. Prantzos, P. Aguer, G. Bogaert, A. Lefebvre, & J. P. Thibaud (1990, December). Revised reaction rates for the H-burning of O-17 and the oxygen isotopic abundances in red giants. *A&A 240*, 85–92.

Larson, R. B. (1974, March). Dynamical models for the formation and evolution of spherical galaxies. *MNRAS 166*, 585–616.

Larson, R. B. (1975, December). Models for the formation of elliptical galaxies. *MNRAS 173*, 671–699.

Larson, R. B. (1986, February). Bimodal star formation and remnant-dominated galactic models. *MNRAS 218*, 409–428.

Larson, R. B. (1998, December). Early star formation and the evolution of the stellar initial mass function in galaxies. *MNRAS 301*, 569–581.

Levinson, F. H. & W. W. Roberts, Jr. (1981, April). A cloud/particle model of the interstellar medium - Galactic spiral structure. *ApJ 245*, 465–481.

Lia, C., L. Portinari, & G. Carraro (2002, March). Star formation and chemical evolution in smoothed particle hydrodynamics simulations: a statistical approach. *MNRAS 330*, 821–836.

Lucy, L. B. (1977, December). A numerical approach to the testing of the fission hypothesis. *AJ 82*, 1013–1024.

Lupton, R. H., J. E. Gunn, & A. S. Szalay (1999, September). A Modified Magnitude System that Produces Well-Behaved Magnitudes, Colors, and Errors Even for Low Signal-to-Noise Ratio Measurements. *AJ 118*, 1406–1410.

Marri, S. & S. D. M. White (2003, October). Smoothed particle hydrodynamics for galaxy-formation simulations: improved treatments of multiphase gas, of star formation and of supernovae feedback. *MNRAS 345*, 561–574.

McClure, R. D. & S. van den Bergh (1968, June). Five-color intermediate-band photometry of stars, clusters, and galaxies. *AJ 73*, 313–+.

Merlin, E. & C. Chiosi (2006, October). Formation and evolution of early-type galaxies. II. Models with quasi-cosmological initial conditions. *A&A 457*, 437–453.

Merlin, E. & C. Chiosi (2007, June). Simulating the formation and evolution of galaxies: Multi-phase description of the interstellar medium, star formation, and energy feedback. *ArXiv e-prints 706*.

Meza, A., J. F. Navarro, M. Steinmetz, & V. R. Eke (2003, June). Simulations of Galaxy Formation in a ΛCDM Universe. III. The Dissipative Formation of an Elliptical Galaxy. *ApJ 590*, 619–635.

Mihalas, D., D. G. Hummer, B. W. Mihalas, & W. Daeppen (1990, February). The equation of state for stellar envelopes. IV - Thermodynamic quantities and selected ionization fractions for six elemental mixes. *ApJ 350*, 300–308.

Mobasher, B., P. Capak, N. Z. Scoville, T. Dahlen, M. Salvato, H. Aussel, D. J. Thompson, R. Feldmann, L. Tasca, O. Lefevre, S. Lilly, C. M. Carollo, J. S. Kartaltepe, H. McCracken, J. Mould, A. Renzini, D. B. Sanders, P. L. Shopbell, Y. Taniguchi, M. Ajiki, Y. Shioya, T. Contini, M. Giavalisco, O. Ilbert, A. Iovino, V. Le Brun, V. Mainieri, M. Mignoli, & M. Scodeggio (2007, September). Photometric Redshifts of Galaxies in COSMOS. *ApJS 172*, 117–131.

Munakata, H., Y. Kohyama, & N. Itoh (1985, September). Neutrino energy loss in stellar interiors. *ApJ 296*, 197–203.

O'Connell, R. W. (1980, March). Galaxy spectral synthesis. II - M32 and the ages of galaxies. *ApJ 236*, 430–440.

O'Connell, R. W. (1986). Analysis of stellar populations at large lookbacks. In *Spectral evolution of galaxies, p. 321 - 343*, pp. 321–343.

Oke, J. B. (1964, August). Photoelectric Spectrophotometry of Stars Suitable for Standards. *ApJ 140*, 689–+.

Oke, J. B. & J. E. Gunn (1983, March). Secondary standard stars for absolute spectrophotometry. *ApJ 266*, 713–717.

Patton, D. R., C. J. Pritchet, H. K. C. Yee, E. Ellingson, & R. G. Carlberg (1997, January). Close Pairs of Field Galaxies in the CNOC1 Redshift Survey. *ApJ 475*, 29–+.

Peebles, P. J. E. (2002). When did the Large Elliptical Galaxies Form? In N. Metcalfe & T. Shanks (Eds.), *A New Era in Cosmology*, Volume 283 of *Astronomical Society of the Pacific Conference Series*, pp. 351–+.

Pickles, A. J. (1985, September). Differential population synthesis of early-type galaxies. III - Synthesis results. *ApJ 296*, 340–369.

Piovan, L., R. Tantalo, & C. Chiosi (2003, September). Shells of dust around AGB stars: Effects on the integrated spectrum of Single Stellar Populations. *A&A 408*, 559–579.

Piovan, L., R. Tantalo, & C. Chiosi (2006a, March). Modelling galaxy spectra in presence of interstellar dust - I. The model of interstellar medium and the library of dusty single stellar populations. *MNRAS 366*, 923–944.

Piovan, L., R. Tantalo, & C. Chiosi (2006b, August). Modelling galaxy spectra in presence of interstellar dust - II. From the ultraviolet to the far-infrared. *MNRAS 370*, 1454–1478.

Probst, R. G., A. Montane, M. Warner, M. Boccas, M. Bonati, R. Galvez, R. Tighe, M. C. Ashe, N. S. van der Bliek, & R. D. Blum (2003, March). ISPI: the infared side port imager for the CITO 4-m telescope. In M. Iye & A. F. M. Moorwood (Eds.), *Instrument Design and Performance for Optical/Infrared Ground-based Telescopes. Edited by Iye, Masanori; Moorwood, Alan F. M. Proceedings of the SPIE, Volume 4841, pp. 411-419 (2003).*, Volume 4841 of *Presented at the Society of Photo-Optical Instrumentation Engineers (SPIE) Conference*, pp. 411–419.

Reimers, D. (1975). Circumstellar absorption lines and mass loss from red giants. *Memoires of the Societe Royale des Sciences de Liege 8*, 369–382.

Renzini, A. & A. Buzzoni (1983). Theoretical foundations of evolutionary population synthesis A progress report. *Memorie della Societa Astronomica Italiana 54*, 739–745.

Renzini, A. & A. Buzzoni (1986a). Global properties of stellar populations and the spectral evolution of galaxies. In C. Chiosi & A. Renzini (Eds.), *Spectral Evolution of Galaxies*, Volume 122 of *Astrophysics and Space Science Library*, pp. 195–231.

Renzini, A. & A. Buzzoni (1986b). Global properties of stellar populations and the spectral evolution of galaxies. In *Spectral evolution of galaxies, p. 195 - 235*, pp. 195–235.

Ridgway, S. T., R. R. Joyce, N. M. White, & R. F. Wing (1980, January). Effective temperatures of late-type stars - The field giants from K0 to M6. *ApJ 235*, 126–137.

Rocca-Volmerange, B. (1989, January). An evolutionary model of star formation for elliptical galaxies. *MNRAS 236*, 47–56.

Rocca-Volmerange, B. & B. Guiderdoni (1987, March). Star formation in nuclei of S0/E galaxies. *A&A 175*, 15–22.

Rocca-Volmerange, B. & B. Guiderdoni (1988, October). An atlas of synthetic spectra of galaxies. *A&AS 75*, 93–106.

Rocca-Volmerange, B. & B. Guiderdoni (1990, November). Merging Driven Evolution of High Redshift Galaxies in a Universe with OMEGA/0=1. *MNRAS 247*, 166–+.

Rogers, F. J. & C. A. Iglesias (1992, April). Radiative atomic Rosseland mean opacity tables. *ApJS 79*, 507–568.

Salasnich, B., L. Girardi, A. Weiss, & C. Chiosi (2000, September). Evolutionary tracks and isochrones for alpha-enhanced stars. *A&A 361*, 1023–1035.

Salpeter, E. E. (1955, January). The Luminosity Function and Stellar Evolution. *ApJ 121*, 161–+.

Schade, D., S. J. Lilly, D. Crampton, R. S. Ellis, O. Le Fèvre, F. Hammer, J. Brinchmann, R. Abraham, M. Colless, K. Glazebrook, L. Tresse, & T. Broadhurst (1999, November). Hubble Space Telescope Imaging of the CFRS and LDSS Redshift Surveys. III. Field Elliptical Galaxies at $0.2 < z < 1.0$. *ApJ 525*, 31–46.

Schlegel, D. J., D. P. Finkbeiner, & M. Davis (1998, June). Maps of Dust Infrared Emission for Use in Estimation of Reddening and Cosmic Microwave Background Radiation Foregrounds. *ApJ 500*, 525–+.

Schmidt, M. (1959, March). The Rate of Star Formation. *ApJ 129*, 243–+.

Scoville, N., H. Aussel, M. Brusa, P. Capak, C. M. Carollo, M. Elvis, M. Giavalisco, L. Guzzo, G. Hasinger, C. Impey, J.-P. Kneib, O. LeFevre, S. J. Lilly, B. Mobasher, A. Renzini, R. M. Rich, D. B. Sanders, E. Schinnerer, D. Schminovich, P. Shopbell, Y. Taniguchi, & N. D. Tyson (2007, September). The Cosmic Evolution Survey (COSMOS): Overview. *ApJS 172*, 1–8.

Searle, L., W. L. W. Sargent, & W. G. Bagnuolo (1973, January). The History of Star Formation and the Colors of Late-Type Galaxies. *ApJ 179*, 427–438.

Spergel, D. N., L. Verde, H. V. Peiris, E. Komatsu, M. R. Nolta, C. L. Bennett, M. Halpern, G. Hinshaw, N. Jarosik, A. Kogut, M. Limon, S. S. Meyer, L. Page, G. S. Tucker, J. L. Weiland, E. Wollack, & E. L. Wright (2003, September). First-Year Wilkinson Microwave Anisotropy Probe (WMAP) Observations: Determination of Cosmological Parameters. *ApJS 148*, 175–194.

Tantalo, R. (2005, January). New database of SSPs with different IMFs. In E. Corbelli, F. Palla, & H. Zinnecker (Eds.), *The Initial Mass Function 50 Years Later*, Volume 327 of *Astrophysics and Space Science Library*, pp. 235–+.

Tantalo, R., A. Bressan, & C. Chiosi (1997, October). To what Extent are Mg_2 and <Fe> indicators of Mg and Fe Abundances? *ArXiv Astrophysics e-prints*.

Tantalo, R. & C. Chiosi (2004, September). Measuring age, metallicity and abundance ratios from absorption-line indices. *MNRAS 353*, 917–940.

Tantalo, R., C. Chiosi, & A. Bressan (1998, May). Ages and metallicities in elliptical galaxies from the H_beta, <Fe>, and Mg_2 diagnostics. *A&A 333*, 419–432.

Tantalo, R., C. Chiosi, A. Bressan, & F. Fagotto (1996, July). Spectro-photometric evolution of elliptical galaxies. II. Models with infall. *A&A 311*, 361–383.

Tantalo, R., C. Chiosi, A. Bressan, P. Marigo, & L. Portinari (1998, July). Spectro-photometric evolution of elliptical galaxies. III. Infall models with gradients in mass density and star formation. *A&A 335*, 823–846.

Tinsley, B. M. (1968, February). Evolution of the Stars and Gas in Galaxies. *ApJ 151*, 547–+.

Tinsley, B. M. (1980a). Evolution of the Stars and Gas in Galaxies. *Fundamentals of Cosmic Physics 5*, 287–388.

Tinsley, B. M. (1980b, October). On the interpretation of galaxy counts. *ApJ 241*, 41–53.

Treu, T., R. S. Ellis, T. X. Liao, P. G. van Dokkum, P. Tozzi, A. Coil, J. Newman, M. C. Cooper, & M. Davis (2005, November). The Assembly History of Field Spheroidals: Evolution of Mass-to-Light Ratios and Signatures of Recent Star Formation. *ApJ 633*, 174–197.

Turnrose, B. E. (1976, November). The stellar content of the nuclear regions of SC galaxies. *ApJ 210*, 33–37.

van der Wel, A., M. Franx, P. G. van Dokkum, H.-W. Rix, G. D. Illingworth, & P. Rosati (2005, September). Mass-to-Light Ratios of Field Early-Type Galaxies at z ˜ 1 from Ultradeep Spectroscopy: Evidence for Mass-dependent Evolution. *ApJ 631*, 145–162.

van Dokkum, P. G. & M. Franx (1996, August). The Fundamental Plane in CL 0024 at z = 0.4: implications for the evolution of the mass-to-light ratio. *MNRAS 281*, 985–1000.

van Dokkum, P. G., M. Franx, D. Fabricant, G. D. Illingworth, & D. D. Kelson (2000, September). Hubble Space Telescope Photometry and Keck Spectroscopy of the Rich Cluster MS 1054-03: Morphologies, Butcher-Oemler Effect, and the Color-Magnitude Relation at Z = 0.83. *ApJ 541*, 95–111.

van Dokkum, P. G., M. Franx, D. D. Kelson, & G. D. Illingworth (1998, September). Luminosity Evolution of Early-Type Galaxies to Z = 0.83: Constraints on Formation Epoch and Omega. *ApJ 504*, L17+.

Vazdekis, A., E. Casuso, R. F. Peletier, & J. E. Beckman (1996, October). A New Chemo-evolutionary Population Synthesis Model for Early-Type Galaxies. I. Theoretical Basis. *ApJS 106*, 307–+.

Vazdekis, A., R. F. Peletier, J. E. Beckman, & E. Casuso (1997, July). A New Chemo-evolutionary Population Synthesis Model for Early-Type Galaxies. II. Observations and Results. *ApJS 111*, 203–+.

White, S. D. M. & M. J. Rees (1978, May). Core condensation in heavy halos - A two-stage theory for galaxy formation and clustering. *MNRAS 183*, 341–358.

Yoshii, Y. & F. Takahara (1988, March). Galactic evolution and cosmology - Probing the cosmological deceleration parameter. *ApJ 326*, 1–18.

Ziegler, B. L. & R. Bender (1997, November). The Mg(b)-sigma relation of elliptical galaxies at Z of about 0.37. *MNRAS 291*, 527–+.